MICRODISTRIBUTION OF IMPURITIES IN SEMICONDUCTORS AND ITS INFLUENCE ON PHOTOVOLTAIC ENERGY CONVERSION

by

PAOLO RAVA

B.S., Politecnico di Torino
(1975)

M.S., University of London
(1976)

SUBMITTED IN PARTIAL FULFILLMENT
OF THE REQUIREMENTS FOR THE
DEGREE OF
DOCTOR OF PHILOSOPHY

at the

MASSACHUSETTS INSTITUTE OF TECHNOLOGY

June 1981

Signature of Author_____
Department of Physics
March 3, 1981

Certified by_____
Harry C. Gatos
Thesis Supervisor

Accepted by_____
George F. Koster
Departmental Graduate Committee

MICRODISTRIBUTION OF IMPURITIES IN SEMICONDUCTORS AND ITS INFLUENCE ON PHOTOVOLTAIC ENERGY CONVERSION

by

PAOLO RAVA

Submitted to the Department of Physics
on March 3, 1981 in partial fulfillment of the
requirements for the degree of
Doctor of Philosophy in Physics

ABSTRACT

In the present investigation for the first time the interstitial oxygen distribution in Si has been investigated on a microscale and correlated to the activation of thermal donors by 450°C heat treatment. Scanning IR absorption was used to measure the axial oxygen microdistribution at different distances from the edge of the crystal. The light source used had a wavelength in the neighborhood of the 9 μm oxygen absorption band; interference due to multireflections inside the sample was avoided, reducing the reflectivity, by applying an AR coating to the surfaces of the sample.

The free carrier microdistribution along the same locations was measured, after a 450°C heat treatment, using a spreading resistance probe. A comparison of the two microprofiles revealed direct correspondence in the general features, but no correlation between oxygen and thermal donor concentration in some areas; in particular, no activation of donors took place in some areas. After a 650°C heat treatment, all donors were annihilated; upon subsequent 450°C heat treatment, donors were activated again, but in a different pattern: the areas which were activated the first time now exhibited smaller densities of thermal donors and the areas which were not previously activated exhibited high donor concentration.

The microdefect distribution was studied as a function of heat treatment time and compared to the activated donor microprofiles. A high density of B-defects was found in areas where no donor activation took place upon the first heat treatment at 450°C, whereas A-defects were present in areas where donors were activated. Upon 650°C heat treatment B-defects became larger and less dense, approaching A-defects and allowing activation of donors upon further 450°C heat treatment.

The influence of different dopants (B, Ga, In) on the activation rate was investigated. It was determined that the activation rate is enhanced by the presence of Ga in all regions of the crystal and by the presence of In near the periphery.

These results are qualitatively in agreement with the vacancy-oxygen model proposed for donor activation. According to this model, an oxygen atom can slip into a Si vacancy and be bound to this site by bonding one of its electrons with another nearest neighbor Si vacancy; this complex

can then be easily ionized by releasing the extra electron. A neighbor vacancy diffused at 650°C can trap this free electron to form an electrically inert complex. The presence of unactivated areas close to the crystal periphery was attributed to a lower concentration of available vacancies due to the presence of the B-defects (vacancy clusters); a 650°C heat treatment changed their structure, possibly releasing vacancies which then participated in donor formation. On the other hand, the areas activated the first time at 450°C have fewer vacancies available the second time for donor formation and therefore are less activated. Acceptor atoms can also contribute to the formation of donors by forming complexes with oxygen and therefore enhancing the activation rate, as observed in Ga-doped Si. A high concentration of acceptor impurities can also increase the concentration of available vacancies near the periphery, as observed in In-doped Si. It was shown that the vacancy-oxygen complex must be the first step in the formation of multi-vacancy or any multi-oxygen donor complexes.

The role of a factor other than oxygen in donor activation can be revealed only by a microscale analysis such as the one presented here. In fact, the areas in which donor formation is enhanced by 650°C heat treatment are completely undetected in a macroscale analysis, which therefore would lead to a proportionality between oxygen concentration and activated donors. This work shows that the accepted premise that the concentration of oxygen donors is proportional to the oxygen concentration is not generally valid.

Multiple p-n junctions have been prepared in B-doped Si through overcompensation near the oxygen periodic concentration maxima by thermal donors generated during an appropriate heat treatment at 450°C. Application of this structure to photovoltaic energy conversion has been investigated. A new solar cell structure based on multiple p-n junctions was developed and tested. An increase in short circuit current was achieved, but at the same time a degradation in open circuit voltage occurred. An interpretation of the experimental data in the light of the results of a computer simulation showed that an overall increase in efficiency can be achieved in this structure with a small and regular junction spacing.

The effect of carrier density inhomogeneities in InP and GaAs samples was then investigated. The same scanning IR absorption technique employed in the first part of this study was used to measure free carrier microprofiles in order to determine the homogeneity of the samples. It was established that presence of inhomogeneities can lead to a significant ambiguity in the determination on a macroscale of mobility, carrier concentration and absorption coefficient.

A procedure based on independent measurements of the free carrier absorption and of the electron mobility was used to determine the compensation ratio in InP. This procedure was determined to be applicable only to homogeneous samples. A microscale analysis such as the one presented here has been proven to be necessary to clarify ambiguities arising from macroscale measurements.

Thesis Supervisor: Professor Harry C. Gatos

Title: Professor of Electronic Materials

TABLE OF CONTENTS

ACKNOWLEDGMENTS

This thesis is the result of a few years' work as a research assistant in the Electronic Materials Group at MIT; the interaction with the human and scientific resources provided by the people of the group is largely responsible for the accomplishment of the results presented in this work. Therefore I am grateful to all the people who assisted me in one way or another during the completion of this thesis, even though it is not possible to name all of them.

First of all I wish to thank Professor Harry C. Gatos for giving me the opportunity to spend a few years in the United States, an experience that had a very positive influence on my life and career. I am also grateful to him for providing me with a careful guidance which has gradually taught me to be more independent in tackling and solving problems. Thanks also to Dr. Jacek Lagowski who gave me valuable advice and helped me gain more insight into scientific problems. Professor August F. Witt gave numerous helpful suggestions.

During most of the completion of this thesis I worked in close cooperation with Dr. Jim Y. Chi; most of the ideas and approaches presented here initiated from discussions with him. I learned to appreciate not only his valuable scientific advice but also his friendly and generous character that made more pleasant an often demanding work.

A special thanks goes also to Cliff Herman whose technical skill, inventiveness and willingness to help made possible the practical realization of ideas which otherwise might have been infeasible. Joe DiMaria also provided valuable technical assistance. Equally valuable has been the help of Phyllis Merrick and Gloria Landahl in all the administrative matters. Gloria also did a very good job in typing this manuscript.

The advice of some other people also gave a very helpful contribution. In particular, Dr. Lubomir Jastrzebski guided me closely during the initial period of my work in the Electronic Materials Group; Bor Yen Mao gave me useful advice on photovoltaics, David Bliss on silicon crystal growth and properties; Dr. John Vaughan was very helpful in all the measurements on the SEM.

A special thanks goes to my parents, who encouraged me to come to the United States for an experience they knew would be valuable for me even though I might have been away from home for a long time.

The author is grateful to the National Aeronautics and Space Administration, Lewis Research Center, for the financial support provided; and to the Commission for Cultural Exchange between Italy and the United States for the assistance provided for the admission to MIT and for the travel grant under the Fulbright program.

Paolo Rava
Cambridge, Massachusetts

I. INTRODUCTION

I.1 Impurities in semiconductors

Impurities of various types are invariably present in semiconductors and have a very important influence on the electrical and optical characteristics of the material and consequently on the device performance. Impurities can be either intentional or unintentional, according to whether they have been intentionally introduced to achieve required material parameters or they have been unintentionally introduced due to the growth or processing apparatus or environment or other unknown factors.

Intentional impurities are often referred to as dopants and their main purpose is to introduce donor or acceptor levels which are usually ionized at room temperature to give a required electron or hole concentration. Unintentional impurities have often unwanted effects on the electrical and optical characteristics of semiconductors.

Both categories of impurities are non-uniformly distributed, due to thermal asymmetries in the growth conditions. Although the importance of impurities in semiconductors has been recognized for some time, their study and understanding have been limited to a macroscale and to phenomenological basis. Such macroscale investigations deal with quantities averaged in an area over which the impurity concentration can change considerably and therefore can often lead to misleading conclusions. A better understanding of the influence of impurities on material parameters requires knowledge of the relationships between the distribution of impurities and the electrical and optical properties of the semiconductor on a microscale.

I.2 Silicon

Silicon has been for a long time and still is the semiconductor most used in photovoltaic and other applications and most extensively studied.

The main unintentional impurities in silicon are oxygen and carbon; the main sources of oxygen contamination are the SiO_2 crucibles and of carbon, the graphite accessories. Oxygen is invariably present in Czochralski-grown silicon crystals at concentration levels in the vicinity of 10^{18} cm^{-3} and carbon in the vicinity of 10^{16} - 10^{17} cm^{-3}.

The influence of these two impurities on the electrical and optical properties of silicon has been extensively investigated on a macroscale. Oxygen and carbon give rise to two infrared absorption bands respectively around 9 μm and 16.5 μm, which are routinely used to determine the concentration of these two impurites. It is also well-known that the resistivity of a silicon crystal containing oxygen changes upon heat treatment at a temperature in the vicinity of 450°C; this effect has been attributed to the activation of oxygen donors. The microdistribution of oxygen donors has been obtained by electrical measurements and in the past it was assumed to coincide with the oxygen microdistribution. Different hypothesis have been advanced for the mechanism of donor activation based on macroscale experimental results; so far a correlation between oxygen microdistribution and activated donors microdistribution has been lacking.

In the present work an IR absorption scanning technique was developed; this technique allows the direct determination of oxygen microprofiles in silicon crystals, it is non-destructive and requires no contacts. A comparison of the obtained oxygen microprofiles and of the activated donor microprofiles can be interpreted in light of the proposed models for donor activation.

Dopant impurities in silicon have also been extensively studied. Due to the advanced stage of development of silicon technology, usually only one type of electrically active impurity is present in silicon crystals and

its concentration is proportional to the free carrier concentration. The impurity microprofiles can be determined by measuring free carrier microprofiles either by direct electrical methods or by an IR free carrier absorption technique which is essentially the same employed in determining oxygen microprofiles.

I.3 III-V Compounds

Quite different is the situation in other semiconductors, like GaAs or InP, which have recently attracted more attention due to some desirable features resulting from a direct energy gap slightly larger than the indirect gap of silicon.

In these semiconductors, usually both donor and acceptor centers coexist, and their spacial variations are larger than in silicon due to the difficulty to obtain perfect stoichiometry. For GaAs and InP the free carrier microdistribution can be readily obtained by the same IR free carrier absorption scanning technique employed for silicon, but the determination of the actual impurity microprofiles requires an analysis of the wavelength dependence of free carrier absorption.

The relatively large inhomogeneities often present in the free carrier concentration make possible an analysis of their influence on macroscopic material parameters. Once again, a microscale analysis is necessary to reveal factors which were previously unaccounted for by macroscale measurements.

I.4 Influence of impurities on photovoltaic energy conversion

Impurities have a very important effect on the electronic and optical properties of semiconductors and therefore on photovoltaic energy conversion. In fact, the main parameters relevant to the design of a photovoltaic device are determined by the concentration of various impurities

in the semiconductor considered. Namely, the free carrier concentration is determined by the concentration of ionized donor and acceptor impurities. The mobility, the diffusion length and the lifetime are determined by the concentration of deep level impurities, as well as by the concentration of shallow donor and acceptor impurities. A better understanding of the influence of impurities on photovoltaic energy conversion therefore requires a better understanding of their influence on material parameters, which can be achieved by a microscale analysis.

An inhomogeneous impurity distribution has also a direct influence on macroscopic material parameters and on conversion efficiency. In fact, in the case of large area devices, such as photovoltaics, an inhomogeneous impurity distribution can create electric fields; it is conceivable that an appropriate disposition of these electric fields could be found to improve device performance. The development of crystal growth techniques aimed at obtaining appropriate impurity profiles has to be based on reliable microcharacterization techniques.

Both silicon and the III-V compounds have to be taken into account in an investigation of the influence of the microdistribution of impurities on photovoltaic energy conversion. Silicon is the material most widely used for photovoltaic applications due to its very well developed technology, its relatively high theoretical conversion efficiency, its potential for cost reduction and the lack of environmental problems.

GaAs and InP technology is not as well developed, but these materials have a higher theoretical conversion efficiency which makes them attractive for concentrator applications. In addition, InP has the potential for an efficiency higher than GaAs at the high temperatures common for operation under concentrated sunlight.

II. LITERATURE REVIEW AND MOTIVATION

II.1 Oxygen in silicon

Due to its very widespread and important applications, silicon has been one of the semiconductors most extensively investigated. In particular, the oxygen impurity in silicon has been the focus of investigation for quite some time due to its important influence on electrical properties. The presence of oxygen in silicon has been revealed by infrared studies.

Collins and Fan (1) measured the first infrared spectra of silicon at room temperature and at lower temperatures; they found that the absorption of all lattice bands increased with temperature except for a strong band with maximum room temperature absorption at about 9 μm (1106 cm^{-1}) which presented an anomalous behavior. This was the only band whose absorption did not increase with temperature and also whose peak showed a clear shift in frequency with temperature.

Kaiser et al (2) correlated the 9 μm band with the oxygen content of silicon. They investigated the 9 μm band at room temperature and low temperatures for a wide range of silicon crystals, grown both by the Czochralski and by the float zone technique; the oxygen content of the crystals was determined by vacuum fusion analysis. The absorption coefficient at 9 μm was found to be proportional to the oxygen content; the absorption coefficient for Czochralski-grown samples increased at low temperatures while for float-zone samples (which had very low oxygen content) it decreased at low temperatures.

These facts allowed the assignment of the 9 μm band for samples with high oxygen content (10^{17} - 10^{18} cm^{-3}) to the vibration of a Si-O-Si unit; such a unit can be formed by two neighboring Si atoms which give up their co-

valent bond and engage with an interstitial oxygen atom instead, forming an isosceles triangle with Si, O, Si at the corners, with a bond angle Si-O-Si of approximately 100°. This vibration is superimposed on a weak lattice band, which is the only one present in float zone samples as evident from the different temperature dependence.

The number N_o of independent Si-O-Si oscillators is proportional to the area of the absorption band and can be estimated from the following equation:

$$N_o = \frac{9n}{(n^2 + 2)^2} \frac{3\mu c}{\pi e^2} \int \alpha_\nu \, d\nu \qquad (2.1)$$

where α_ν is the absorption coefficient at the frequency ν, μ is the reduced mass of the oscillator, e is the net electronic charge, and n is the refractive index of the surrounding medium. The calculation of N_o from infrared absorption data was found to be in good agreement with oxygen content data from vacuum fusion analysis.

It was concluded that optical absorption measurements can provide a reliable method for a quantitative analysis of oxygen in silicon, once an appropriate calibration of oxygen concentration versus 9 μm absorption coefficient has been obtained.

Hrostowski and Kaiser (3) correlated three infrared absorption bands with the oxygen concentration of silicon. The most intense band is the 9 μm (1106 cm^{-1}) band already investigated by the previous authors; two less intense bands were observed at 515 cm^{-1} and at 1205 cm^{-1}. The 9 μm band peak was found to shift to higher frequencies and its absorption coefficient to increase with decreasing temperature; at the same time, the

band width narrowed so that the total intensity of the band was temperature independent. The three observed vibrations were identified with the three normal vibrations of the Si-O-Si unit previously proposed (2). The 9 μm band was assigned to the antisymmetric stretching motion, in which the O atom oscillates along the <111> direction in the silicon lattice and the Si atoms oscillate along the Si-O bonds with opposite phase.

Hrostowski also observed (3,4) the appearance of a fine structure at very low temperatures in the 9 μm band and refined the model for the infrared absorption previously proposed. He concluded that the oxygen atom occupies a position slightly displaced from an interstitial lattice site and at room temperature occupies a number of slightly different configurations of varying energy, from which a broad band width results. On cooling the oxygen atom is forced into equilibrium positions of different energy, which correspond to the fine structure observed.

The most important result of Hrostowski's and Kaiser's work was that the concentration of interstitial oxygen could be determined from the absorption coefficient of the 9 μm band. The exact determination of the interstitial oxygen concentration therefore requires a calibration of oxygen concentration versus absorption coefficient. Many authors have focused their attention on the determination of this calibration (5-8) and this technique has become the standard measurement to determine non-destructively the oxygen concentration in silicon. The ASTM standard (9) recommends the following calibration:

$$[O] = 4.81 \times 10^{17} \alpha_o \qquad (2.2)$$

where α_o is the oxygen absorption coefficient at room temperature. This technique is more sensitive at low temperatures due to the increase in absorption coefficient; a lower value of the calibration constant has to be used at low temperatures (9).

Fuller et al (11-12) were the first to report an increase in donor concentration in silicon crystals grown by the Czochralski technique and heat-treated in the temperature range 350°C - 500°C.

Kaiser (13) correlated the formation of donor states with the presence of interstitial oxygen as revealed by the 9 μm absorption band.

Kaiser et al (14) summarized and completed the investigation of the salient features of donor formation:

(1) The donor concentration of oxygen containing silicon crystals increases as a function of heat treatment time at temperatures in the vicinity of 450°C, reaches a maximum and subsequently decreases slowly.

(2) Donor states, once formed in the specimen, can be removed rapidly by subsequent heating at temperatures above 500°C.

(3) The time of attainment of the donor concentaation maximum decreases with an increase in the heat treatment temperature while the maximum donor concentration increases with decreasing temperature.

(4) The initial rate of donor formation is proportional to the fourth power of the oxygen concentration.

(5) The maximum donor concentration is approximately proportional to the third power of the oxygen concentration.

(6) If A(t) is the donor concentration at time t, and A* that corresponding to the maximum, then at times prior to the appearance of the maximum ℓn (A* - A) is a linear function of time.

(7) If the crystal is heated to 1000°C for an appreciable period of time, it is "stabilized" in the sense that heating at 450°C no longer produces donors. Furthermore, optical studies indicate that SiO_2 precipitates form.

Kaiser et al (14) proposed a model which is able to correlate the above facts in a rather quantitative manner. It is based on the assumption that a series of complexes of oxygen and silicon form containing larger and larger numbers of atoms, culminating finally in the creation of a new phase, SiO_2. In this form, the oxygen is stabilized and prevented from entering reactions leading to donor formation; hence, the stabilization produced by heating at 1000°C. The donors are thought to be the intermediate complexes formed in the reaction chain which contain not more than four oxygen atoms.

Following Kaiser et al, a single oxygen in silicon is denoted by A_1, a complex of two by A_2, of three by A_3, and of four by A_4. Larger complexes are denoted by the symbol P (for polymer) with a subscript indicating the number of oxygen atoms contained. The following set of reactions are then postulated:

$$A_1 + A_1 \rightleftarrows A_2$$
$$A_2 + A_1 \rightleftarrows A_3$$
$$A_3 + A_1 \rightleftarrows A_4$$
$$A_4 + A_1 \rightleftarrows P_5$$
$$\text{etc.} \qquad (2.3)$$

It is further assumed that the first two reactions of eq. (2.3) are very rapid, so that instantaneous equilibrium between A_1 and A_3 is always established. Thus,

$$A_3 = K A_1^3 \qquad (2.4)$$

in which K is an equilibrium constant. Applying the law of mass action to the last two equations of 2.3, neglecting depolymerization and variations in A_1, the time rate of appearance of A_4 can be written as:

$$\frac{dA_4}{dt} = k_f A_1^4 - (k_b + k_p A_1) A_4 \qquad (2.5)$$

in which k_f is an effective forward rate constant and k_b is a backward rate constant for the reaction $4A_1 \underset{k_b}{\overset{k_f}{\rightleftarrows}} A_4$ and k_p the rate constant for the forward reaction in the fourth of eq. 2.3. Simple mathematical manipulations on eq. 2.5 show that this model can account for many of the experimental facts reported above.

Although the SiO_4 complex is considered the main contributor to the donor activity, Kaiser does not rule out the possibility that complexes containing less than four oxygen atoms (SiO_3 or SiO_2) could be responsible for donor activity for very short heat treatments at temperatures below 433°C.

Although Kaiser's work firmly established the influence of oxygen on the formation of thermal donors in silicon, his model for donor activation presents many weaknesses in the light of results of further experimental work.

Diffusion data do not allow the formation of oligoatomic oxygen complexes. Extrapolation of the high temperature diffusion data measured by several authors (15-18) to 450°C gives a diffusion length of oxygen in silicon which is smaller than the average distance of oxygen atoms in Czochralski silicon.

Kaiser's quantitative model assumed equilibrium conditions so that the mass action law would hold. Measurements of the solubility of oxygen in silicon (19,20) show that donor formation at 450°C takes place under highly supersaturated conditions, since the solubility limit for oxygen concentration of the order of 10^{18} cm^{-3} is set above 1200°C. Such conditions are non-equilibrium conditions, so that the mass action law does not hold.

The experimentally found exponential relationships between initial oxygen concentration and thermal donor concentration and generation rate could not convincingly be confirmed by the work of Bean and Newman (21) and Helmreich and Sirtl (22).

A last important weakness is the difficulty in explaining the donor activity of the SiO_4 complexes (21).

It is clear from the above that the SiO_4 model was far from being well established: further experimental work contributed new results and led to the formulation of other models.

Fuller et al (23,24) studied the influence of acceptor dopants on thermal donor generation. They found that the presence of acceptor dopants

enhanced thermal donor activation; differences existed between different types and concentrations of dopants; the increase in donor concentration was generally accompanied by a decrease in acceptor concentration; no comparable effect of n-type dopants was observed on thermal donor activation.

Hrostowski and Kaiser (25) investigated the infrared spectra of Group III acceptors in silicon at very low temperatures. They found that the presence of oxygen influences the absorption band due to gallium and attributed this fact to the formation of a gallium-oxygen complex. It was concluded that acceptor dopants can participate in the formation of thermal donors.

The influence of carbon on thermal donor activation also attracted considerable interest. Carbon is always present as an impurity in Czochralski-grown silicon: it has been associated with the 16.5 μm absorption band (26), from which its concentration can be measured (27,28). It has been determined that carbon occupies a substitutional site in silicon and that it decreases the silicon lattice parameter in direct proportion to its concentration (29).

Bean and Newman (21) investigated the effect of carbon on thermal donor formation on a number of samples with different carbon and oxygen concentrations. They determined that the presence of a high concentration of carbon strongly inhibits the formation of thermally produced donors; therefore the proportionality between activated donors and interstitial oxygen concentration found by Kaiser (14) does not hold in general.

Matukura (30) investigated the influence of crystal defects on thermal donor generation. By measuring activated donors in locations with

different defect concentration, he determined that defects inhibit thermal donor activation.

Graff et al (31,32) investigated the behavior of carrier lifetime in oxygen containing silicon as a function of heat treatment. The lifetime follows a behavior parallel to the donor concentration: it increases upon 450°C heat treatment and returns to the original values upon heat treatment at temperatures above 600°C.

The likelihood of the participation of another factor beside oxygen in thermal donor activation is evident from the results just discussed. Some authors suggested the participation of vacancies (33) and deep levels (32) in donor activation. Helmreich and Sirtl (22) proposed a new model which departs drastically from Kaiser's model and postulates the interaction of interstitial oxygen with silicon vacancies and acceptor dopants.

According to this model, during thermal activation of donors the interstitial oxygen, O_i, first occupies a silicon vacancy, V_{Si}, and then it combines with a neighboring silicon vacancy V_n:

$$O_i + V_{Si} \rightarrow O_{Si} \tag{2.6}$$

$$O_{Si} + V_n \rightarrow O_{Si}^{+} V_n^{-} \tag{2.7}$$

The oxygen-vacancy complex is then readily ionized as a donor:

$$O_{Si}^{+} V_n^{-} \rightarrow O_{Si}^{+2} V_n^{-} + e^{-} \tag{2.8}$$

A far neighbor vacancy V_f eventually may trap the free electron and form an electrically inactive complex:

$$O_{Si}^{+2} V_n^{-} + e^{-} + V_f \rightarrow O_{Si}^{+2} V_n^{-} V_f^{-} \tag{2.9}$$

Processes 2.7, 2.8 and 2.9 can also happen with the participation of an acceptor atom in place of a vacancy. Process 2.8 is predominant at 450°C, while process 2.9 is predominant at temperatures above 600°C due to a faster diffusion of vacancies; these processes account respectively for donor activation and donor annihilation.

Most of the experimental facts reported above can be explained by this model. Acceptors influence donor activation because they take part in the formation of donor complexes. A high carbon concentration decreases the lattice parameter releasing the lattice strain introduced by interstitial oxygen and reducing the concentration of vacancies: hence, the inhibiting action of carbon on thermal donor formation. Some types of defects are vacancy getters so that donor activation is reduced near them. Finally, vacancies and acceptor impurities, when occupied in donor complexes, can no longer act as traps for carriers, therefore the lifetime increases.

In spite of its success in explaining some experimental results, this model has some weaknesses in that it does not explain quantitatively as well as Kaiser's model some general features of thermal donor activation. In particular, it is worth noticing that in no thermal donor activation experiment ever reported the activated thermal donor concentration equals the initial oxygen concentration and in fact seldom it exceeds one-fourth of the initial oxygen concentration.

Recently more results concerning some features of thermal donor activation have been obtained. The energy position of the donor levels has been investigated since the early days of the study of oxygen in silicon silicon (12,30,34,35,36); the measured ionization energies vary greatly from one report to another.

Recently, Gaworzewski and co-workers (37,38) reported a detailed investigation of the energy levels as a function of heat treatment time. They found two sets of energy levels, one comprising a few levels about 45 to 65 meV from the conduction band and the other comprising a few levels about 80 to 140 meV from the conduction band. With increasing heat treatment time in both sets of levels higher energy lines decrease in intensity and lower energy lines increase in intensity, corresponding to an overall decrease of the average ionization energy. Similar results have been reported by Nakayama et al (39). These results are problematic to interpret in light of a simple oxygen-vacancy complex model.

Recently, comprehensive investigations on the effects of heat treatment on the properties of oxygen-containing large diameter dislocation-free silicon crystals have been reported (40-43). Thermal donor generation in the vicinity of 450°C has features similar to those reported by Kaiser (14), although a few minor differences exist. In addition to this already well-known effect, it was found that donors are activated also in a different temperature range, from about 600°C to 800°C; the features of these "new" donors present many differences with respect to the 450°C donors. These experimental findings have led to various speculations and models for the mechanisms of activation of both the "old" and the "new" donors. These models are often in contrast and are based either on Kaiser's (14) or Helmreich's (22) models.

The present state of understanding of the generation of thermal donors in silicon is unsatisfactory. Oxygen has unmistakably been identified as a necessary factor, but some other species seem to have an important influence: these other species have not yet been unmistakably identified.

The spatial distribution of oxygen in silicon was originally investigated by Kaiser and co-workers (5,13) and correlated to crystal growth parameters. The salient features are as follows:

i. The periphery of the crystal contains less oxygen than the center.

ii. The oxygen concentration fluctuates along the growth axis.

iii. There is an increase in oxygen content from the top to the bottom of the ingot.

iv. An increase in diameter and/or rotation rate increases the oxygen content.

The fluctuations in oxygen concentration along the growth axis are due to thermal asymmetries in the melt during growth (44). The microdistribution of thermal donors activated by 450°C was measured with high resolution electrical techniques (44-46) and was assumed to coincide with interstitial oxygen distribution. As evident from what was reported in the literature, this is not necessarily the case because the unidentified species which influences thermal donor activation besides oxygen could also be non-uniformly distributed.

II.2 III-V compounds

III-V semiconductors recently have been the focus of many investigations due to their desirable features in a number of device applications, including photovoltaic, microwave and optoelectronic devices. Usually more than one type of electrically active impurity is present, often of opposite conduction type; this gives rise to an appreciable degree of compensation of the free carrier concentration. Knowledge of the extent of compensation is important for the understanding of the basic electronic

characteristics of these materials and their devices and for the evaluation of crystal growth processes. The methods for determining the compensation are usually related to the fact that the compensation reduces the free carrier concentration and it enhances free carrier scattering by ionized impurities. In GaAs, because of the small donor ionization energy (~5 meV), the accurate determination of donor and acceptor concentrations from free carrier concentration changes must be carried out at temperatures well below 15°K. Similarly, the determination of the compensation ratio from the amplitude of Schubnikov - de Haas oscillations, as proposed recently by Raymond et al (47), must be carried out at 4.2°K. The low temperature requirements render these methods inaccessible for routine needs. Other methods based on scattering of free carriers by ionized impurities have been proposed for the determination of the compensation ratio. Rode and Knight (48) reported theoretical calculations of electron mobility for n-type GaAs including compensation as a parameter. They took into account all major scattering mechanisms; these consist of scattering by acoustic phonons through deformation potential and piezoelectric interactions, polar longitudinal optical phonon scattering and ionized impurity scattering. For polar mode scattering, the relaxation time cannot be defined except for low temperatures (49). So they used an iterative procedure to solve the Boltzmann equation, combining all relevant scattering mechanisms. The theoretical values of mobilitv obtained as a function of electron concentration with compensation as a parameter allowed the determination of compensation ratio when compared with experimental values.

Free carrier absorption has been used also for the determination of the compensation ratio in n-type GaAs (50-52). The infrared absorption

due to the optical excitation of a conduction electron into a higher state in the conduction band requires the presence of scattering by crystal imperfections; in fact, they can provide the momentum necessary to satisfy the conservation laws in the process of the absorption of a photon. The same three scattering sources relevant in the calculation of the mobility (48) were considered, although in this approach the ionized impurity contribution to free carrier absorption is separable from contributions by other scattering mechanisms. These authors (50-52) have not correlated the values of compensation ratio obtained from free carrier absorption to values obtained from mobility (48).

Walukiewicz et al (53) considered the effect of compensation on two independently measured quantities, i.e., on the electron mobility and on the free carrier absorption. They considered the following scattering mechanisms: screened optical phonon scattering (54), screened ionized impurity scattering (55), acoustic phonon scattering through the deformation potential and piezoelectric interactions (48). Screening effects had not been considered in previous calculations (48,50-52) and were found to be relevant for electron concentrations in excess of 10^{17} cm^{-3}. They used a variational method to calculate the mobility and an approach based on perturbation theory (50) to calculate the free carrier absorption. A procedure was then outlined for the convenient determination of the compensation ratio from measured values of room temperature electron mobility and from the absorption coefficient at a wavelength of about 10 μm. They found that values of the compensation ratio determined from two independent measurements were in good agreement for most samples. For a few samples discrepancies were found between calculated values and

measured values of the absorption coefficient; these were tentatively attributed to the presence of inhomogeneities.

InP is a semiconductor which recently has been receiving a great deal of attention as a potential substitute for GaAs in a number of microwave and optoelectronic applications. Rode (56) calculated the electron mobility in InP using an approach similar to one used for GaAs (48), but neglecting ionized impurity scattering. He showed that theoretical mobility limits agree with experimental data obtained with good quality, uncompensated material. Only a limited effort has been directed toward the study of free carrier absorption in InP. There are just two pertinent experimental reports (57,58). Furthermore, the material parameters used in the theoretical analysis of free carrier absorption (50) have since been revised.

III.3 Motivation of the present study

The purpose of the present study is to carry out an investigation of the influence of the microdistribution of impurities on the material parameters pertinent to photovoltaic energy conversion. In the case of silicon, it is therefore in order to investigate the important properties of the oxygen impurity and in particular to clarify its role in thermal donor activation. A comparison of interstitial oxygen microprofiles with activated thermal donor microprofiles is very important in light of the identification of the species other than oxygen active in the mechanism of donor activation. It is the purpose of the present investigation to carry out such a comparison and to propose a model for the mechanism of thermal donor activation.

The direct influence of a particular thermal donor microdistribution on the conversion efficiency of an oxygen-doped structure is to

be investigated. The potential of such a structure for improved efficiency is to be considered.

In the case of III-V compounds, the influence of free carrier inhomogeneities on macroscopic material parameters is to be investigated. In the light of the potential of InP for high concentration photovoltaic applications (59), it is the purpose of the present study to extend to InP the procedure used by Walukiewicz et al (53) to determine the compensation ratio in GaAs. In such an investigation the effects due to inhomogeneities of the samples have to be taken into account.

III. BACKGROUND, EXPLORATORY MEASUREMENTS, APPARATUS AND PROCEDURE

III.1 Background

III.1a Infrared absorption

The concentration of interstitial oxygen in silicon on a macroscale can be determined from infrared transmissivity measurements of the 9 μm absorption band (9). This method can be extended to a microscale analysis by improving the resolution. Difficulties which will be discussed below made worthwhile exploring also other techniques, which are discussed in the appendix.

Infrared transmissivity techniques can be used to measure a wide range of impurities in silicon. The infrared transmissivity spectrum of silicon measured on a Fourier Transform Spectrometer between 4000 cm^{-1} and 400 cm^{-1} is shown in Fig. 3.1. The silicon sample used was n-type, P-doped with a carrier concentration of about 10^{17} cm^{-3}; a strong oxygen absorption band is present around 9 μm, a carbon absorption band is present around 16.5 μm and a free carrier absorption background which increases with wavelength is superimposed on the other bands.

The absorption coefficient α can be calculated from the transmissivity T for every wavelength using the expression (60)

$$T = \frac{(1 - R)^2 e^{-\alpha z}}{1 - R^2 e^{-2\alpha z}} \qquad (3.1)$$

where R is the reflection coefficient (~0.29 for silicon in this wavelength range) and z is the thickness of the sample. The term at the denominator takes into account multireflections inside the sample. For high absorbance, i.e., $\alpha z \gg 1$, multireflected beams become negligible with respect to the beam that passed through the sample only once, the term at the denominator

can be neglected and 3.1 becomes :

$$T = (1 - R)^2 \, e^{-\alpha z} \tag{3.2}$$

In general, absorption can be due to more than one process: then the total absorption coefficient is equal to the sum of the absorption coefficients relative to the respective processes. For example, at the peak of the oxygen absorption band (λ = 9.01 μm) the total absorption coefficient is

$$\alpha_T = \alpha_o + \alpha_L + \alpha_F \tag{3.3}$$

where α_o, α_L, α_F are the absorption coefficients due respectively to oxygen, a lattice vibration band and free carriers. The absorption coefficient α_L, due to the lattice vibration, is known to be about 0.4 cm^{-1} at room temperature (9); the absorption coefficient α_F is equal to the absorption coefficient of the background at the peak of the band (λ = 9.01 μm). In order to calculate α_F, it is necessary to plot the total absorption coefficient calculated from eq. 3.1 as a function of wavelength for the whole band, then join the two edges of the band with a straight line; α_F is then the value of the absorption coefficient on the straight line in correspondence of the wavelength of the peak. Then α_o can be obtained from eq. 3.3. If the transmissivities are not too small, they can be assumed to be linear with the respective absorption coefficients and a simplified procedure can be used to calculate α_o. In the plot of transmissivity versus wavelength, a straight line drawn between the two edges of the band (Fig. 3.2) defines a baseline transmissivity T_b at the wavelength of the peak. The absorption coefficient of the band (oxygen + lattice) $\alpha_o + \alpha_L$ can then be calculated from

$$\frac{I_o}{I_b} = e^{-(\alpha_o+\alpha_L)z} \tag{3.4}$$

The oxygen concentration can be obtained from

$$[O] = 4.81 \times 10^{17}\ \alpha_o \tag{3.5}$$

where [O] is in cm^{-3} and α_o in cm^{-1}. If the free carrier absorption is negligible ($\alpha_T = \alpha_o + \alpha_L$), the procedure described above is exact. There are obvious advantages in calculating α_T using eq. 3.4 rather than eq. 3.1: simplicity and elimination of influences of variations in R due to surface preparation.

Determination of oxygen microprofiles requires high resolution measurements of the absorption coefficient at 9 μm along a continuous line; such measurements can be made by scanning IR absorption using a CO_2 laser.

III.1b Multireflections and interference

The high spatial resolution achieved by this technique introduces some problems which were not present at a lower resolution. If $\alpha z \lesssim 1$, multireflections inside the sample cannot be neglected, as discussed above. If the light is coherent, the first beam interferes with the secondary beams with a phase which depends on the difference in optical paths, which is determined by the thickness d of the sample. For example, the difference in optical path between the first transmitted beam and the beam that underwent one multireflection is 2d; the two beams interfere constructively or destructively if the difference in optical path is equal respectively to an even multiple of a half wavelength or to an odd multiple of a half wavelength. Therefore, if the thickness varies by a half wavelength from one point to another in the sample, the interference will go from constructive

to destructive; this thickness variation Δd is

$$\Delta d = \frac{\lambda}{2n} \tag{3.6}$$

where n is the index of refraction of silicon. In the present case, $\Delta d \sim 1$ μm: variations in thickness for samples prepared using standard techniques often exceed this value. In the case of macroscale measurements generally variations in thickness $\gtrsim 1$ μm can be expected for the area over which the signal is averaged; it follows that the contributions from areas of constructive interference and areas of destructive interference average out. In the case of microscale measurements, the beam moves along areas of varying thickness and an alternating pattern of constructive and destructive interference results. Therefore, reliable microscale measurements require the elimination of multireflections.

As discussed above, multireflections are negligible for $\alpha z >> 1$; this condition seems difficult to achieve for the oxygen absorption in silicon since the oxygen absorption coefficient is typically a few cm^{-1} and thickness cannot exceed a few millimeters to retain the required spatial resolution.

III.1c Temperature dependence of the oxygen absorption band

The oxygen absorption coefficient is known to increase at low temperatures (3) and, in fact, low temperature absorption measurements have been used to increase the sensitivity of the macroscale analysis of oxygen in silicon (9). An increase in the oxygen absorption coefficient would alleviate the problem of multireflections in a microscale analysis; on the other hand, the wavelength of the peak decreases at low temperatures to reach ~8.8 μm at 4.2°K. Monochromatic light sources in this range are not

easily available and, in fact, the lowest stable wavelength attainable with a CO_2 laser is 9.174 μm which is at about half-width of the oxygen absorption band at room temperature. Extrapolating low temperature data to temperatures above room temperature, an increase in the peak wavelength can be expected so that the peak would move closer to the CO_2 laser line available. At the same time, the oxygen absorption coefficient is expected to decrease slightly and the free carrier absorption is expected to increase greatly due to thermal generation of carriers. The combined effect would probably be a large increase in the total absorption coefficient at 9.174 μm, which could conceivably alleviate the problem of multireflections for a micro-scale analysis.

These speculations were based on extrapolation of low temperature data since no investigations of the oxygen absorption band above room temperature have been reported. Therefore, exploratory measurements were made to investigate the high temperature behavior of the oxygen absorption band in silicon.

III.2 Exploratory measurements

A Fourier Transform Spectrometer was used to measure the infrared transmissivity spectrum between 4000 cm^{-1} and 400 cm^{-1} for five silicon samples; the diameter of the beam was about 1 cm. The samples were placed in a heater and the temperature was monitored by a thermocouple. Four of the samples were Czochralski grown, had oxygen content in the vicinity of 10^{18} cm^{-3} and were doped respectively with B, Ga, In, P; one sample was grown by the float zone technique and had a low oxygen content.

The total absorption coefficient α_T at the peak of the oxygen absorption band was calculated as a function of temperature using eq. 3.1; results are shown in Fig. 3.3. The large increase with temperature observed is

largely due to an increase in the free carrier absorption background caused by thermal generation of free carriers. To separate the free carrier contribution, the absorption coefficient $\alpha_o + \alpha_L$ relative to the band was calculated using eq. 3.4; results are shown in Fig. 3.4. The increase in absorption coefficient with temperature is much larger for the float zone sample than for the high oxygen content samples. In the float zone sample the absorption band is due almost exclusively to the lattice band ($\alpha_o << \alpha_L$) while for the other samples both the oxygen absorption and the lattice absorption have to be taken into account. The oxygen absorption coefficient for the four samples of high oxygen content was found as a function of temperature by subtracting the lattice contribution which is assumed to be equal to the absorption coefficient of the float zone sample; results are shown in Fig. 3.5. It is seen that the oxygen absorption coefficient decreases with temperature, in agreement with an extrapolation of the low temperature data obtained by Hrostowski and coworkers (3,4). It is important to notice that the band broadened with increasing temperature, so that the total strength of the band remained approximately constant, again in agreement with Hrostowski.

The total absorption coefficient at 10 μm calculated using eq. 3.1 is shown as a function of temperature in Fig. 3.6. At 10 μm no absorption band is present so that the absorption is due only to free carriers. As expected, all the samples have a similar behavior except for the In-doped sample. In fact, the level of the indium acceptor in silicon is at 0.16 eV

above the valence band (61) and not all indium atoms are ionized at room temperature; an increase in temperature causes ionization of indium atoms and therefore an initial sharper increase in free carriers than in the other samples.

The wavelength of the oxygen absorption peak is plotted in Fig. 3.7 as a function of temperature for the four samples of high oxygen content. The peak wavelength increases linearly with temperature, again in agreement with an extrapolation of low temperature data (3,4). The peak wavelength did not shift appreciably with temperature for the float zone sample, as expected for a lattice band.

The present results extend to a temperature range previously not investigated and confirm the validity of the proposed model (2-4) for the infrared absorption of interstitial oxygen.

It is interesting to note that the wavelength of the oxygen absorption peak is equal to 9.174 μm, the lowest stable wavelength of the CO_2 laser, at about 560°K (Fig. 3.7). At this temperature the total absorption coefficient for the samples investigated is between 6 cm^{-1} and 9 cm^{-1} (Fig. 3.3) which are values still too low to achieve the condition $\alpha z >> 1$ necessary to eliminate multireflections. The wavelength of the peak increases further at higher temperatures and reaches 9.24 μm at 660°K (Fig. 3.7); at this temperature the total absorption coefficient is around 15 cm^{-1} (Fig. 3.3) and the condition $\alpha z > 1$ can be achieved with thicknesses of a few millimeters. Various CO_2 laser lines are available in this wavelength range, but the decrease in oxygen absorption coefficient with temperature (Fig. 3.5) reduces the sensitivity of the technique for wavelengths higher than 9.174 μm.

A further problem is caused by the variation of the index of refraction of silicon with temperature (62); a small variation in index of refraction causes a variation in the optical path. If some interference is still present, a variation in the optical path causes a variation in the intensity of the transmitted signal. Therefore, a high degree of temperature stability and homogeneity in temperature spatial distribution is necessary. Even if all interference has been eliminated by a high value of αz, temperature fluctuations cause changes in absorption coefficient.

It can be concluded that high temperature measurements of oxygen microprofiles do not appear to be a convenient technique unless a high degree of temperature stability is achieved. Low temperature measurements could be a viable technique of higher sensitivity, provided that monochromatic light sources of appropriate wavelength are available and a high degree of temperature stability can be achieved.

III.3 Apparatus and procedure

III.3a Antireflection coating

Another approach to the problem of the elimination of multireflections is to reduce the reflection coefficient, instead of increasing the absorption coefficient. An antireflection coating can be used to reduce the reflection coefficient; contemporary to the present work an AR coating was successfully employed by Ohsawa et al (63) to obtain oxygen profiles in silicon crystals by scanning IR absorption with a 200 μm resolution using a semiconductor laser.

The use of a single layer of low index of refraction as a means of suppressing the reflection from a surface is well-known (64). The reflectivity at normal incidence of a layer of index of refraction n_1 covering a material of index of refraction n_2 is given by

$$R = \frac{r_1 + r_2 e^{-2i\delta_1}}{1 + r_1 r_2 e^{-2i\delta_1}} \tag{3.7}$$

where δ_1 is the change in phase of the beam on traversing the film and

$$r_1 = \frac{n_o - n_1}{n_o + n_1} \tag{3.8}$$

$$r_2 = \frac{n_1 - n_2}{n_1 + n_2} \tag{3.9}$$

and n_o is the index of refraction of air. At the wavelength for which the optical thickness of the film is one-quarter wavelength, the beams reflected from the upper and lower surfaces of the film differ in phase by π. Setting $\delta_1 = \pi$ in eq. 3.7, the reflectivity of the film-covered surface is zero if $r_1 = r_2$. Using eq. 3.8 and 3.9, the following condition on the indexes of refraction is obtained:

$$n_1 = \sqrt{n_o n_2} \tag{3.10}$$

Using the value $n_2 = 3.42$ for the room temperature index of refraction for silicon at 9 μm, the value $n_1 = 1.85$ is obtained for the index of refraction of the coating. A single layer quarter-wavelength coating of zinc sulfide ($n = 2.25$) (65) can attain a substantial reduction in reflectivity.

The spectrum of a silicon sample with an AR coating was measured with a Fourier Transform Spectrometer between 4000 cm^{-1} and 400 cm^{-1} and is shown in Fig. 3.8. The transmissivity is greatly increased in the vicinity of the 9 μm absorption band due to the reduction in reflection coefficient. The transmissivity oscillates as a function of wavelength

due to an alternating pattern of constructive and destructive interference in the AR coating. The absorption coefficient was calculated using eq. 3.4; this value substituted in eq. 3.1 gives a value for the reflection coefficient R = 0.07. This value can be compared to the value R = 0.29 without AR coating.

III.3b Laser IR absorption scanning technique

The experimental set-up for the laser IR absorption scanning technique is shown in Fig. 3.9 and is similar to the one used to determine dopant concentration profiles in silicon (60). Using this apparatus oxygen microprofiles can be reliably determined on silicon samples with an AR coating at room temperature. The light source is a CO_2 laser Molectron model IR 250; its wavelength can be tuned between 9.174 μm and 10.94 μm. The beam emitted by the laser has a diameter of about 5 mm; it goes through a chopper PAR model 194 set at a reference frequency, is reflected by a mirror and focused by a 25 cm focal length CaF_2 lens onto the sample mounted on an x-y moving stage complete with a motor drive. After being transmitted through the sample, the beam is detected by a germanium piroelectric detector Molectron model P3-01 in front of which a 30 μm pinhole is placed to increase the resolution. The detected signal is amplified by a lock-in amplifier PAR model HR-8 locked onto the reference frequency set by the chopper and recorded on a chart recorder HP model 7100B. Transmissivity microprofiles can be obtained recording the transmitted intensity as the sample is moved through the beam by the motor drive. A measurement of the transmissivity with no sample in the beam allows to obtain a calibration for the transmissivity microprofile. The power and the wavelength of the laser can be monitored respectively by a power meter Coherent Radiation model 201 and by a spectrum analyzer,

Optical Engineering model 16-A, after removing the mirror.

The 25 cm focal length lens was chosen to optimize the size of the beam. A laser beam can be focused to a spot whose size is directly proportional to the focal length of the lens and, in addition, depends on the divergence of the laser, on the distance from the laser and on the wavelength. The size of the spot attained is also inversely proportional to the divergence of the beam after being transmitted through the lens. The experiment discussed here requires minimum size of the beam over the whole thickness of the sample, i.e., a few millimeters. A computer program developed by the Laser Group at MIT was used to determine the optimum focal length: it was found that a 25 cm focal length lens maintains the size of the beam around 200 - 300 μm for a few millimeters. Shorter focal length lenses gave smaller spots which diverged to much larger sizes over a few millimeters, and larger focal length lenses did not give small enough beam diameters.

The resolution is not limited to 300 μm because of the 30 μm pinhole placed in front of the detector; the pinhole is at an angle with respect to the beam to prevent parts of the beam which might have been reflected by the surface around the pinhole from reaching the detector after a second reflection on the sample surface.

The laser wavelength used for the microscale measurements (9.174 μm) falls at about half-width of the oxygen absorption band. A ratio of the absorption coefficient at the peak $\alpha_o + \alpha_L$ and of the absorption coefficient at 9.174 μm, $\alpha(\lambda = 9.174\ \mu m)$, was calculated from the spectrum of Fig. 3.11:

$$\frac{\alpha_o + \alpha_L}{\alpha(\lambda = 9.174\ \mu m)} = 1.95 \qquad (3.11)$$

This ratio was used to obtain α_o and then the oxygen concentration [O] from eq. 2.1.

III.3c Spreading resistance technique

The free carrier concentration microprofiles were determined by two probe spreading resistance measurements (44) at 10 μm intervals with 50 μm spacing between the probes after removing the AR coating and polishing the surface. The spreading resistance apparatus used was a Solid State Measurements model ASR-100.

Figure Captions

Fig. 3.1 Infrared transmissivity of a silicon sample as a function of wavenumber between 4000 cm^{-1} and 400 cm^{-1}. The carrier concentration n is ~10^{17} cm^{-3}.

Fig. 3.2 Transmissivity of a silicon sample as a function of wavenumber in the region of the oxygen absorption peak. The baseline transmissivity T_b and the transmissivity at the oxygen absorption peak T_o are shown.

Fig. 3.3 Total absorption coefficient α_T at the oxygen absorption peak as a function of temperature T: ○ Si B-doped, □ Si P-doped, • Si Ga-doped, ▲ Si In-doped, △ Si float zone.

Fig. 3.4 Absorption coefficient of the 9 μm band $\alpha_o + \alpha_L$ calculated according to eq. 3.4 as a function of temperature T: samples are the same as in Fig. 3.6.

Fig. 3.5 Oxygen absorption coefficient α_o calculated subtracting the lattice contribution α_L as a function of temperature T; samples are the same as in Fig. 3.6 except for the float zone sample.

Fig. 3.6 Free carrier absorption coefficient at λ = 10 μm. $\alpha_{10\ \mu m}$ as a function of temperature T; samples are the same as in Fig. 3.6.

Fig. 3.7 Wavelength of the oxygen absorption peak λ_o as a function of temperature T; samples are the same as in Fig. 3.6 except for the float zone sample.

Fig. 3.8 Infrared transmissivity of a silicon sample with AR coating as a function of wavenumber between 4000 cm^{-1} and 400 cm^{-1}.

Fig. 3.9 Schematic representation of IR laser scanning absorption apparatus for oxygen microprofiling.

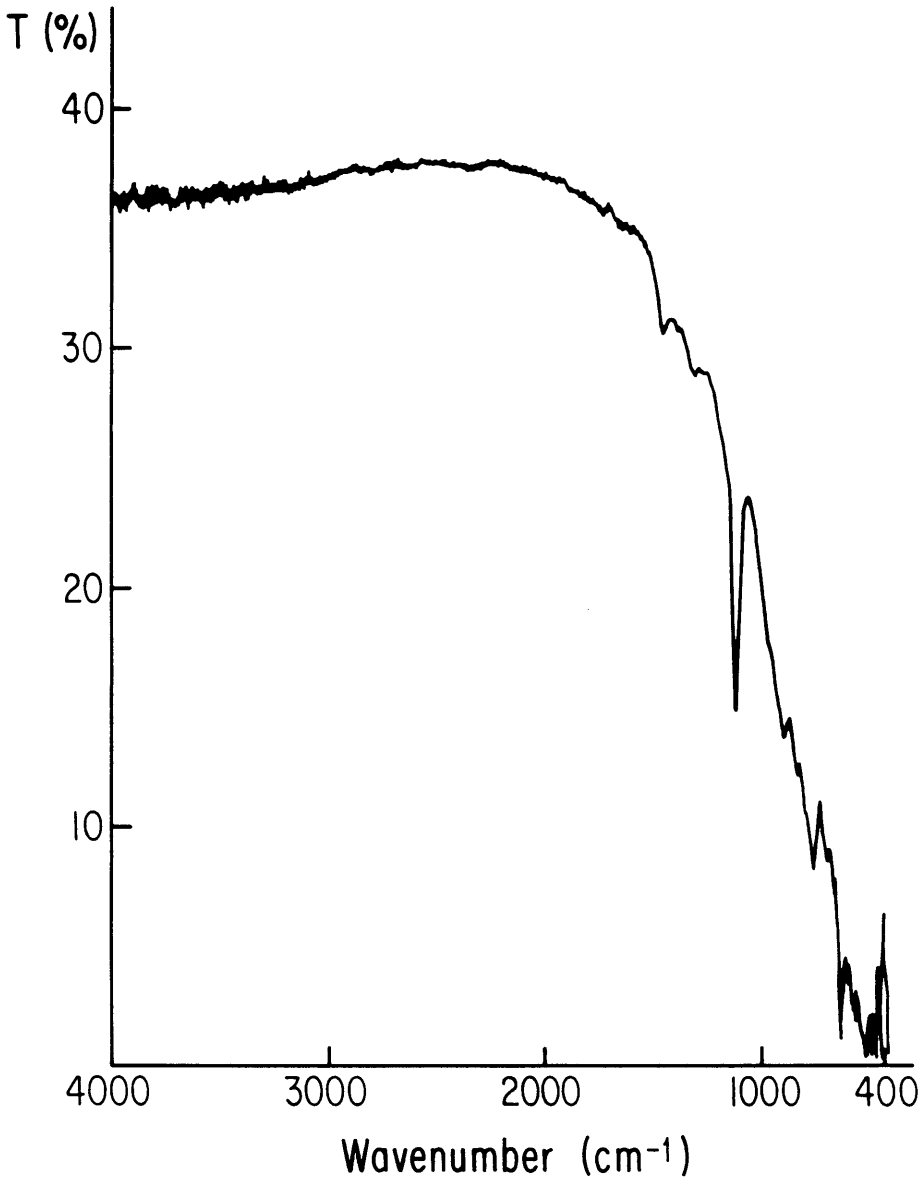

Fig. 3.1

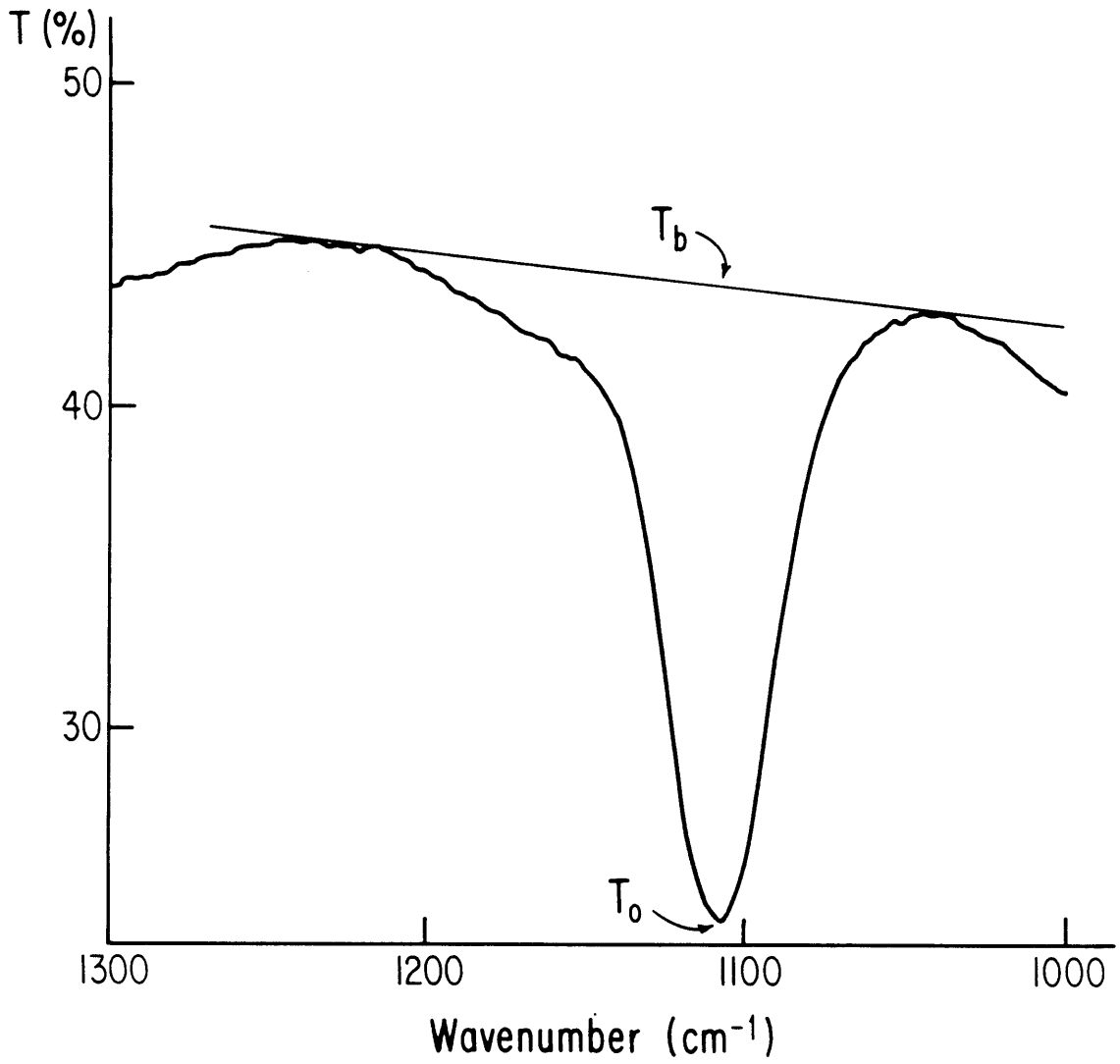

Fig. 3.2

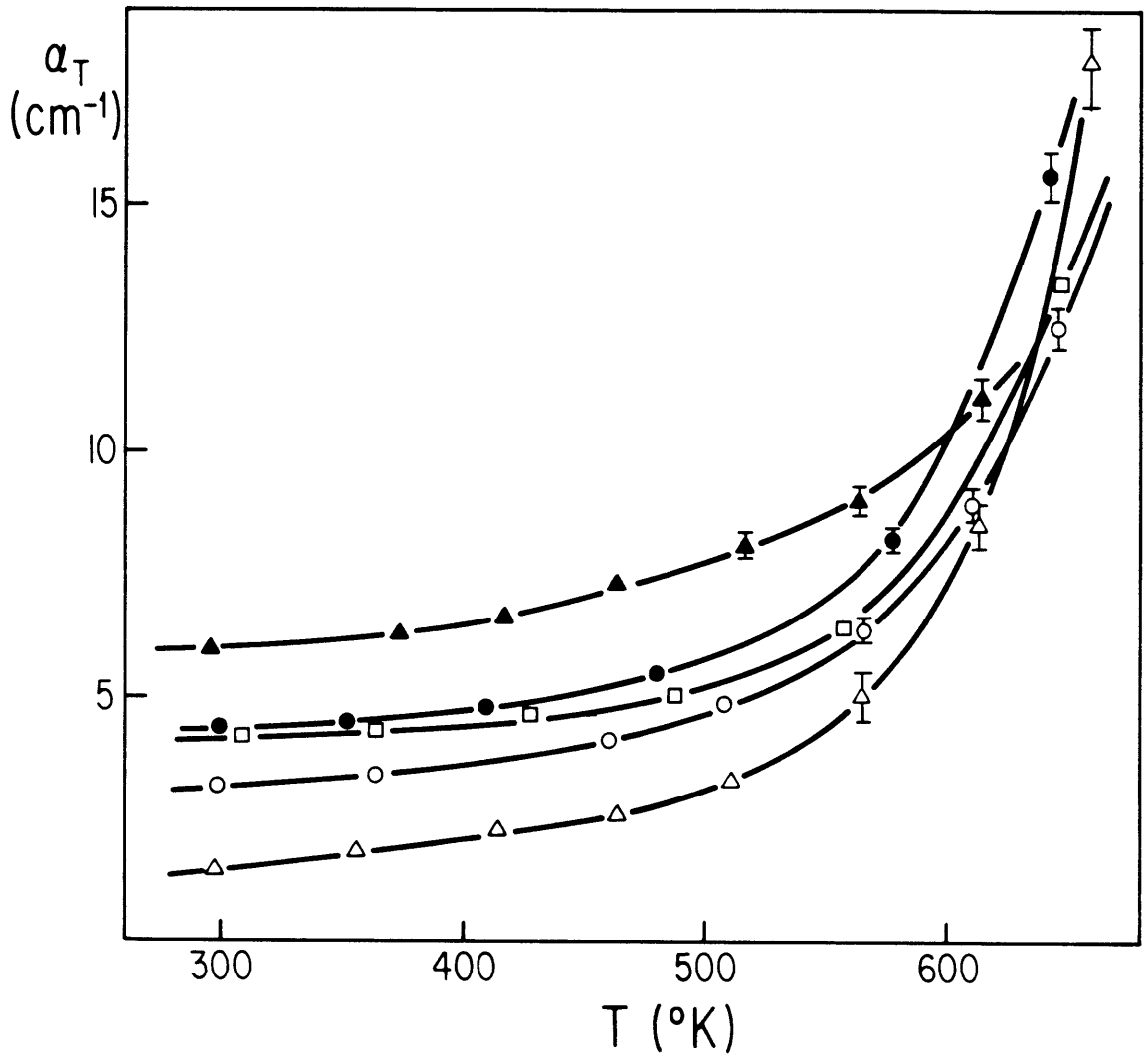

Fig. 3.3

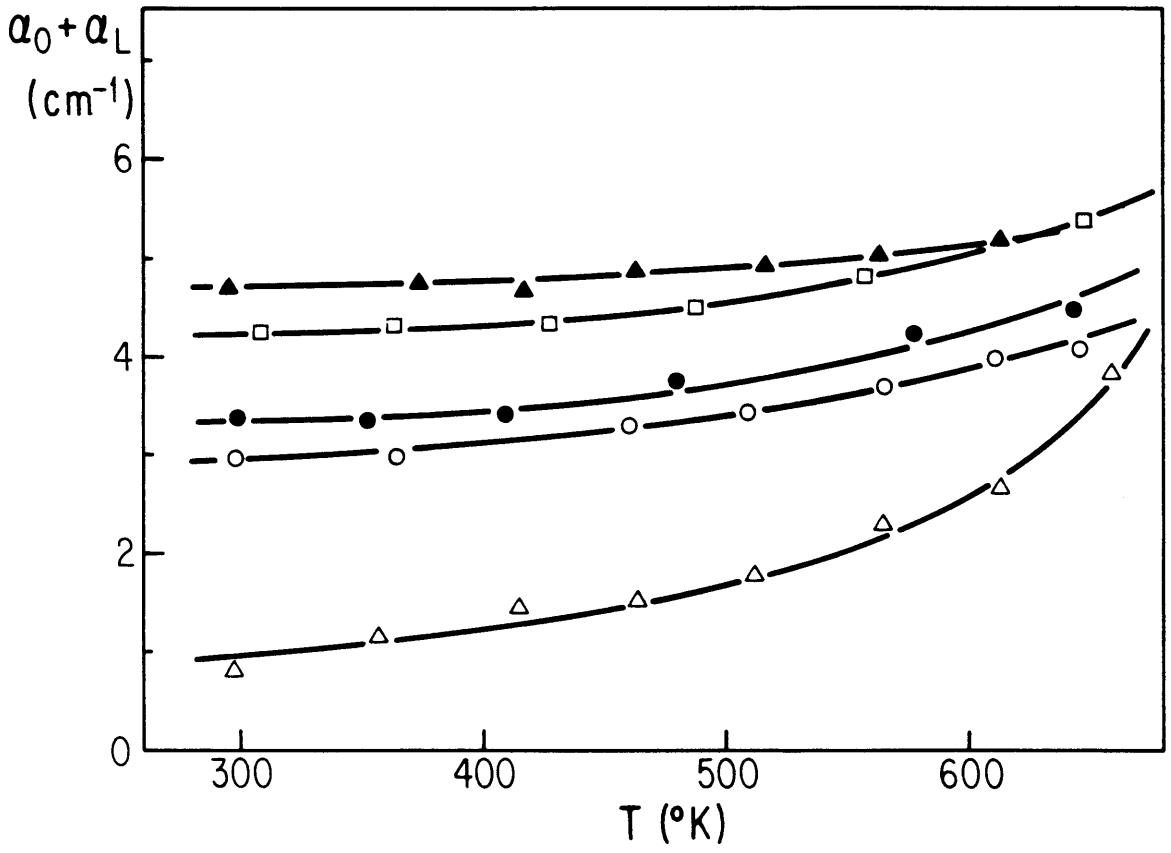

Fig. 3.4

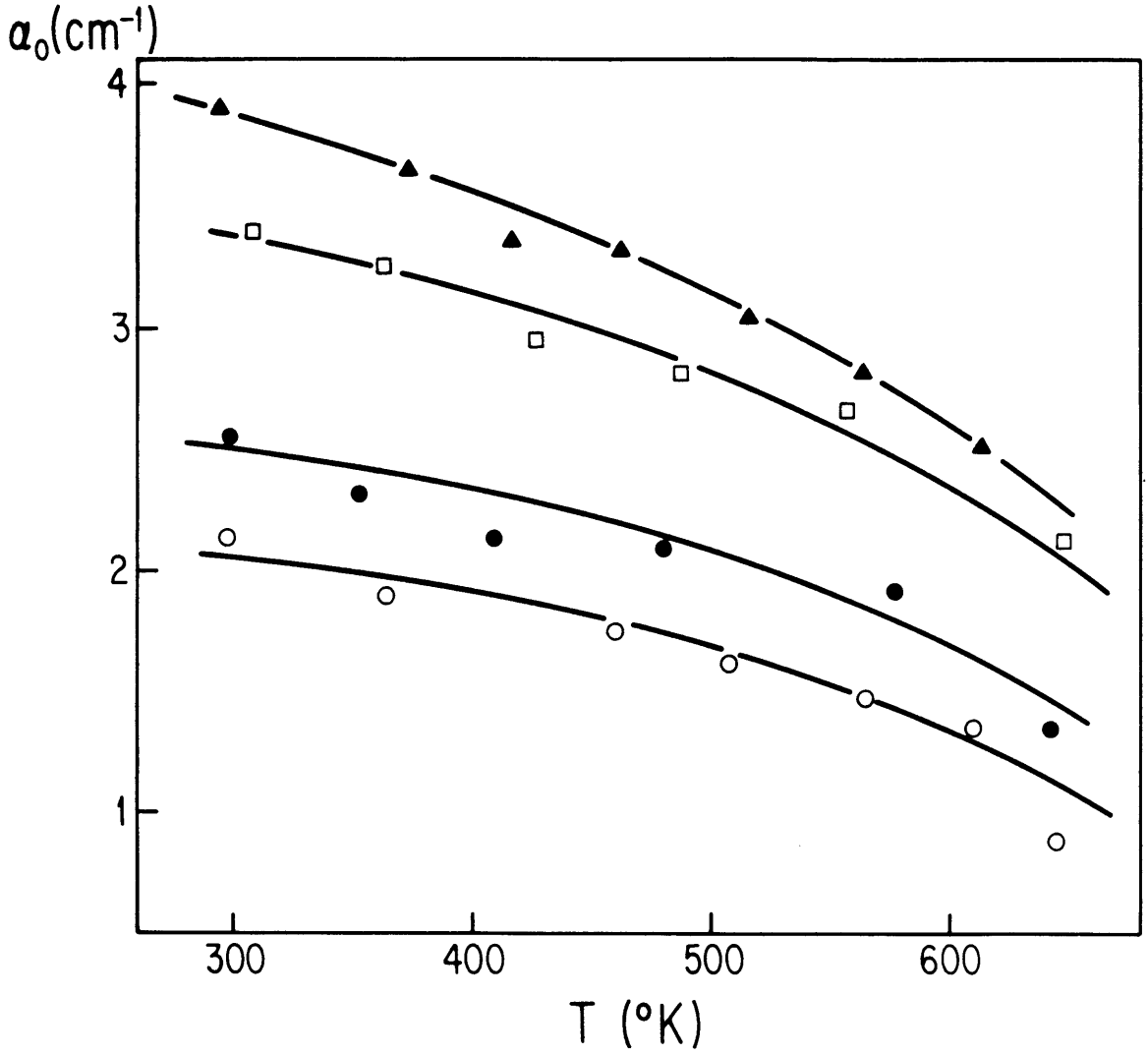

Fig. 3.5

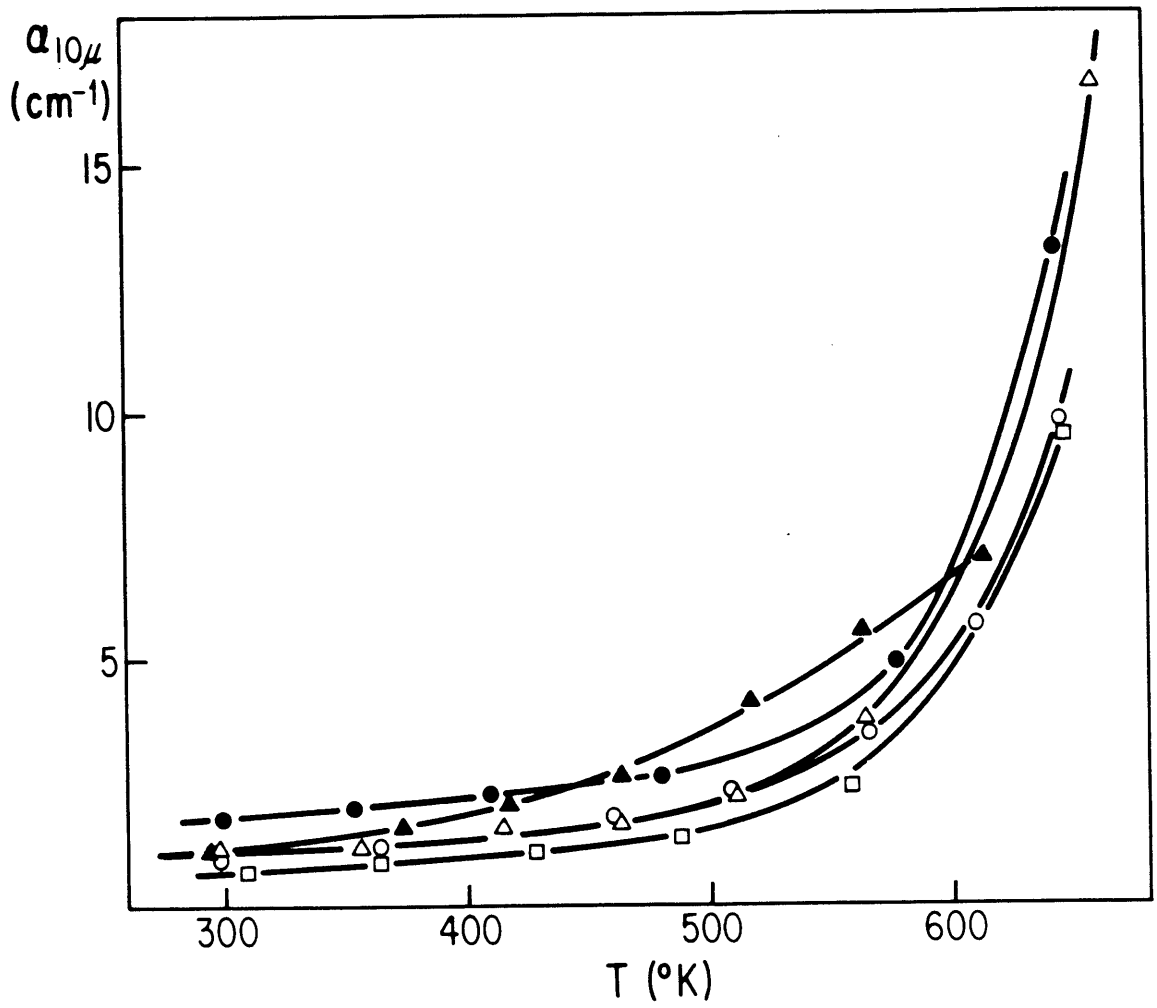

Fig. 3.6

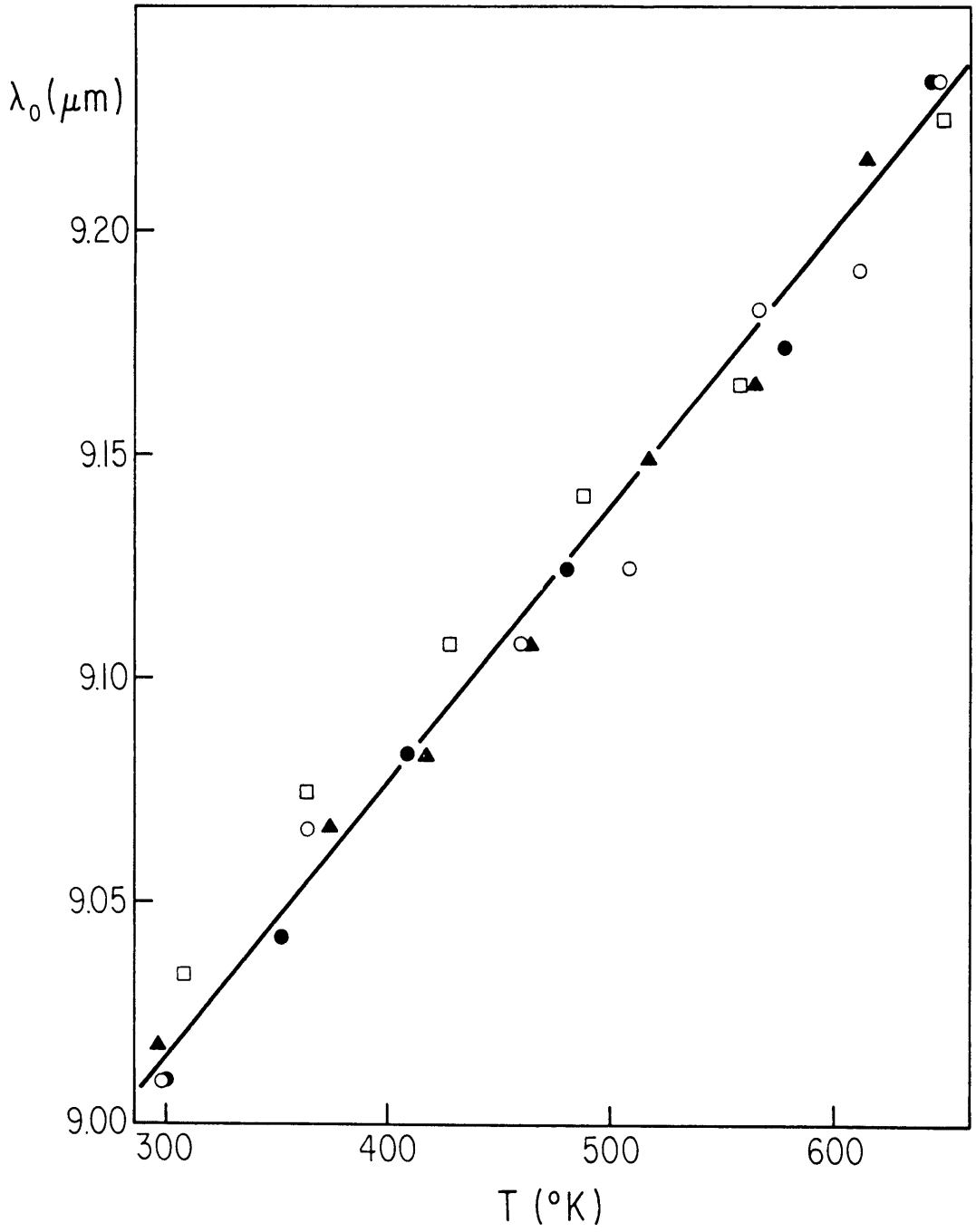

Fig. 3.7

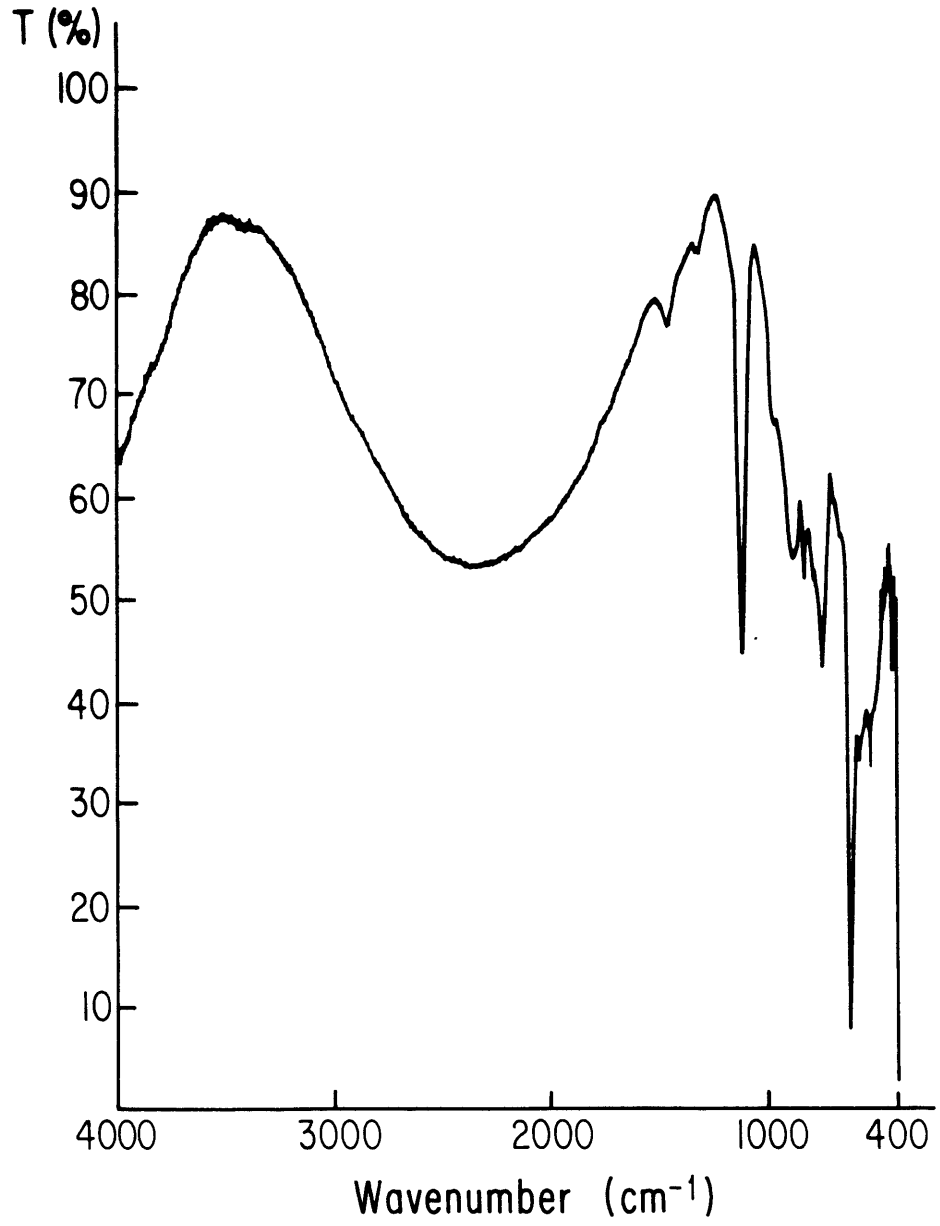
T (%)
100
90
80
70
60
50
40
30
20
10
4000
3000
2000
1000
400
Wavenumber (cm-1)

Fig. 3.8

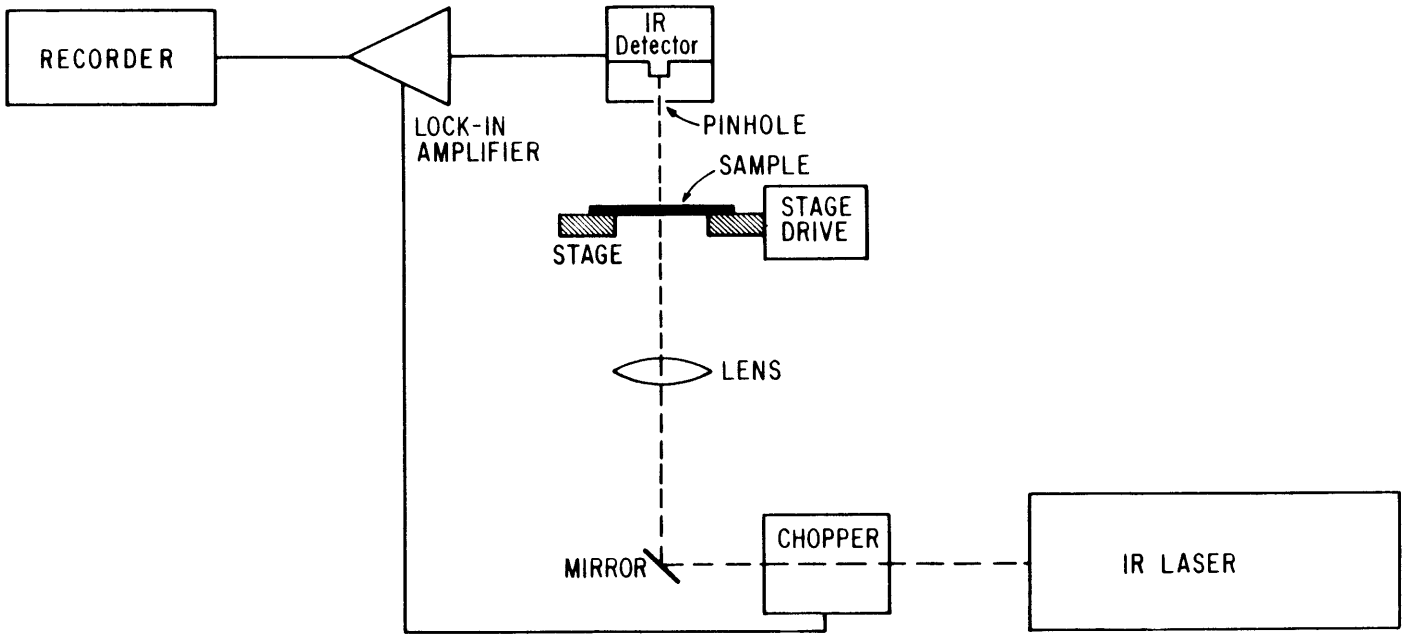
RECORDER
LOCK-IN
AMPLIFIER
IR
Detector
PINHOLE
SAMPLE
STAGE
DRIVE
STAGE
LENS
MIRROR
CHOPPER
IR LASER

Fig. 3.9

IV. EXPERIMENTAL RESULTS FOR B-DOPED SILICON

IV.1 Correlation between oxygen microprofiles and thermal donor microprofiles

All the samples investigated in this section were cut parallel to the growth direction from a<111> Czochralski-grown dislocation-free commercial B-doped silicon crystal whose regular diameter overall length was approximately 52 mm and initial p-type average carrier concentration was $\sim 1.5 \times 10^{15}$ cm^{-3}. They were not submitted to any thermally stabilizing heat treatment prior to experimentation.

Slices were cut at different distances from the periphery of the crystal; their infrared spectrum was measured between 4000 cm^{-1} and 400 cm^{-1} using a Fourier Transform Spectrometer. The oxygen and carbon concentrations were calculated from eq. 3.1 and ref. 28 and are shown in Fig. 4.1 as a function of distance from the periphery of the crystal. As expected, the oxygen concentration decreases sharply toward the periphery while the carbon concentration stays fairly constant.

A sample was cut parallel to the growth direction and through the rotation axis; both parallel faces of the sample were polished to a mirror finish and coated with a single layer quarter-wavelength zinc sulfide antireflection coating. Oxygen concentration microprofiles were obtained by the scanning IR absorption technique discussed in Section III. An oxygen concentration microprofile taken parallel to the growth direction 6 mm from the periphery of the crystal is shown in Fig. 4.2a. It is seen that the oxygen concentration fluctuates from about 1×10^{18} to 1.5×10^{18} cm^{-3}. The fluctuations are more random than periodic, indicative of turbulence convection in the melt during growth [44]. A carrier concentration profile along the IR transmission scan of Fig. 4.2a exhibited essentially no fluc-

tuations, typical for B-doped crystals (44).

Subsequently, the silicon slice was heat-treated at 450°C for 4 hours to activate thermal donors, and a spreading resistance scan was taken along the line of the IR absorption scan. The results are shown in Fig. 4.2b. The hole concentration is decreased from its original value of 1.5×10^{15} cm^{-3} by the amount of activated thermal donors. It is seen that the oxygen and carrier concentration profiles exhibit in general similar features. As an average, the donor concentration is about three orders of magnitude smaller than the oxygen concentration.

A close examination of profiles 4.2a and 4.2b shows that in some locations there is no direct correspondence between oxygen and activated donor concentrations. For example, in location B, the concentration of oxygen is greater than that in location A, whereas the corresponding thermal donor concentration in B is smaller than in A. Similarly, in location C the oxygen concentration exhibits a peak which does not appear in the carrier concentration profile.

Upon heat treatment of the slice at 650°C for 4 hours, the thermal donors, as expected, were annihilated; the slice was then heat-treated again at 450°C for 8 hours. The resulting carrier concentration profile is shown in Fig. 4.2c. It is seen that in this case the overall activated donor concentration is significantly smaller than before the 650°C heat treatment, in spite of the longer heat treatment time at 450°C. Here, again (as in Fig. 4.2b), in locations A and B there is no direct correspondence between oxygen and thermal donor concentration. However, the oxygen concentration peak in location C becomes visible in Fig. 4.2c, whereas it was not present in Fig. 4.2b.

It is important to point out that with each subsequent heat treatment of the same slice at 650°C and then at 450°C the average concentration of the activated thermal donors continuously decreased. In the present case, after a cumulative heat treatment of about 15 hours at 650°C the thermal donor concentration activated by heat treatment at 450°C for a few hours was greatly reduced.

The discrepancies between oxygen and thermal donor concentrations were found to be very pronounced near the periphery of the crystal. An oxygen concentration profile taken parallel to the growth direction 4.5 mm from the periphery of the same crystal and the corresponding carrier concentration profile taken after heat treatment at 450°C for 4 hours are shown in Figs. 4.3a and 4.3b, respectively. As already shown in Fig. 4.1, the mean concentration of interstitial oxygen is smaller near the periphery than toward the center of the crystal.

The striking result presented in Fig. 4.3b is that in entire regions no thermal donors were formed, and, in fact, the carrier concentration in some of these regions (region B; $p \sim 1.5 \times 10^{15}$ cm^{-3}) is the same as prior to the heat treatment. There are, of course, regions (region A) in which activation of thermal donors took place. After the thermal donors were annihilated by a heat treatment at 650°C for 4 hours, the slice was heat-treated again at 450°C for 8 hours. The resulting carrier concentration profile is shown in Fig. 4.3c. It is seen that activation of thermal donors took place in regions in which activation was not pronounced or not observed after the first heat treatment (region B, for example). In regions where pronounced activation took place after the first heat treatment, the concentration of thermal donors decreased following the second 450°C heat

treatment (for example, region A) consistent with results presented in Fig. 4.2.

With subsequent heat treatments of the same slice at 650°C and then at 450°C the concentration of the thermal donors in the regions where activation had not taken place after the first heat treatment continued to increase to a maximum value and then decreased, eventually reaching very small values (Fig. 4.3d). Thus, the thermal donor activation behavior near the periphery and toward the center of the crystal is shown in Fig. 4.4.

A series of oxygen profiles taken on the same silicon crystal at various distances from the periphery (abscissa) are shown in Fig. 4.5. It is seen that the variations in oxygen concentration are more pronounced near the periphery of the crystal than near the center, as already reported in the literature (5). It is further seen that certain patterns of inhomogeneities persist from the periphery to the center of the crystal and clearly delineate a striation pattern. Two striation patterns are superimposed, one with a closer spacing between maxima and the other with a larger spacing between maxima and much more irregular. The former is due to rotation of the crystal through thermal asymmetries at the solid-liquid interface during growth; the latter is due to turbulence convection in the melt during growth. The corresponding carrier concentration profiles after a heat treatment at 450°C for 4 hours are shown in Fig. 4.6. Here again it is apparent that near the periphery of the crystal there are extended regions in which no donor activation took place during the initial heat treatment at 450°C.

The thermal donor concentration activated by a heat treatment at 450°C for 4 hours for various points along the scans of Fig. 4.6 is shown in Fig. 4.7 as a function of the oxygen concentration in the corresponding points of Fig. 4.5. A straight line giving the proportionality of the initial generation rate of donors with the fourth power of the oxygen concentration obtained by Kaiser (14) is also shown in Fig. 4.7. It is seen that, although Kaiser's law is followed on the average, the scatter in the experimental points is very large, reflecting the difference in activation rates between different regions which has been revealed by the microscale analysis.

The average thermal donor concentration as a function of distance from the periphery of the crystal, obtained by averaging the spreading resistance scans, is shown in Fig. 4.8a after a heat treatment at 450°C for 4 hours and in Fig. 4.8b after heat treatments at 450°C for 4 hours, at 650°C for 4 hours and at 450°C for 6 hours. Again here it is seen that after the second heat treatment the average activation is lower toward the center of the crystal, whereas it is higher toward the periphery, reflecting the presence of the areas whose activation is enhanced by heat treatment at 650°C already discussed.

It is apparent from these results that oxygen is not necessarily the controlling factor in the activation of thermal donors, as had already been deduced from a careful examination of the literature. Areas have been identified near the periphery of the crystal where the presence of another species that controls donor activation at least in the initial stage is evident.

IV.2 Microdefect distribution

It can be hypothesized that this species could be connected with crystal defects, which have already been shown to influence donor activation (30). DeKock (66) has shown that the distribution of microdefects in silicon is not uniform both in the radial and in the axial direction. He identified essentially two types of microdefects: B-defects, predominant toward the periphery of the crystal, and A-defects, predominant toward the center of the crystal. Various authors have also investigated the influence of heat treatments at various temperatures on microdefects and on their interaction with oxygen (44,63,67).

In the present work the microdefect distribution was investigated as a function of heat treatment in order to clarify its relationship with the unknown species that controls donor activation in some areas. A modified Sirtl etch was used to reveal microdefects (66); its composition was HF (49%):CrO_3 (33% acqueous solution) = 1:2. When used to etch polished silicon surfaces, A-defects are revealed by large etch pits, B-defects by small etch pits.

An axially cut B-doped silicon sample was heat treated for 4 hours at 450°C and the carrier concentration profile was measured by spreading resistance parallel to the direction of growth at 6 mm from the periphery of the crystal. The sample was then etched to reveal microdefects.

A series of microphotographs of the etched surface of the sample is shown in Fig. 4.9; the spreading resistance trace taken at 6 mm from the edge of the crystal is visible and the corresponding carrier concentration microprofile is shown above the microphotographs on the same scale. A detail of the etched surface is shown in Fig. 4.10b and the corresponding carrier concentration profile in Fig. 4.10a. It is seen that in areas

where donors have been activated, microdefects are larger and less dense (A-type) than in areas where no donors have been activated (where B-type defects are predominant). In correspondence of activated donors, grooves due to the preferential character of the etchant can be observed. This sample had also been etched prior to heat treatment; the microdefect distribution and structure were essentially the same, indicating little effect of the initial heat treatment at 450°C on microdefects.

Increasing the heat treatment time at 450°C, the density of the defects starts decreasing both for the A- and the B-type defects (Fig. 4.11). The crystal was then heat treated at 650°C and the same detail shown in Fig. 4.10b is shown in Fig. 4.10c after heat treatments for $15\frac{1}{2}$ hours at 450°C and for 4 hours at 650°C. It is seen that the density of defects in the previously activated area is reduced and that the defects in the previously non-activated area have increased in size and reduced in density, i.e., tend to become A-type. As already discussed above, upon further heat treatment at 450°C, activation takes place in areas where there was no activation upon the first heat treatment at 450°C. After long heat treatment times, both at 450°C and at 650°C, A-defects appear in all areas of the sample (Fig. 4.12).

From these results it is apparent that B-type defects hinder and A-type defects favor thermal donor formation; upon heat treatment at 650°C B-type defects tend to become A-type and therefore make thermal donor formation possible in areas previously unactivated.

Figure Captions

Fig. 4.1 o Oxygen concentration as a function of distance from the periphery of the crystal obtained from IR transmissivity measurements of the 9 μm band an samples cut at different distances from the periphery.

▲ Carbon concentration as a function of distance from the periphery of the crystal obtained from IR transmissivity measurements of the 16.5 μm band on samples cut at different distances from the periphery.

Fig. 4.2 (a) Oxygen concentration, [O], (O/cm^3) as a function of distance parallel to the direction of growth at a distance of 6 mm from the periphery of the crystal obtained by scanning IR absorption. (b) Hole concentration, [p], (p/cm^3) obtained with spreading resistance measurements along the same location as in (a) after 4 hrs. heat treatment at 450°C. (c) Hole concentration along the same location as in (a) after 4 hrs. heat treatment at 450°C followed by heat treatments for 4 hrs. at 650°C and 8 hrs. at 450°C.

Fig. 4.3 (a) Oxygen concentration, [O], (O/cm^3) as a function of distance parallel to the direction of growth at a distance 4.5 mm from the periphery of the crystal obtained by scanning IR absorption. (b) Hole concentration, [p], (p/cm^3) obtained with spreading resistance measurements along the same location as in (a) after 4 hrs. heat treatment at 450°C. (c) Hole concentration along the same location as in (a) after 4 hrs. heat treatment at 450°C followed by heat treatment for 4 hrs. at 650°C and 8 hrs. at 450°C. (d) Hole concentration as in (c) after following heat treatments for 4 hrs. at 650°C and 8 hrs. at 450°C.

Fig. 4.4 Thermal donor concentration after heat treatment cycles at 450°C, 650°C, 450°C as a function of cumulative 650°C heat treatment times.

Fig. 4.5 Oxygen concentration microprofiles in a silicon crystal at various locations (abscissa) from the periphery toward the center of the crystal. The distance between scans is 0.635 mm; the lowest scan is at 4.47 mm and the highest scan is at 9.55 mm from the periphery of the crystal.

Fig. 4.6 Carrier concentration microprofiles corresponding to the oxygen microprofiles of Fig. 4.5 after heat treatment at 450°C for 4 hours.

Fig. 4.7 Thermal donor concentration [n] activated by a heat treatment at 450°C for 4 hours as a function of interstitial oxygen concentration. The experimental points correspond to various

locations on the maps shown in Figs. 4.5 and 4.6. The solid line of slope 4 gives the dependence of the activated donor concentration on the fourth power of the oxygen concentration.

Fig. 4.8 Thermal donor concentration [n] activated by (a) ○ 4 hrs. at 450°C; (b) □ 4 hrs. at 450°C, 4 hrs. at 650°C and 6 hrs. at 450°C as a function of distance from the periphery of the crystal obtained averaging spreading resistance scans.

Fig. 4.9 Microphotographs of the surface of a Si sample heat-treated for 4 hrs. at 450°C; the spreading resistance trace was taken at 6 mm from the periphery of the sample and the carrier concentration profile obtained is shown above the microphotographs.

Fig. 4.10 (a) Carrier concentration profile taken at 6 mm from the periphery of a B-doped Si crystal heat treated at 450°C for 4 hrs. (b) Microphotograph of the surface of the same sample as in (a) etched with Sirtl etch; the spreading resistance trace corresponds to the carrier concentration profile in (a). (c) Microphotograph of the surface of the same sample heat treated at 450°C for 15½ hrs. and at 650°C for 4 hrs. etched with Sirtl etch; same location as in (b).

Fig. 4.11 Microphotograph of the surface of a sample heat treated at 450°C for 14 hrs. etched with Sirtl etch; location is about 1 cm from the periphery of the crystal.

Fig. 4.12 Microphotograph of the surface of a sample heat treated for 4 hrs. at 450°C, 4 hrs. at 650°C, 8 hrs. 450°C, 4 hrs. 650°C, 4 hrs. 450°C etched with Sirtl etch; location is about 4.5 mm from the periphery.

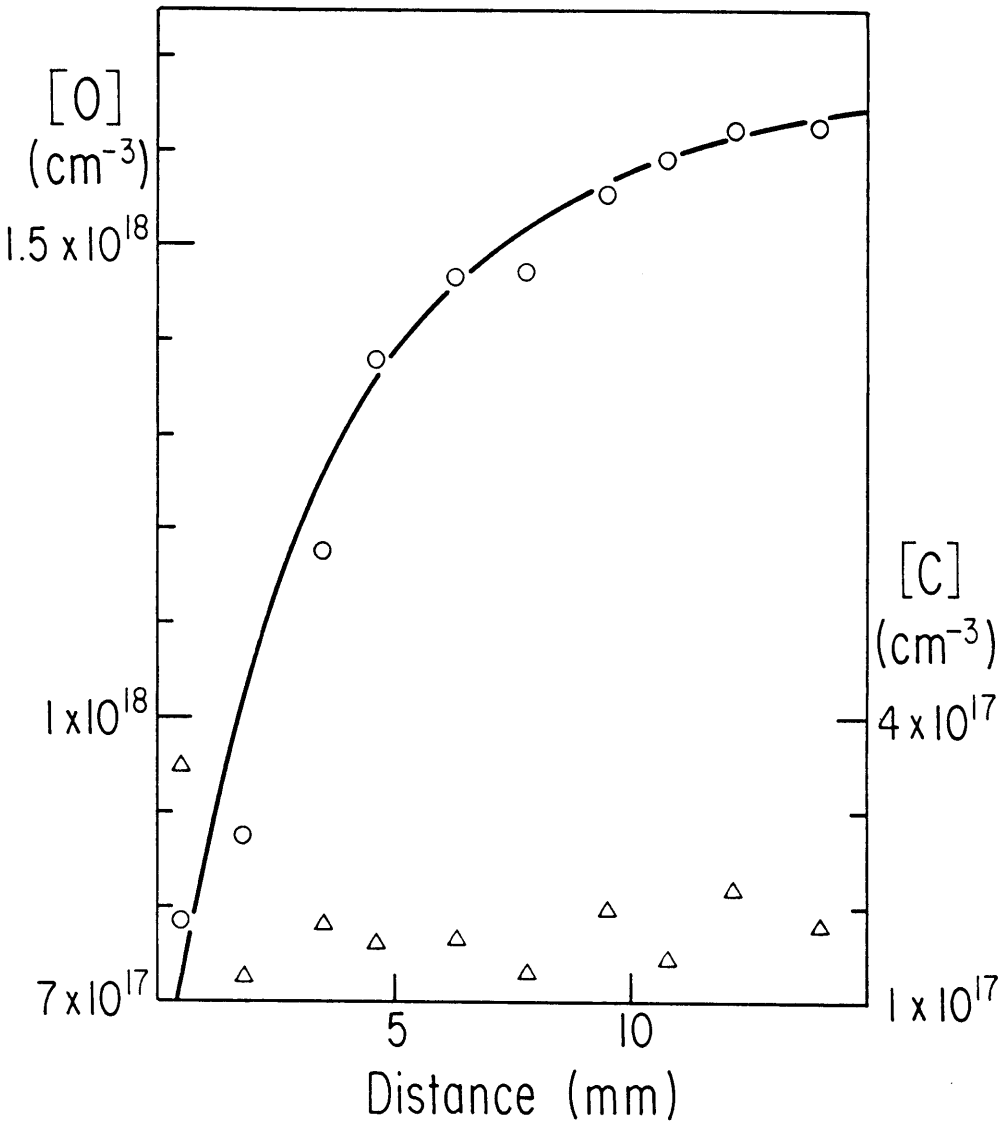
[O]
(cm^{-3})
1.5 x 10^{18}
1 x 10^{18}
7 x 10^{17}
[C]
(cm^{-3})
4 x 10^{17}
1 x 10^{17}
5
10
Distance (mm)

Fig. 4.1

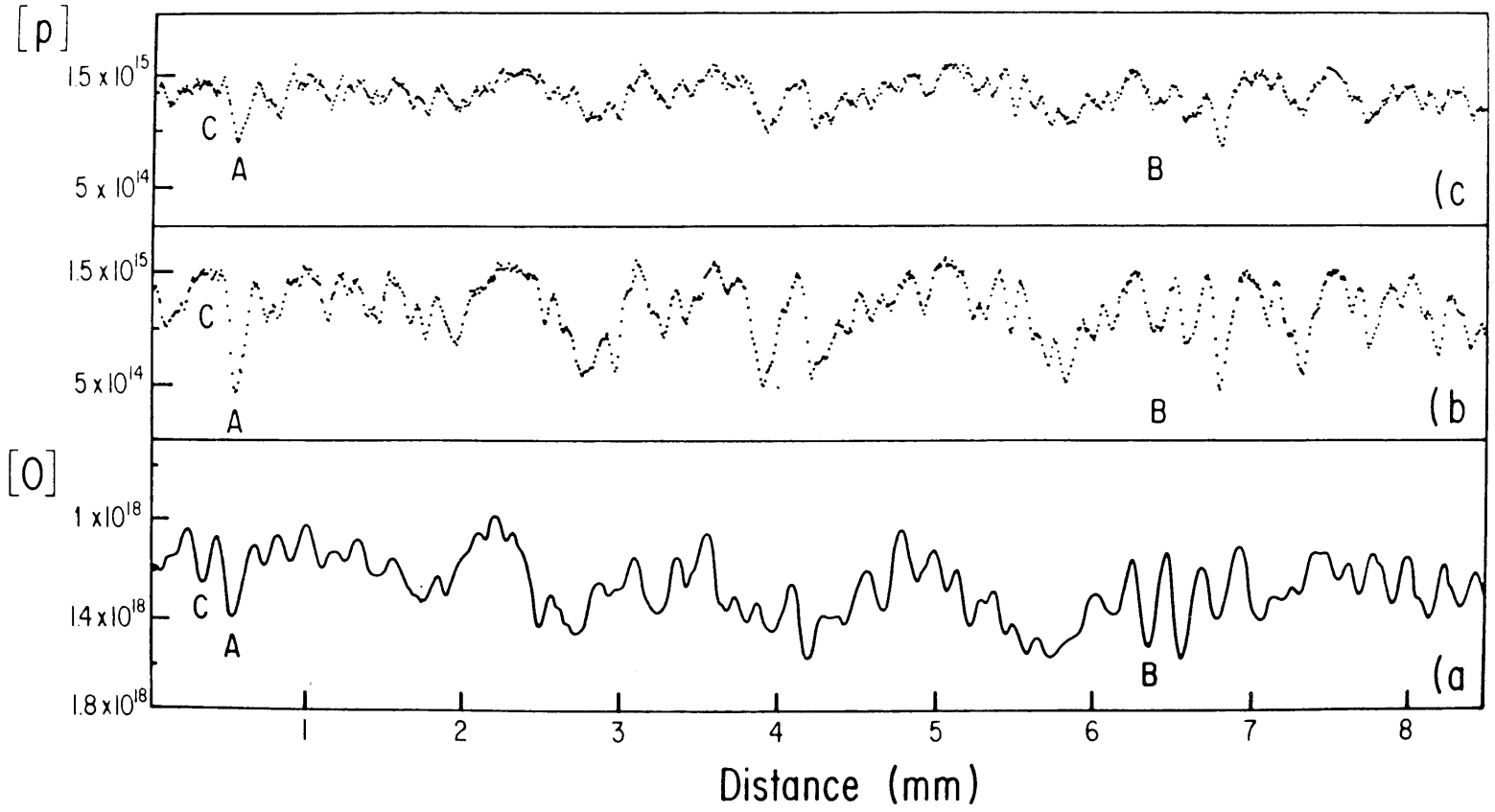
[p]
1.5 x 10^15
5 x 10^14
C
A
B
(c
1.5 x 10^15
5 x 10^14
C
A
B
(b
[O]
1 x 10^18
1.4 x 10^18
1.8 x 10^18
C
A
B
(a
1
2
3
4
5
6
7
8
Distance (mm)

Fig. 4.2

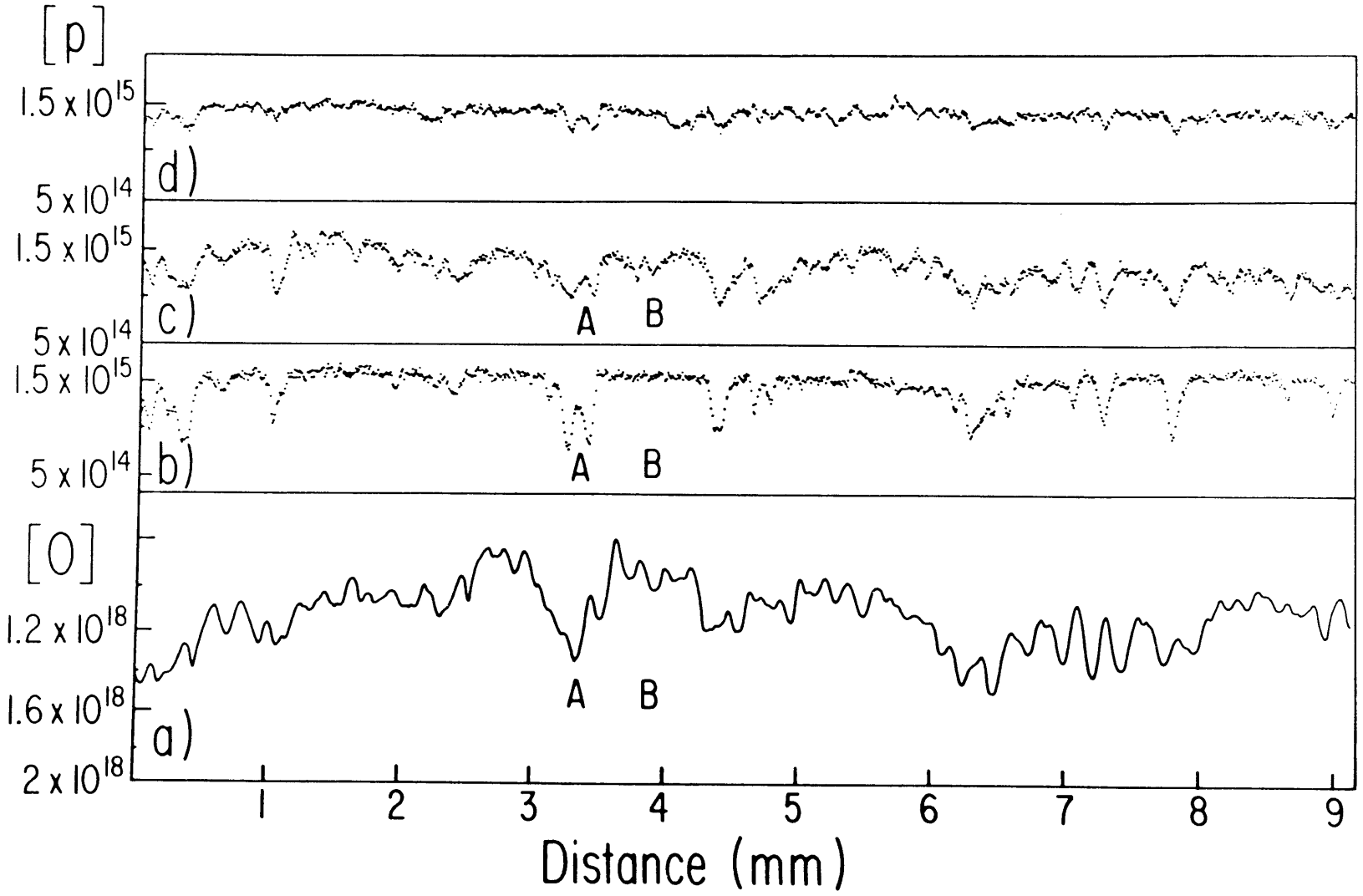
[p]
1.5 x 10^15
d)
5 x 10^14
1.5 x 10^15
c)
A B
5 x 10^14
1.5 x 10^15
b)
A B
5 x 10^14
[O]
1.2 x 10^18
1.6 x 10^18
a)
A B
2 x 10^18
1 2 3 4 5 6 7 8 9
Distance (mm)

Fig. 4.3

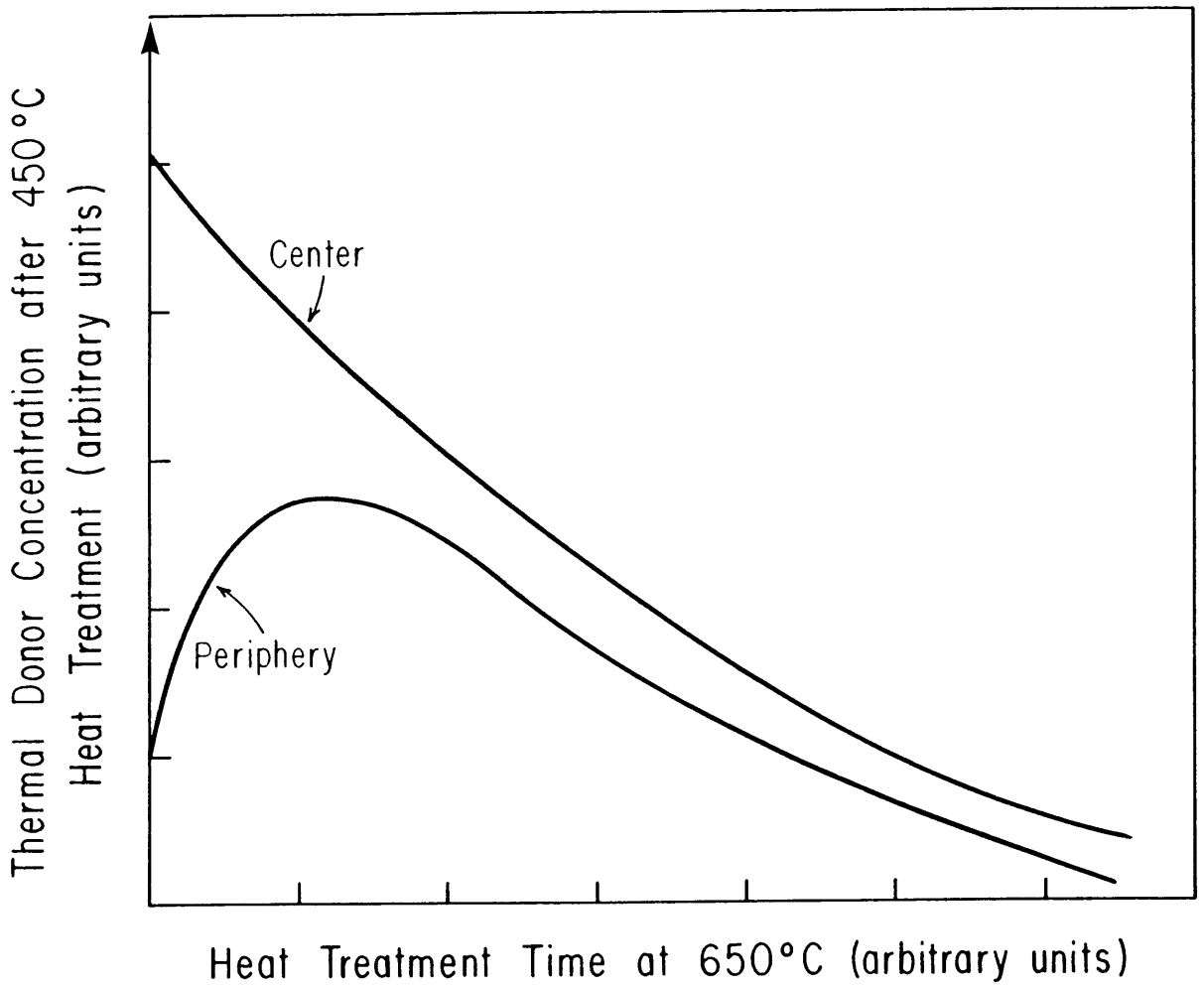
Thermal Donor Concentration after 450°C
Heat Treatment (arbitrary units)
Center
Periphery
Heat Treatment Time at 650°C (arbitrary units)

Fig. 4.4

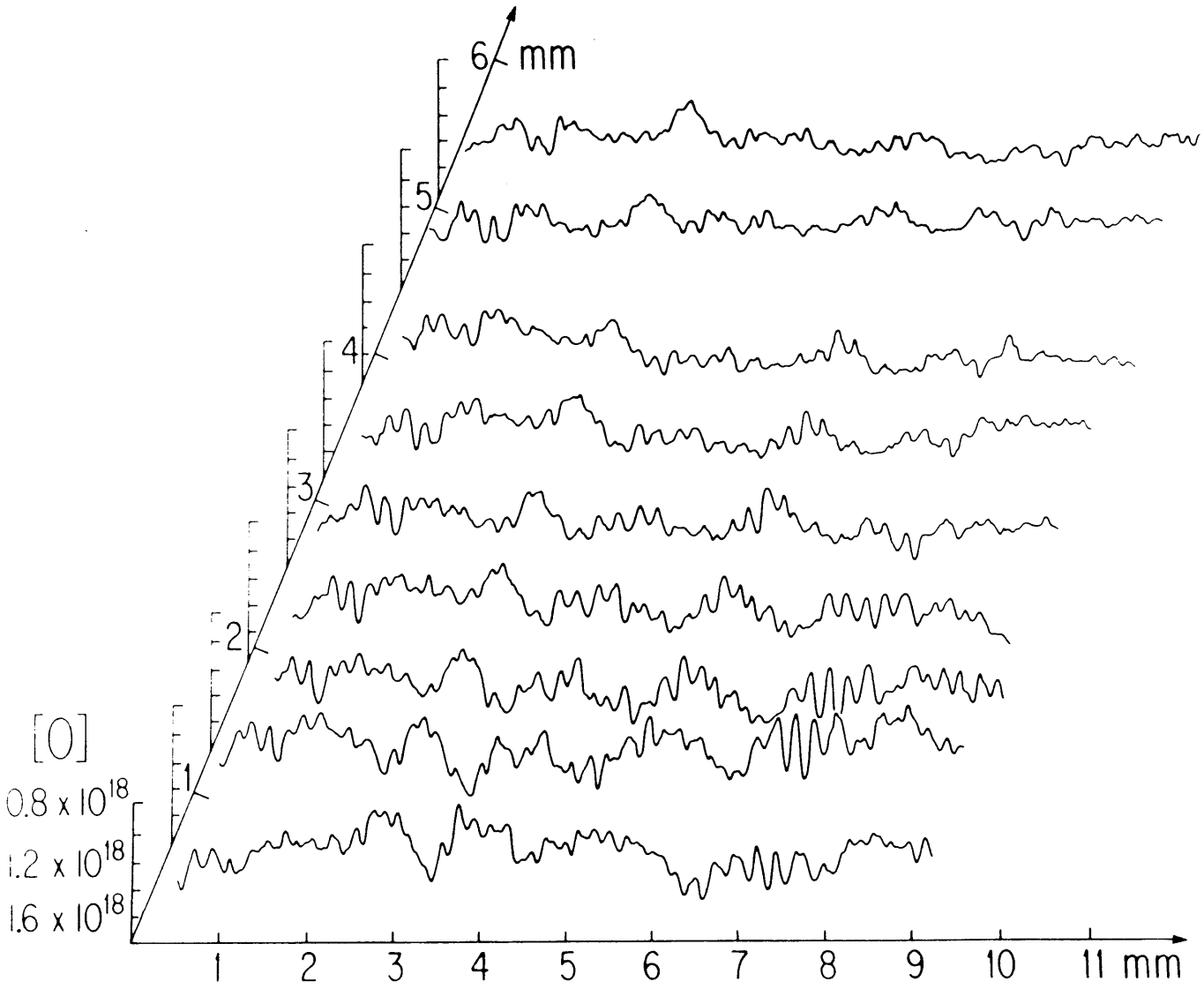

Fig. 4.5

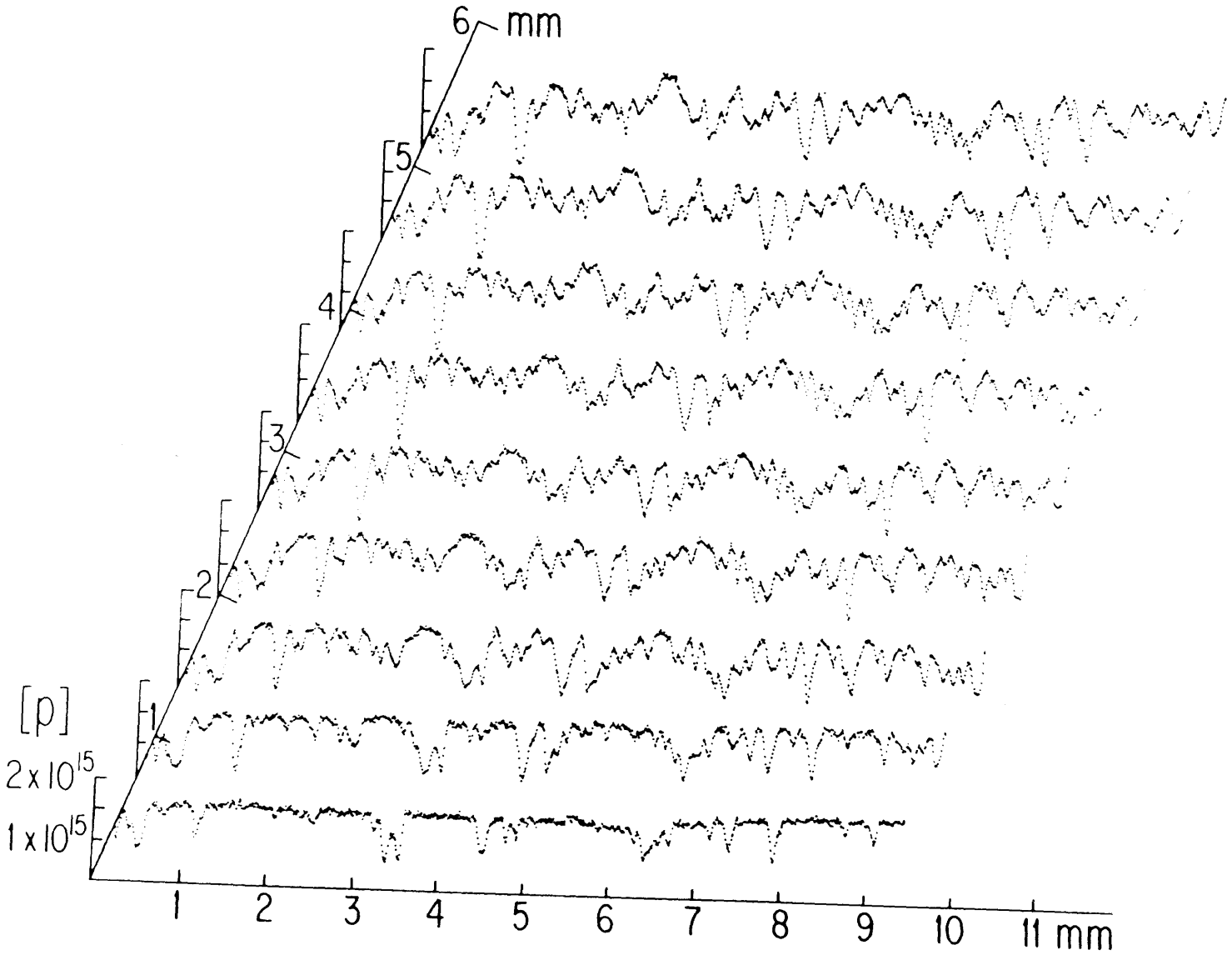

Fig. 4.6

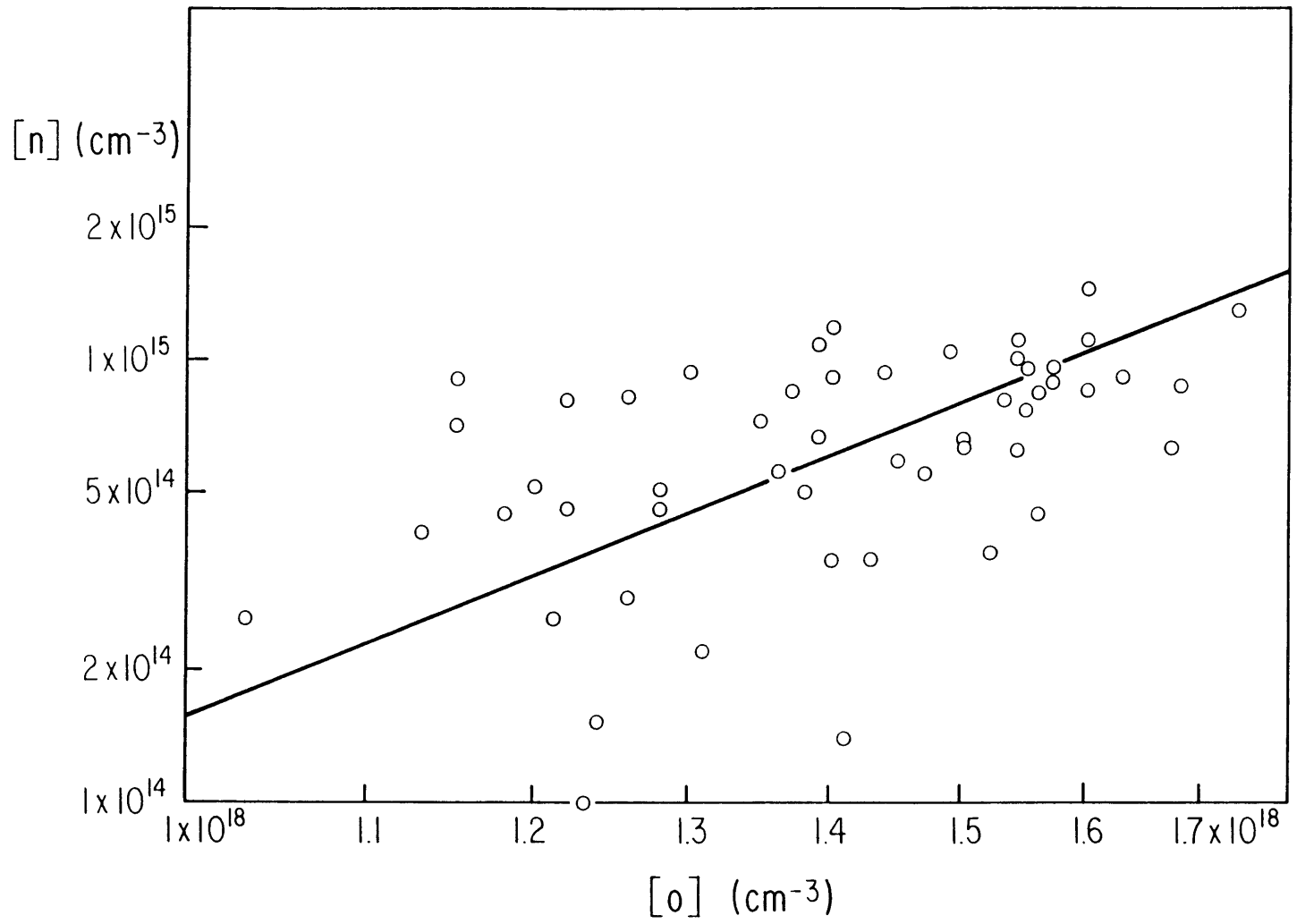
[n] (cm^{-3})
2 x 10^{15}
1 x 10^{15}
5 x 10^{14}
2 x 10^{14}
1 x 10^{14}
1 x 10^{18}
1.1
1.2
1.3
1.4
1.5
1.6
1.7 x 10^{18}
[o] (cm^{-3})

Fig. 4.7

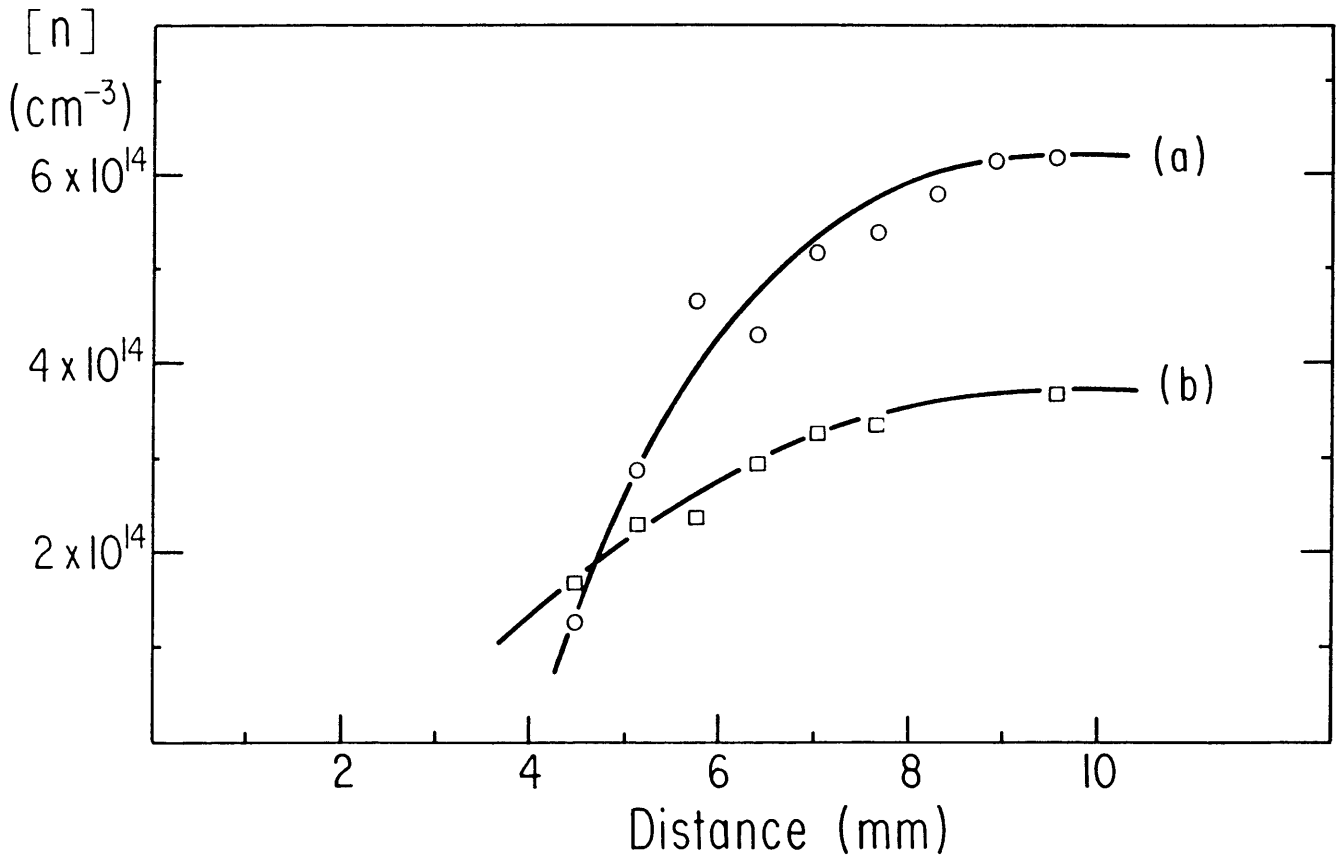

Fig. 4.8

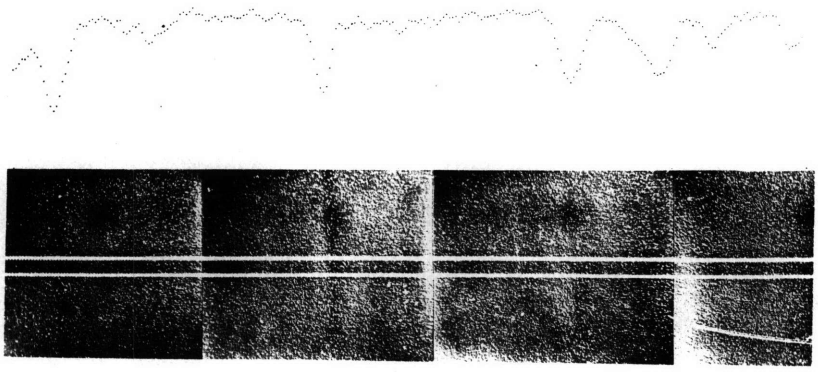

(a)

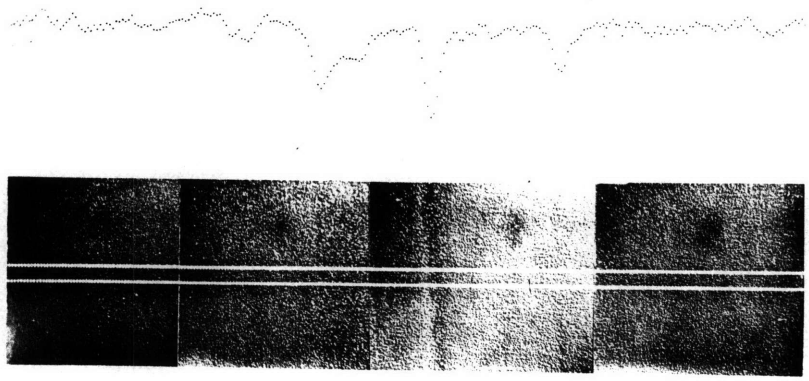

(b)

Fig. 4.9

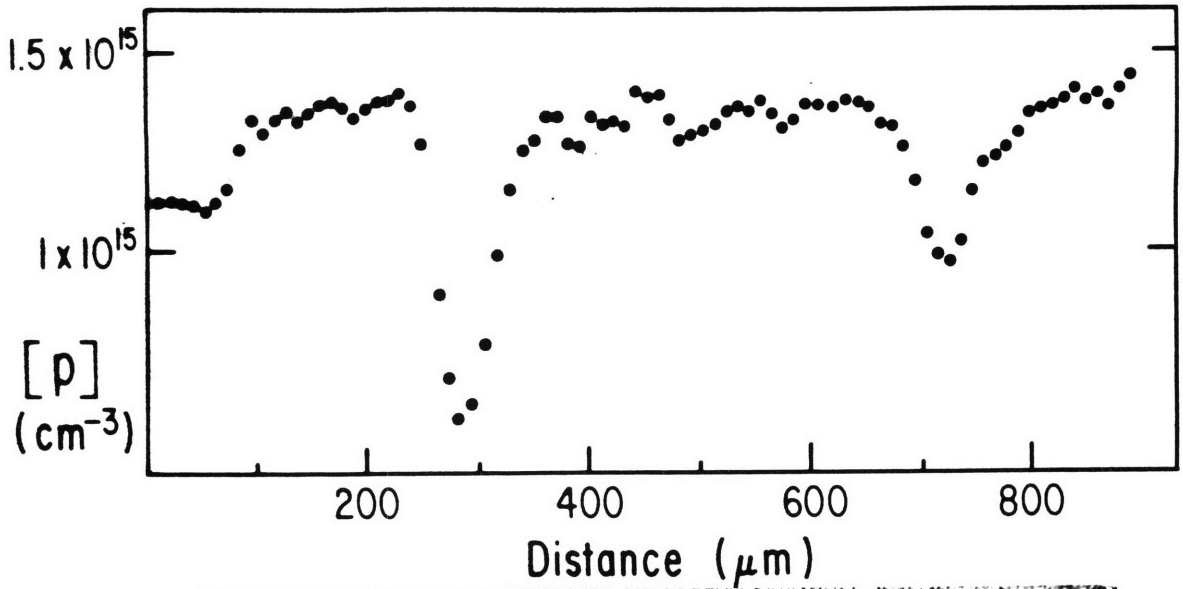

(a)

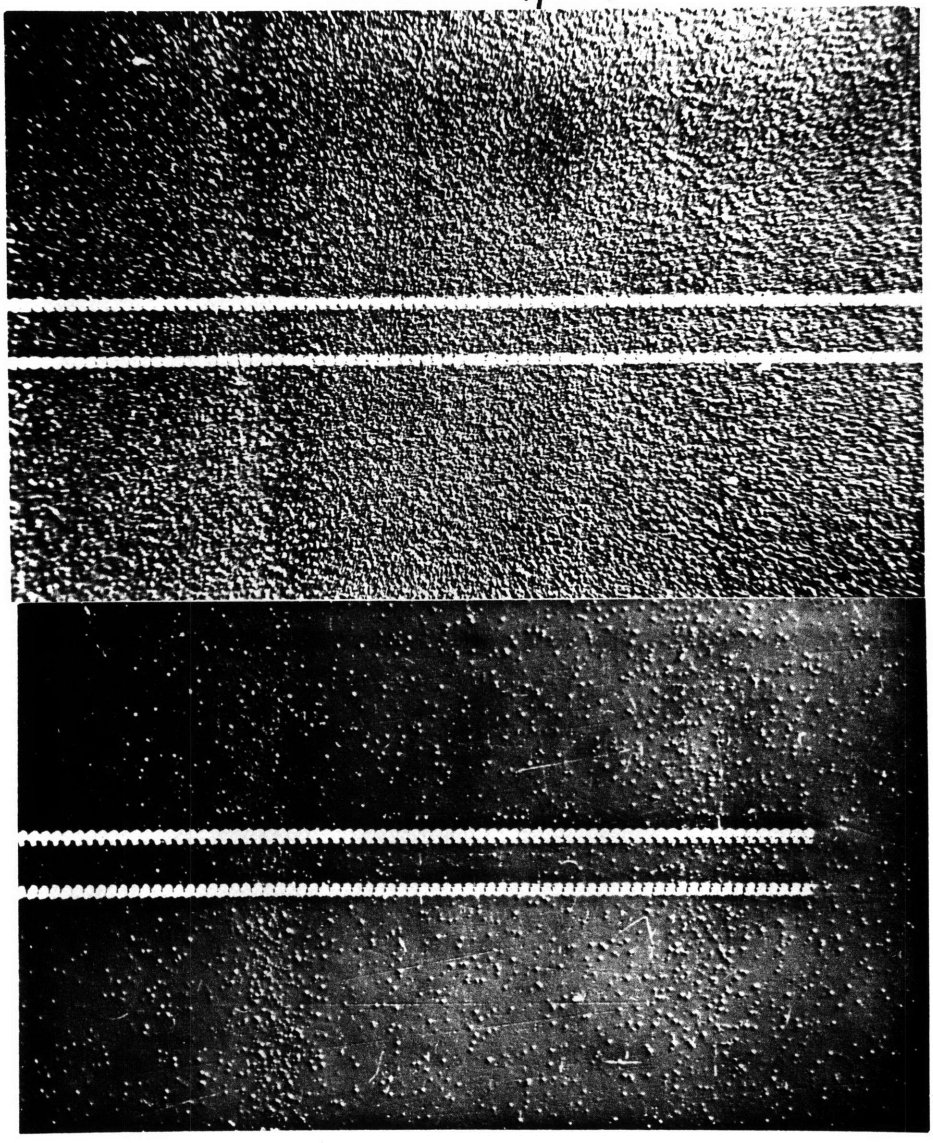

(b)

(c)

Fig. 4.10

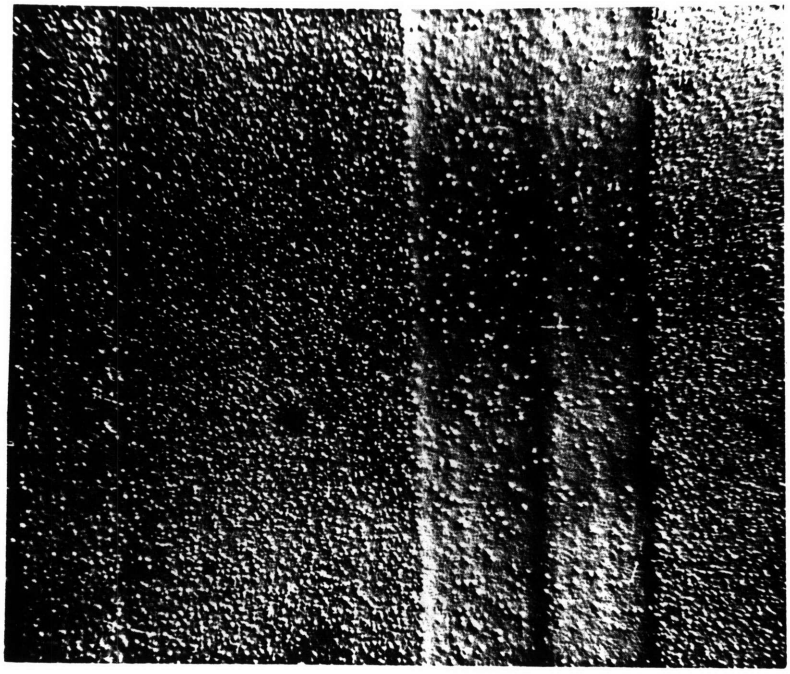

Fig. 4.11

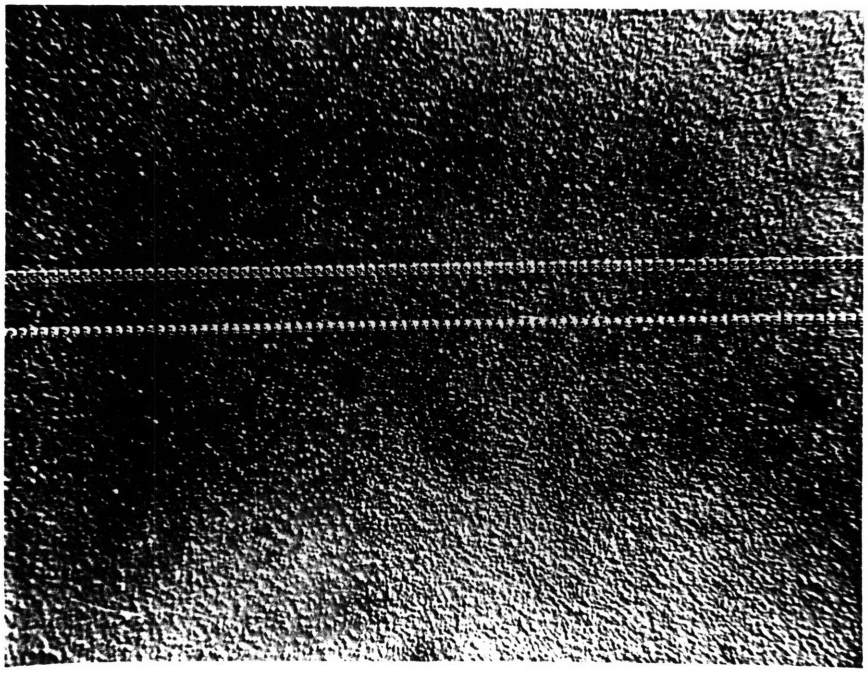

Fig. 4.12

V. DONOR ACTIVATION FOR DIFFERENT TYPES OF DOPANTS

V.1 Activation rates

In the previous section it was reported that the thermal donor activation rate differs in different areas of the same sample (B-doped). In this section the activation rate for oxygen-containing silicon crystals doped with different acceptors was investigated. All the samples investigated in this section were cut parallel to the growth direction from <111> Czochralski-grown dislocation-free B-doped, Ga-doped and In-doped silicon crystals; their regular diameter overall length was approximately 52 mm and the average carrier concentration was in the range 10^{15} - 10^{16} cm^{-3}. The average carbon concentration was about 1.4 x 10^{17} cm^{-3} for the B-doped crystal, 5.7 x 10^{16} cm^{-3} for the Ga-doped crystal and 5.4 x 10^{16} cm^{-3} for the In-doped crystal.

Free carrier concentration profiles were obtained at different distances from the periphery for the as-grown samples by spreading resistance measurements. The samples were then heat treated at 450°C for increasing lengths of time and the carrier concentration profiles along the same lines were measured. The average activated thermal donor concentrations at different distances from the periphery were obtained by averaging the spreading resistance scans and were plotted as a function of heat treatment time at 450°C; results for B-doped, Ga-doped and In-doped samples are shown respectively in Figs. 5.1, 5.2 and 5.3. It is seen that the activation rates are different at different distances from the periphery, partly due to the decrease in oxygen concentration toward the periphery. The activation rates differ for samples with different dopants, also partly due to differences in oxygen concentration between the samples.

The oxygen concentrations were measured for the samples in the standard way; the radial distribution was assumed to coincide with the distribution shown in Fig. 4.1, appropriately normalized for each sample. The

concentration of thermal donors activated by a heat treatment at 450°C for 8 hours is shown in Fig. 5.4 as a function of the interstitial oxygen concentration. It is seen that the activation rates are different for samples with different dopants and also that their dependence on the oxygen concentration is different. The thermal donor concentration for the B-doped sample is on the average proportional to the fourth power of the oxygen concentration, as shown by the straight line of slope 4 (Kaiser's law) (14). The same dependence on the oxygen concentration is found for the Ga-doped sample, but the amount of activated donors is much larger than for the B-doped sample, indicating participation of Ga in thermal donor activation.

In both the B-doped and the Ga-doped samples, data relative to points close to the periphery fall below the solid line, indicating the presence of a factor which does not depend on oxygen. This can also be seen in Figs. 5.1 and 5.2, where the thermal donor concentration for points close to the periphery saturates with heat treatment time. It can be noticed that the single point in the upper part of Fig. 5.4, relative to the center of another B-doped crystal, falls above the solid line drawn for the B-doped sample, indicating enhanced activation. The activated thermal donor concentration for the In-doped sample presents a different dependence on the oxygen concentration, as indicated by the solid line of slope 2.1. It is important to notice that the data relative to points close to the periphery fall on the solid line, indicating a proportionality between activated donors and oxygen and the absence of a factor hindering donor activation near the periphery, as opposed to what was found for Ga-doped and B-doped samples. This fact is also evident from the lack of

saturation in the curve relative to donors activated close to the periphery as a function of heat treatment time observed in Fig. 5.3.

V.2 Microdefect distribution

The microdefect distribution was investigated for B-, Ga- and In-doped samples by etching the surfaces with the same etchant discussed in Section IV. Results relative to B-doped samples were already reported in Section IV. A microphotograph of the etched surface of a Ga-doped sample heat treated at 450°C for 11 hours is shown in Fig. 5.5b. The spreading resistance trace visible was taken at 6 mm from the edge and the corresponding carrier concentration profile is shown in Fig. 5.5a. It is seen that defects have a lower density and slightly larger size in areas with larger activation. This is quite similar to what was observed in B-doped crystals, although differences between activated and non-activated areas are not as large. The sample was then heat treated at 650°C for 4 hours and etched with Sirtl etch; a microphotograph of the same area of Fig. 5.5b is shown in Fig. 5.5c. It is seen that an almost complete homogenization of the microdefect distribution has taken place, and some A-type defects appear in all areas. After a heat treatment at 450°C for another 4 hours, the defect density decreased in all areas (Fig. 5.6), indicating that no effect hindering donor activation due to defects still exists.

Quite different results were obtained for In-doped silicon. A microphotograph of the etched surface of an In-doped silicon crystal heat treated at 450°C for 26 hours at about 1 cm from the periphery is shown in Fig. 5.7. It is seen that the density of B-type defects is orders of magnitude lower than for B-doped and Ga-doped samples; a comparable density of A-type defects is visible in the highly activated areas. After

a heat treatment at 650°C for 4 hours, an etched surface presents a very homogeneous pattern of A-type defects (Fig. 5.8); the same pattern is present toward the center and the periphery of the crystal. These results indicate the absence of any effect due to defects hindering donor activation in In-doped silicon. This is consistent with results reported earlier in this section (Fig. 5.4).

V.3 Correlation between oxygen and Ga striations

A close comparison of the free carrier microprofiles before and after heat treatment at 450°C allows to draw some qualitative conclusions about the relationship between dopant microdistribution and oxygen microdistribution. In fact in the as-grown crystal the free carrier microprofile essentially coincides with the dopant microdistribution. After heat treatment at 450°C compensation by thermal donors occurs; in the absence of large concentrations of B-defects the thermal donor microdistribution bears a close relationship to the oxygen microdistribution.

It has been reported (44) that the maxima in B-dopant concentration correspond to minima in oxygen concentration for crystals grown under conditions of forced convection. This was attributed to the difference in the segregation coefficient (44), which is larger than one for oxygen (k_o = 1.25) and smaller than one for B (k = 0.8). The assumption was made that the mechanism of incorporation into the solid is microscopic growth rate controlled for both types of impurity under conditions of forced convection. The experimental evidence presented in ref. (44) is not conclusive: in fact, the B striations are barely detectable, due to the segregation coefficient close to unity.

It is a better approach to compare the Ga dopant microdistribution with the thermal donor microdistribution; in fact, Ga has a segrega-

tion coefficient much smaller than unity (k_o = .008) (68) and therefore the Ga striations have a large enough amplitude to make them unambiguously detectable.

The Ga dopant microprofile was measured along the axial direction on an as-grown commercial Ga-doped silicon crystal using the spreading resistance technique with a 5 μm sampling interval. A Ga microprofile taken at 11 mm from the periphery of the crystal is shown in Fig. 5.9a; the Ga striations can be clearly observed.

The sample was then heat-treated at 450°C for 2 hours and a spreading resistance scan was taken along the same line; the corresponding carrier concentration microprofile is shown in Fig. 5.9b. It is seen that thermal donors have been activated in numerous locations. Due to the relatively large distance from the periphery (11 mm), the effects due to B-defects are negligible and there is an overall correspondence between thermal donor and oxygen microprofiles. It is seen that the oxygen striations have a pattern very different from the Ga striations: they are much more irregular and their width is larger. In particular it is to be noticed that at 500 μm a large compensation occurs, in correspondence of a marked oxygen maximum (Fig. 5.9b). The oxygen maximum occurs at the same location as a Ga maximum (Fig. 5.9a). In other locations (for example, around 1200 μm and 1600 μm) the oxygen maxima do not coincide with Ga maxima and in some instances coincide with Ga minima (around 1200 μm). In most locations the oxygen striations have a width larger than the Ga striations; the oxygen maxima also appear to occur in correspondence to a large amplitude of the Ga striations.

These facts allow to reach the conclusion that the mechanisms of incorporation into the crystal of the oxygen impurity and of the Ga

impurity are quite different. For oxygen the dominating mechanism is turbulence convection, while for Ga microsegregation effects are predominant. This is not surprising, in light of the fact that this crystal was not grown under forced convection, as opposed to the crystal considered in ref. (44), where both types of impurities were microscopic growth rate controlled.

Large concentrations of oxygen are incorporated into the melt during conditions of thermal instability: hence the correspondence between oxygen maxima and large amplitude of Ga striations. Conditions of thermal instability generally have a period longer than the period of rotation: hence the larger width of the oxygen striations than of the Ga striations.

It can be concluded that a model for the incorporation of oxygen into the crystal under standard growth conditions cannot be based on a standard microsegregation analysis. Turbulence convection as well as the origin of oxygen from the SiO_2 crucible have to be taken into account.

Figure Captions

Fig. 5.1 Thermal donor concentration [n] as a function of heat treatment time at 450°C for a B-doped silicon sample with average oxygen concentration 1.44×10^{18} cm^{-3} at different distances from the periphery of the crystal.

- ○ 4 mm from the periphery
- ▲ 5 mm from the periphery
- △ 6 mm from the periphery

Fig. 5.2 Thermal donor concentration [n] as a function of heat treatment time at 450°C for a Ga-doped silicon sample with average oxygen concentration 1.48×10^{18} cm^{-3} at different distances from the periphery of the crystal.

- ● 2 mm from the periphery
- ▲ 4 mm from the periphery
- △ 6 mm from the periphery
- □ 8 mm from the periphery
- ○ 1 cm from the periphery

Fig. 5.3 Thermal donor concentration [n] as a function of heat treatment time at 450°C for an In-doped silicon sample with average oxygen concentration 2.13×10^{18} cm^{-3} at different distances from the periphery of the crystal. Symbols are the same as in Fig. 5.2.

Fig. 5.4 Thermal donor concentration [n] as a function of the interstitial oxygen concentration at different distances from the periphery of the crystal.

- ○ B-doped
- □ Ga-doped
- ● In-doped
- △ B-doped center of crystal

Fig. 5.5 (a) Carrier concentration profile taken at 6 mm from the periphery of a Ga-doped Si crystal heat treated at 450°C for 11 hours.

(b) Microphotograph of the surface of the same sample as in (a) etched with Sirtl etch; the spreading resistance trace corresponds to the carrier concentration profile in (a).

(c) Microphotograph of the surface of the same sample heat treated at 450°C for 11 hours and at 650°C for 4 hours etched with Sirtl etch; same location as in (b).

Fig. 5.6 Microphotograph of the surface of a Ga-doped silicon sample heat treated at 450°C for 11 hours, at 650°C for 4 hours and at 450°C for 4 hours etched with Sirtl etch.

Fig. 5.7 Microphotograph of the surface of an In-doped Si sample heat treated at 450°C for 26 hours at about 1 cm from the edge etched with Sirtl etch.

Fig. 5.8 Microphotograph of the surface of an In-doped Si sample heat treated at 450°C for 26 hours and at 650°C for 4 hours at about 1 cm from the edge etched with Sirtl etch.

Fig. 5.9 (a) Carrier concentration profile taken at 11 mm from the periphery of an as-grown Ga-doped Si crystal using a 5 μm probe sampling interval.
(b) Carrier concentration profile taken along the same location as in (a) on the same sample heat-treated at 450°C for 2 hours.

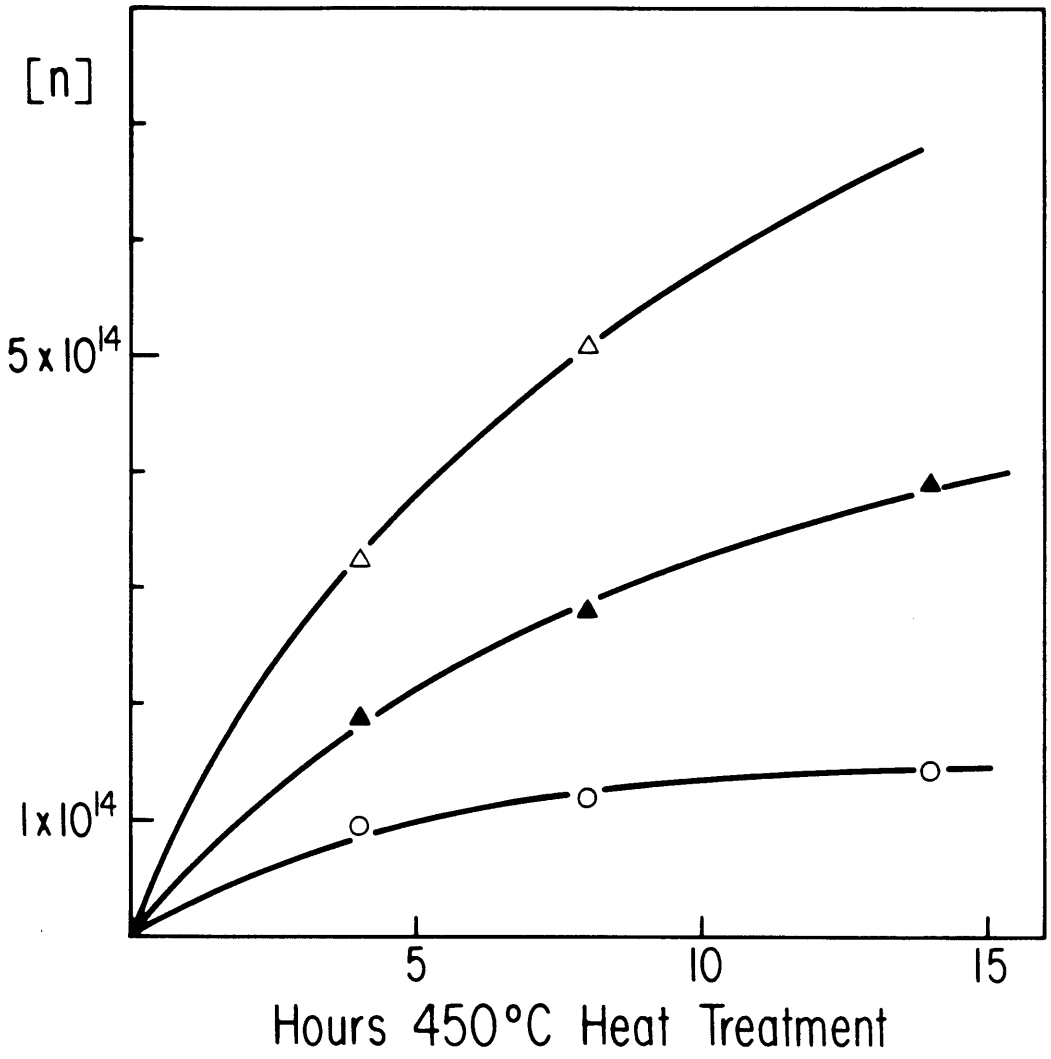

Fig. 5.1

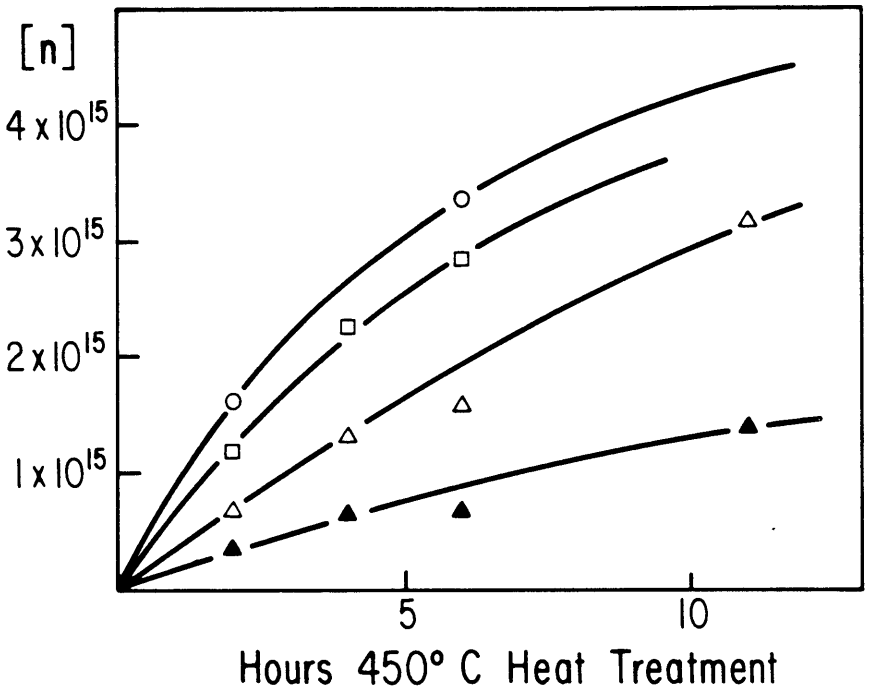
[n]
4 x 10^15
3 x 10^15
2 x 10^15
1 x 10^15
5
10
Hours 450° C Heat Treatment

Fig. 5.2

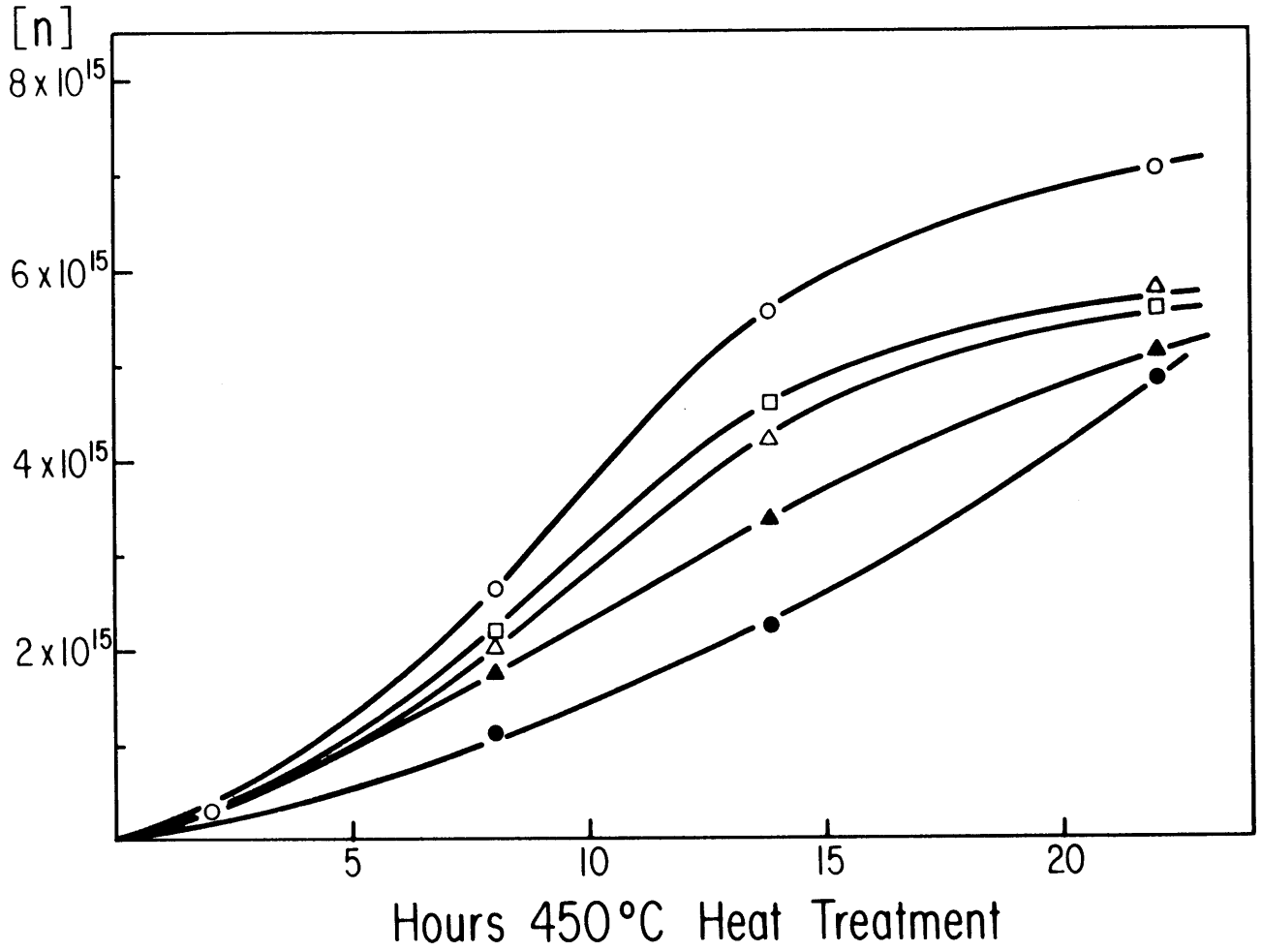
[n]
8 x 10^15
6 x 10^15
4 x 10^15
2 x 10^15
5
10
15
20
Hours 450°C Heat Treatment

Fig. 5.3

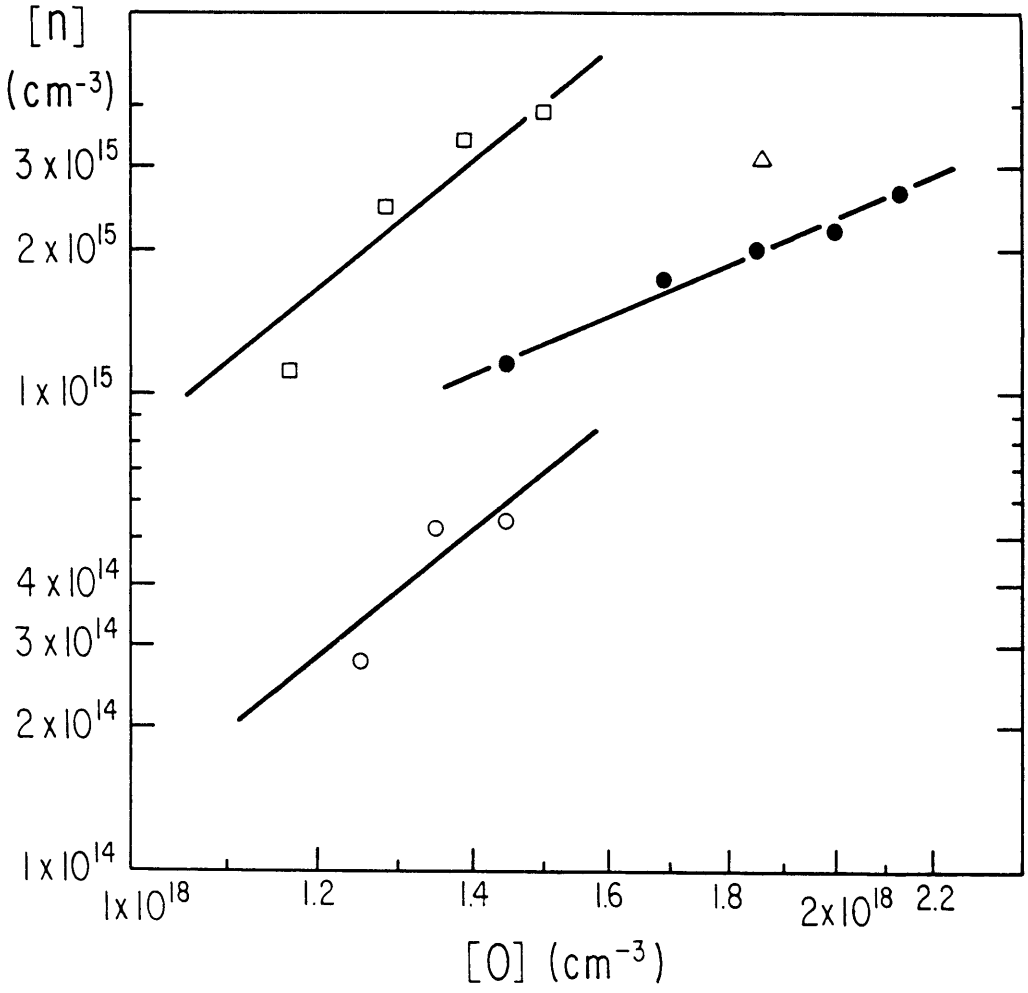
[n]
(cm⁻³)
3 x 10¹⁵
2 x 10¹⁵
1 x 10¹⁵
4 x 10¹⁴
3 x 10¹⁴
2 x 10¹⁴
1 x 10¹⁴
1x10¹⁸
1.2
1.4
1.6
1.8
2x10¹⁸
2.2
[O] (cm⁻³)

Fig. 5.4

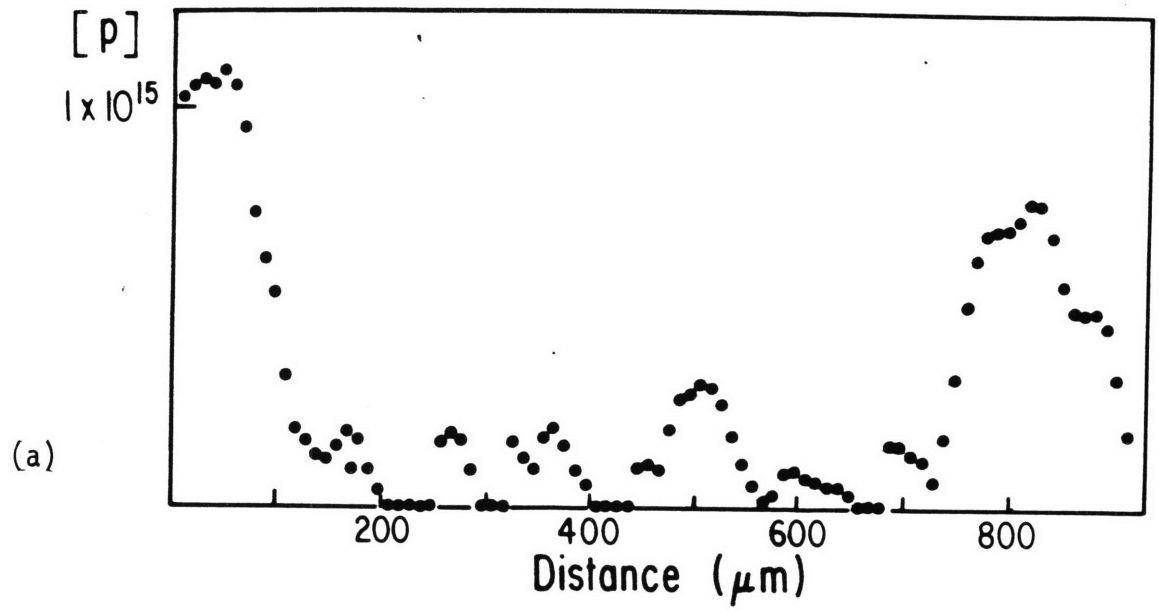

(a)

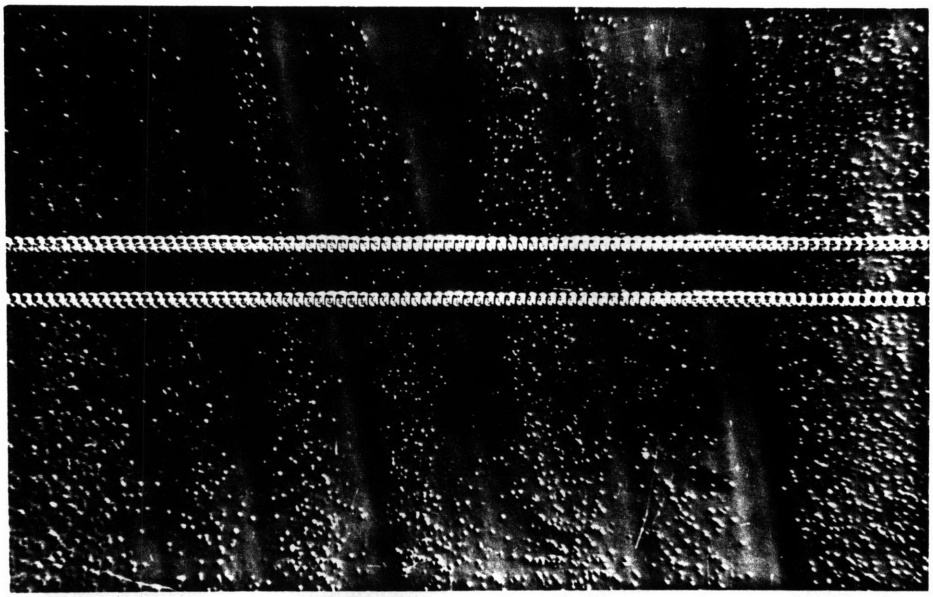

(b)

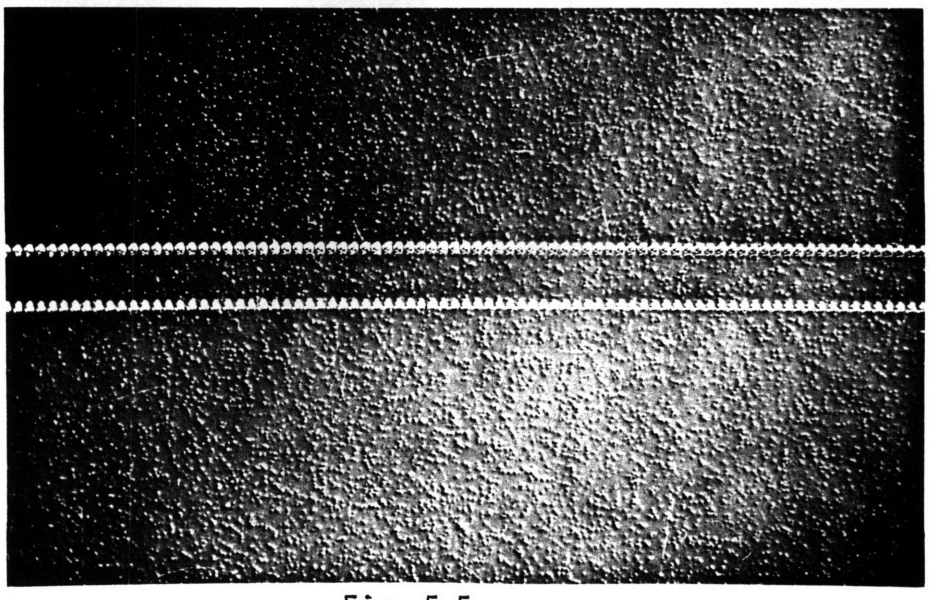

(c)

Fig. 5.5

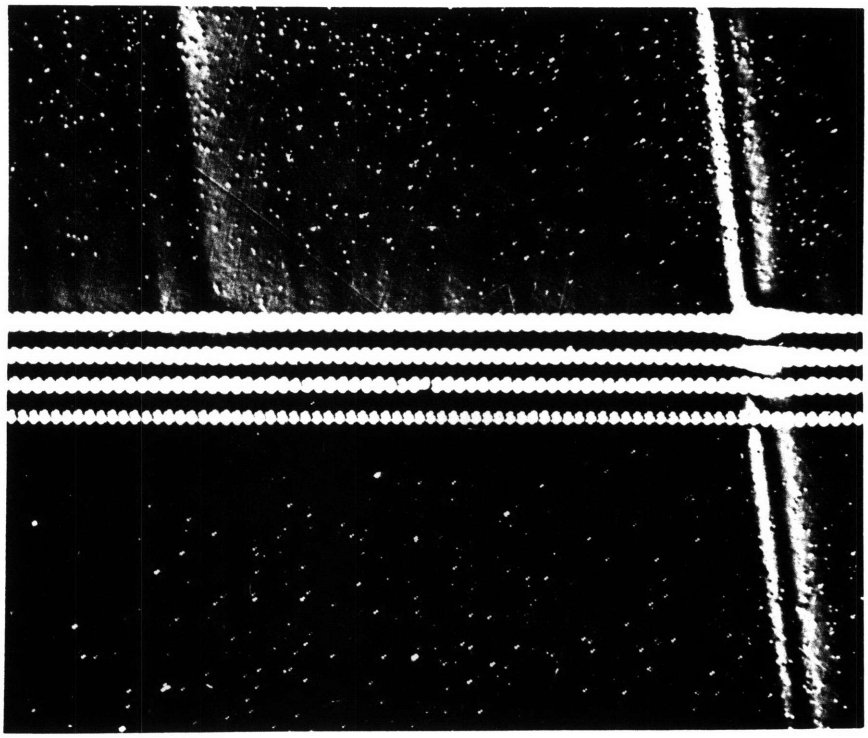

Fig. 5.6

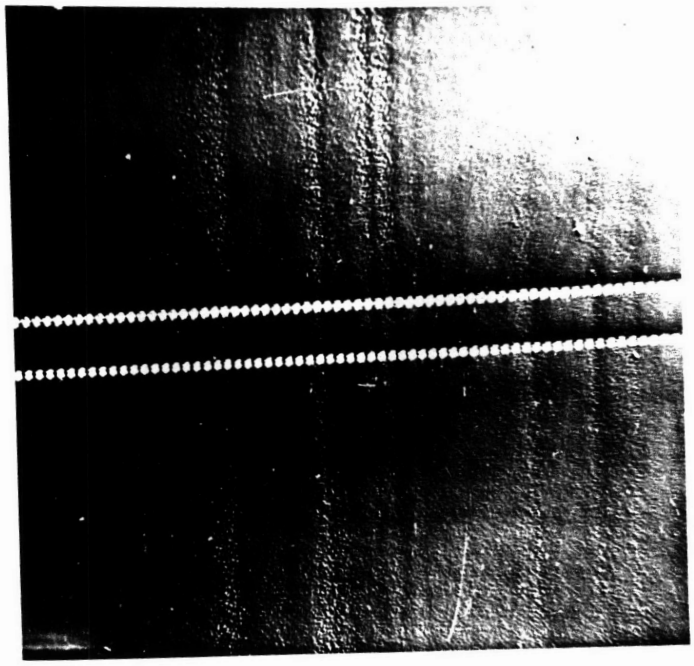

Fig. 5.7

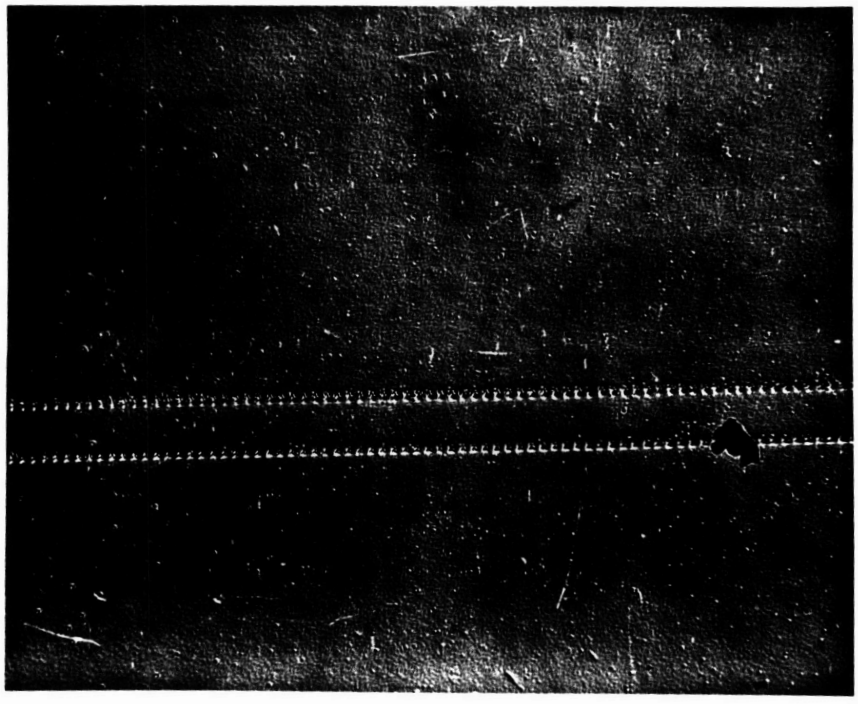

Fig. 5.8

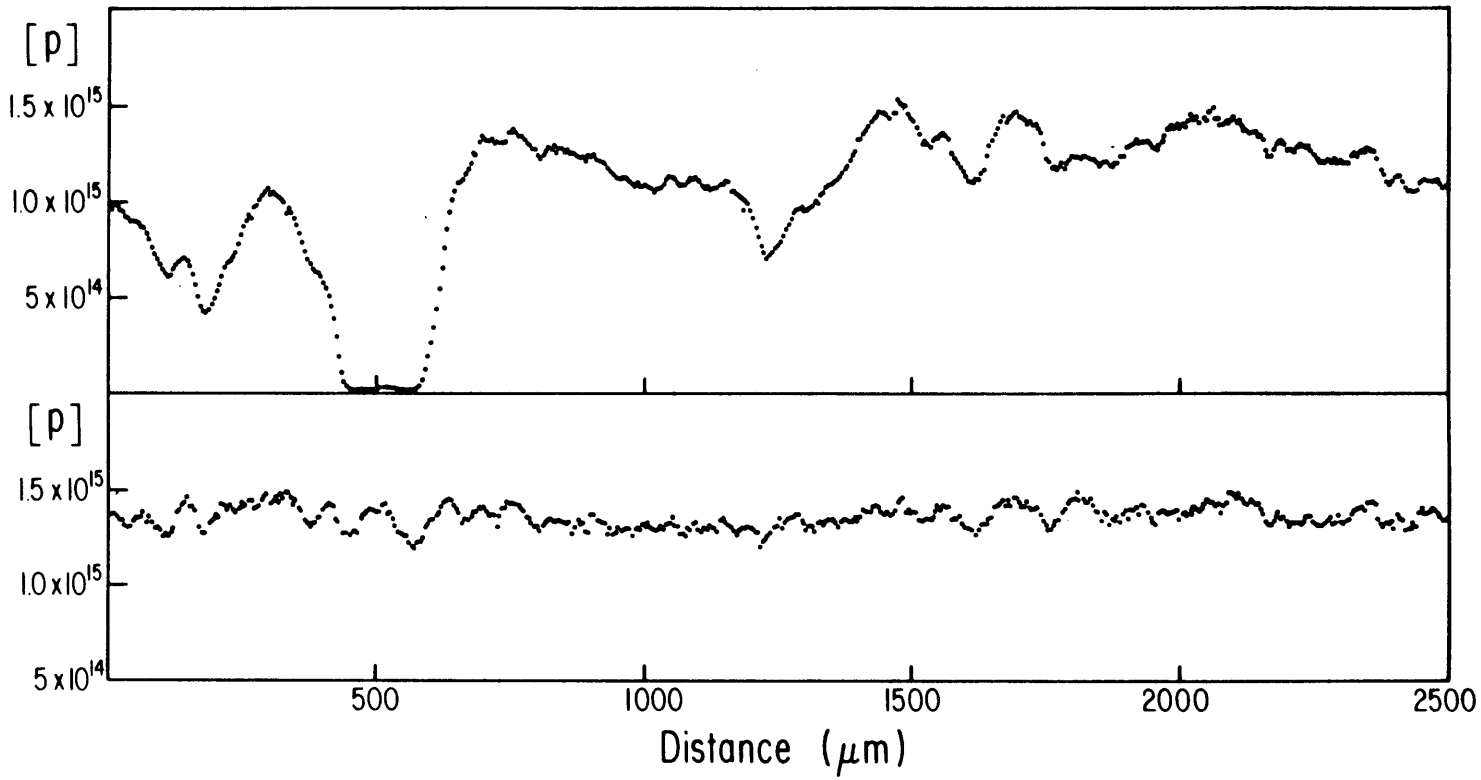
[p]
1.5 x 10^15
1.0 x 10^15
5 x 10^14
[p]
1.5 x 10^15
1.0 x 10^15
5 x 10^14
500
1000
1500
2000
2500
Distance (μm)

Fig. 5.9

VI. DISCUSSION AND INTERPRETATION

VI.1 Vacancy-oxygen complexing model

It is apparent from the results presented in Sections IV and V that the concentration of oxygen is not necessarily the controlling factor in the activation of thermal donors. The presence of another species which in some instances can control thermal donor activation has been detected with the aid of microscale analysis. These results, at least qualitatively, are in good agreement with the model proposed by Helmreich and Sirtl (22) which postulates the interaction of interstitial oxygen with silicon vacancies and acceptor atoms and was already described in Section II. This model implies that the activation of oxygen donors does not depend only on oxygen concentration, but requires the presence of vacancies. However, since the oxygen concentration fluctuates significantly in silicon crystals, this implication could not be tested without knowledge of the actual concentration of oxygen on a microscale.

The present results show that the concentration of activated donors may not be proportional to the oxygen concentration, and, in fact, is strongly dependent on the microdefect distribution. In fact, B-type defects, which exhibit high densities in some regions close to the periphery of the crystal, act essentially as vacancy getters; accordingly, extensive activation of donors does not take place in these regions of the crystal upon the first heat treatment at 450°C. On the other hand, A-type defects may not be active vacancy getters; thus, in areas where A-type defects are predominant, vacancies are available for thermal donor formation upon the first heat treatment at 450°C, according to eqs. 2.6, 2.7 and 2.8. This result is consistent with the fact that A-defects are formed by the agglomeration of Si self-interstitials (69) and involve no vacancies; the nature of the B-defects is still under investigation.

Prolonged heat treatment at 650°C causes a faster diffusion of vacancies

where they are available (regions with A-type defects), so that the neutral three vacancies - oxygen complexes (eq. 2.9) become predominant, causing elimination of donors in the regions previously activated. On the other hand, upon heat treatment at 650°C, B-type defects tend to become A-type, making vacancies available for donor formation. So, upon further heat treatment at 450°C, oxygen atoms can more readily find vacancies for complexing in regions which previously were not activated. In contrast, in regions previously activated, donor activation still takes place, but at a reduced level because some of the oxygen and vacancies are now tied up in neutral three vacancies - oxygen complexes. Further heat treatments at 450°C increase the vacancy-oxygen donor complexes, and further heat treatments at 650°C cause further depletion of "free" vacancies and oxygen and further formation of A-defects.

According to the authors of the present model, in the reaction described by eq. 2.9, the bonding of the donor complex is altered to an electrically inert configuration; this process can be viewed as a low energy phase transition probably due to elastic recovery processes and, thus, correlated to vacancy supported stability of substitutional oxygen. The inert complexes of eq. 2.9 may serve as nucleation centers for SiO_2 precipitates (67) which occur for prolonged high temperature heat treatments; they could not be detected in the present study, since no absorption band at 1230 cm^{-1} was observed, due to the heat treatments low in temperature and short in time.

VI.2 Influence of other impurities

Vacancies are necessary to initiate the process of donor formation, since the reaction described by eq. 2.6 can only take place with the participation of a vacancy. In the following steps, described by eq. 2.7, 2.8 and 2.9, acceptor atoms can take the place of vacancies. The results

reported in Section V can be interpreted in light of this assumption. The difference in the magnitude of the activation rate between B-doped and Ga-doped samples shown in Fig. 5.4 can be explained by a larger participation of Ga atoms in the formation of donor complexes. This result is consistent with the observation of a complex between gallium and oxygen, reported by Hrostowski and Kaiser (25). Toward the periphery of the crystal, the activation is lower both for B-doped and Ga-doped samples, indicating a lower availability of vacancies to start the process of donor activation; this is consistent with the fact that B-type defects were observed near the periphery of both B-doped and Ga-doped crystals. Near the center of the crystal, the larger availability of vacancies enhances donor activation, as shown by the point in the upper part of Fig. 5.4 relative to the center of a B-doped crystal. For the In-doped crystal, no decrease in activation toward the periphery is observed: the activated donor concentration is to a very good approximation proportional to the oxygen concentration, as indicated by the solid line. Oxygen is the controlling factor in donor activation, indicating that vacancies are plentiful and available everywhere to start donor activation. This is consistent with the fact that very low densities of B-type defects are present at all distances from the periphery of In-doped crystals.

An interpretation of the influence of various impurities on thermal donor activation can be given by considering their influence on the lattice parameter of silicon. The tetrahedral radii of the elements of interest are, after Pauling (70):

Element	Si	C	B	Ga	In	O
r_{tet} (Å)	1.17	0.77	0.88	1.26	1.44	0.66

Oxygen is the only one of these elements which is considered to be interstitial in as-grown silicon; therefore, oxygen introduces a strain in the silicon lattice which increases its lattice parameter (17). As a consequence of the induced strain, higher concentrations of vacancies can be expected in an oxygen-containing silicon crystal than in a pure silicon crystal. Besides, it is conceivable that the concentration of vacancies is lower toward the periphery, due to the lower oxygen concentration.

Carbon has a radius smaller than silicon and occupies substitutional sites; therefore, it tends to reduce the lattice parameter (29). When present in high enough concentration in an oxygen-containing silicon crystal, it compensates the lattice strain introduced by oxygen and, therefore, causes a reduction in the vacancy concentration. This accounts for the reduced thermal donor activation observed in high carbon content crystals by Bean and Newman (21). It should also be pointed out that carbon leads to the formation of B-defects (69). In the present study the density of B-defects was higher for the B-doped sample ($C_{ave} \simeq 1.4 \times 10^{17}$ cm^{-3}) than for the Ga-doped sample ($C_{ave} \simeq 5.7 \times 10^{16}$ cm^{-3}) and even more than for the In-doped sample ($C_{ave} \simeq 5.4 \times 10^{16}$ cm^{-3}). Although microprofiling of carbon is not possible at present, it is possible that the high density of B-defects and lack of thermal donor activation in certain regions are associated with high carbon concentration.

Of the acceptor dopants, boron (r_{tet} = 0.88 Å) tends to reduce the lattice parameter while gallium (r_{tet} = 1.26 Å) and indium (r_{tet} = 1.44 Å) tend to increase it. The effect of boron and gallium is negligible with respect to the effect of oxygen, since their concentration in the samples investigated (~ 10^{15} - 10^{16} cm^{-3}) is a lot lower than the oxygen concen-

tration ($\sim 10^{18}$ cm^{-3}). On the other hand, the concentration of the indium impurity is about three orders of magnitude larger than the boron and gallium concentration. In fact, indium forms a deep level in silicon ($E_a \cong 0.16$ eV) and only some atoms are ionized at room temperature: to achieve the carrier concentration of about 1.8×10^{16} cm^{-3} measured in the sample investigated, a much larger impurity concentration is needed. The large mismatch between the radii of indium (1.44 Å) and silicon (1.17 Å) combined with the large indium concentration ($\sim 10^{19}$ cm^{-3}) causes an increase in the vacancy concentration in all areas of the crystal.

VI.3 Concentration and diffusivities of vacancies, oxygen and other impurities

In support of the model presented above, it is important to note that silicon crystals have concentrations of vacancies in the right order of magnitude to explain donor formation. In fact, the concentration of vacancies is given by (66)

$$N_V = N \exp\left(-\frac{\Delta G_V}{kT}\right) = N \exp\left(\frac{\Delta S_V}{k}\right) \exp\left(-\frac{\Delta H_V}{kT}\right) \qquad (6.1)$$

where N is the number of atomic sites in silicon, ΔG_V is the free energy of formation for a vacancy, ΔS_V the entropy of formation, ΔH_V the enthalpy of formation, k Boltzmann constant and T the temperature. Using values given in the literature, the concentration of vacancies at the melting point of silicon is $N_V = 7.2 \times 10^{15}$ cm^{-3}. Assuming that the crystal is quenched to room temperature, this is also the concentration of vacancies frozen in at room temperature and can account for the formation of vacancy-oxygen donor complexes of the order of magnitude $\sim 10^{15}$ cm^{-3}. It should be noted that the figure given above refers to a pure silicon crystal; impurities introduce a lattice strain as already discussed, so

that substantially higher vacancy concentrations are to be expected. As a matter of fact, values of the vacancy concentration determined from experimental data are substantially higher than the figure calculated above (66).

The vacancy-oxygen complexing model discussed above requires also that the diffusivity of vacancies be large enough to allow them to come in contact with oxygen atoms. The diffusion coefficient of vacancies is given by (66):

$$D_V(T) = g\, a^2\, \nu \exp\left(-\frac{E_V^M}{kT}\right) \qquad (6.2)$$

where g is a geometrical factor, a the elementary jump distance, ν the apparent jump frequency, E_V^M the migration energy of a vacancy, k the Boltzmann constant and T the temperature. The diffusion length of vacancies is given by:

$$L_V = \sqrt{D_V \tau} \qquad (6.3)$$

where τ is the lifetime of vacancies. Assuming that the limiting factor for the lifetime of vacancies is the vacancy-oxygen complexing mechanism under consideration and using for the constants values reported in the literature, during a heat treatment at 450°C for 4 hours a vacancy travels 1 mm and during a heat treatment at 650°C for 4 hours a vacancy travels 1.8 mm. On the other hand, assuming another lifetime limiting mechanism and taking for the lifetime a value of 180 seconds, reported in the literature (71), a vacancy travels 110 μm during a heat treatment at 450°C

and 200 μm during a heat treatment at 650°C. Considering that the average distance between oxygen atoms for concentrations of the order of 10^{18} cm^{-3} is 100 Å, any of these vacancy travel distances is enough to allow formation of vacancy-oxygen complexes.

On the other hand, the diffusivity of oxygen (15-18) is not large enough to allow formation of the SiO_4 complexes, which have been proposed by Kaiser (14) to explain donor activation, during the first few hours of heat treatment at 450°C. An oxygen atom during a heat treatment at 450°C for 4 hours travels 16 Å, less than the average distance between oxygen atoms. But the formation of multi-oxygen complexes cannot be ruled out for long heat treatments at 450°C or heat treatments at 650°C.

The diffusivity of acceptor dopants (72) is lower than the diffusivity of oxygen, so that their movement in the silicon lattice upon heat treatment at 450°C is very limited. On the other hand, a high diffusivity is not so important to explain the participation of acceptors to thermal donor activation as it is to explain the formation of the SiO_4 complexes. In fact, only one acceptor atom is needed to form a donor complex in Helmreich's model (22), while four oxygen atoms are needed to form a donor complex in Kaiser's model (14).

VI.4 Multioxygen complexes

It is to be noticed that some experimental facts cannot be explained satisfactorily by the vacancy-oxygen complexing model. In particular, the activated donor concentration never exceeds one-fourth of the initial oxygen concentration; the presence of various donor energy levels, which vary with heat treatment time, indicate the presence of more than one type of donor of changing structure; and, in general, the kinetics are fairly well-explained by Kaiser's theory. The results reported in the present

work indicate that Kaiser's law is usually obeyed on the average, although local deviations revealed by the microscale analysis exist. It is important to point out that these deviations are relative to the initial stages of donor formation, consistent with the hypothesis that vacancies are necessary for the initial step of donor formation described by eq. 2.6. In contrast to this, Kaiser's theory is based on the kinetics of the donor activation process on a longer time scale, and the conditions relative to starting the process have been neglected. In fact, it can be shown that Helmreich's and Kaiser's models are not necessarily opposed, and, in fact, they can be considered complementary.

Already in 1961 Suchet (33) suggested that vacancies are necessary for the formation of the SiO_4 complexes postulated by Kaiser. This suggestion acquires new significance in light of the present results.

In the first step of thermal donor activation, an interstitial oxygen combines with a silicon vacancy to become substitutional, according to eq. 2.6. In this position the oxygen atom has formed four covalent bonds with the four neighboring silicon atoms and has two extra electrons. It can be stabilized by complexing with another vacancy or an acceptor atom according to eq. 2.7 and then be ionized as a donor according to eq. 2.8. It is also possible that another oxygen atom could play the role of the stabilizing acceptor, giving rise to a donor center involving two oxygen atoms. The reaction then continues much in the same way as described by Kaiser (14), with formation of donor complexes composed of an increasing number of oxygen donors. After long enough heat treatment times, the balance of the reaction moves toward complexes containing four oxygen atoms, which account for the reaction kinetics described by Kaiser. The

ionization energy decreases for donors containing more oxygen atoms, as can be deduced from its observed decrease with heat treatment time (37 - 39). Complexes containing more than four oxygen atoms are neutral and account for donor annihilation at 650°C. The type of complex predominant depends on a wide range of conditions relative both to the crystal and to the heat treatment. Therefore, under some conditions donors can be generated also around 700°C (40-43). In conclusion, the present microscale analysis has revealed the essential role of vacancies in the initial stage of thermal donor activation. It was shown that the formation of single or multi-oxygen donor complexes in silicon requires the participation of vacancies.

VII. OXYGEN-DOPED MULTIJUNCTION SOLAR CELL STRUCTURE

VII.1 Background

Of all semiconductor devices actively investigated to date, photovoltaic solar cells are of great interest in the light of their prospective contribution to the solution of the energy crisis. Silicon is by far the most extensively used material among the various semiconductors which can be employed in the fabrication of photovoltaics. Various device structures are employed in the fabrication of photovoltaics.

The conventional solar cell structure consists of a p-n junction formed by diffusing a dopant onto a substrate of the opposite conductivity type; the junction is usually a few fractions of a micron below the surface and sunlight is incident perpendicular to the junction. Carriers generated within one diffusion length of the junction are collected and contribute to the current. The total collection efficiency is defined as the ratio of collected carriers to generated carriers (73) and it is proportional to the short circuit current I_{sc}. The total conversion efficiency η is defined as the ratio of the maximum output usable electrical power P_{out} to the incident sunlight power P_{sun}:

$$\eta = \frac{P_{out}}{P_{sun}} \tag{7.1}$$

The maximum output electrical power is given by:

$$P_{out} = V_{oc}\ I_{sc}\ (FF) \tag{7.2}$$

where V_{oc} is the open circuit voltage and FF is a factor of proportionality called fill factor.

The collection efficiency depends on the diffusion length; in the case of the conventional solar cell structure, carriers generated farther than one diffusion length from the junction cannot be collected and do not contribute to the current. Short wavelength photons are absorbed in the top layer close to the junction and generate carriers which are collected, whereas long wavelength photons are absorbed well in the bulk of the material and generate carriers which may not be collected. The collection efficiency of this structure decreases at long wavelengths.

A structure with an improved collection efficiency at long wavelengths is the vertical multijunction (74). It consists of a series of p-n junctions closely spaced, perpendicular to the top surface and extending throughout the thickness of the device. Sunlight is incident parallel to the junctions and both long wavelength and short wavelength photons generate carriers at similar distances from the junctions. If the diffusion length of the generated carriers is longer than the spacing between the junctions, carriers can be collected.

Surface recombination of carriers is one of the effects which causes degradation of the collection efficiency, particularly in vertical multijunctions. In this structure, junctions extend all the way to the surface, and the high surface recombination velocity causes carriers to recombine before they can be collected. The adverse effect of surface recombination at the back surface of both a conventional and a vertical multijunction structure can be minimized by diffusing a highly doped layer of the same conductivity type as the bulk; this layer creates a field which keeps carriers away from the back surface preventing them from recombining. At the same time, this additional field adds up to the junc-

tion potential to increase the open circuit voltage. Such a structure is called the back surface field (BSF) solar cell (75).

Many ways of fabricating vertical multijunction solar cells have been proposed. They usually involve fairly complicated and expensive processing procedures involving a series of masking and etching steps. In the present work a very simple and inexpensive procedure to fabricate a vertical multijunction structure (76) using low temperature heat treatment of oxygen-containing silicon was investigated.

VII.2 Heat-treated multijunction structure

As reported in Section IV, oxygen is non-uniformly distributed in silicon and upon heat treatment at 450°C it generates a non-uniform distribution of thermal donors. In p-type silicon, the thermal donor fluctuations lead to compensation of the p-type matrix and, after an appropriate heat treatment time, to overcompensation (inversion of the conductivity type) at the thermal donor concentration maxima (44,76). An alternate p-n junction structure results, where the spacing between the junctions depends on the width of the thermal donor striations. As it is seen in Fig. 4.6, in commercial Czochralski silicon, the striation pattern is quite irregular and fairly largely spaced inhomogeneities lead to a large junction spacing.

In order to utilize the multiple junctions for device applications, thin n^+ and p^+ layers are diffused onto the top and bottom of the p-type longitudinal slices before activating the vertical junctions by the 450°C heat treatment. Contacts to the top and bottom of the silicon slice are then made in the conventional manner, after the heat treatment, as shown schematically in Fig. 7.1. The vertical p-n junctions, together with their horizontal shallow components (resulting from the diffused n^+ and p^+

layers), are represented by a continuous solid line. High-low horizontal junctions in-between the alternating p-n junctions parallel to the two surfaces are represented by the dashed lines.

Slices were cut in the longitudinal direction from the B-doped silicon crystal used in Section IV at different distances from the periphery. Their oxygen and carbon content was measured and is shown as a function of distance from the periphery in Fig. 4.1. Most slices were then cut into two parts and thin n^+ and p^+ layers were diffused onto the top and bottom at Mobil Tyco Solar Energy Corporation with the cooperation of Mary Cretella. The slices were divided into two lots, each containing slices cut at corresponding distances from the periphery. Slices from one of the lots were heat treated at 450°C for a length of time appropriate to activate the vertical junctions, which varied with the distance from the periphery. No heat treatment was used on the other lot. Contacts were then applied in the conventional way to achieve the structure shown schematically in Fig. 7.1 for the heat treated lot and a conventional BSF structure for the non-heat treated lot.

The EBIC technique (44) was then used to determine the position and the spacing of the p-n junctions. An EBIC image of a solar cell fabricated on a slice cut at 7.8 mm from the periphery and heat treated at 450°C for 18 hours and 50 minutes is shown in Fig. 7.2. The horizontal dark lines are the fingers of the collecting grid; the spacing between them is 3 mm. The parallel bright and dark narrow bands represent the n and p segments, respectively, in the base region of the cell structure, forming a plurality of junctions perpendicular to the surface. The spacing of the junctions is quite irregular and always larger than a few hundred microns, as was

expected from the results presented in Section IV. The shallow alternating p-n and high-low junctions (77) parallel to the bottom and the top surfaces of the cell (Fig. 7.1) are not seen in the EBIC image. It is apparent that a part of the structure, as shown in Fig. 7.1, resembles the BSF cell, but bound by vertical junctions on two sides (Fig. 7.3a). The other part resembles the vertical junction cell, but with a high-low junction on top and a collection p-n junction at the bottom (Fig. 7.3b). No p-n junctions could be observed by the EBIC technique on non-heat treated samples and on samples close to the periphery, even if heat treated for over 20 hours.

VII.3 Conversion efficiency

The I-V characteristics for both lots of solar cells were measured in the dark and under AM2 illumination, provided by natural sunlight on April 3rd, 1980, at MIT. The I-V characteristics in the dark and under illumination for the solar cell whose EBIC picture was shown in Fig. 7.2 are shown in Figs. 7.4 and 7.5, respectively. In Fig. 7.5, the open circuit voltage V_{oc} is given by the voltage value at the intersection between the characteristic and the horizontal axis (V_{oc} = 457 mV); the short circuit current I_{sc} by the current value at the intersection between the characteristic and the vertical axis (I_{sc} = 43.3 mA); the output power by the point on the characteristic in the fourth quadrant where the IV product is a maximum (P_{out} = 13.1 mW); the fill factor, FF = $(P_{out}/V_{oc}I_{sc})$ = 0.663; the overall conversion efficiency η by the ratio between the output power P_{out} and the sunlight power P_{sun} incident on the 2 cm^2 area of the cell ($P_{sun} \cong$ 200 mW, $\eta \cong$ 8.21%).

The short circuit current I_{sc}, the open circuit voltage V_{oc}, the fill factor FF and the efficiency η were determined from the measured I-V charac-

teristics and are shown respectively in Figs. 7.6, 7.7, 7.8 and 7.9 as a function of distance from the periphery of the crystal for both lots of solar cells. It is seen (Fig. 7.6) that the short circuit current is larger for heat treated solar cells than for non-heat treated solar cells, indicating that the collection efficiency has been improved by the introduction of the vertical junctions. On the other hand, the open circuit voltage (Fig. 7.7) and the fill factor (Fig. 7.8) have been degraded by the heat treatment; this results in an overall conversion efficiency (Fig. 7.9) generally lower for heat treated than for non-heat treated cells.

To identify the causes of the degradation of the open circuit voltage, it is important to note that heat treated cells fabricated on slices close to the periphery do not show any substantial degradation of the open circuit voltage (Fig. 7.7); in these cells no formation of p-n junctions could be seen by EBIC measurements. It can be concluded that the degradation of the open circuit voltage is due to the introduction of the vertical p-n junction structure rather than to some other effect caused by heat treatment. The same argument also confirms that the improvement in short circuit current is due to the introduction of the vertical multijunctions; in fact, cells fabricated on slices close to the periphery show only a minor improvement in short circuit current (Fig. 7.6). In contrast, the fill factor is degraded also for heat treated cells fabricated on slices close to the periphery (Fig. 7.8). It can be deduced that the degradation in fill factor is due to some spurious effect due to heat treatment, like introduction and/or diffusion of impurities, and probably can be cured by improving the cleanliness during heat treatment.

The spectral response of the collection efficiency was determined for two cells, one heat treated and one non-heat treated. The short circuit current was measured as a function of wavelength using a common light source (quartz halogen) and a monochromator. The ratio of the short circuit current measured for the two cells is shown in Fig. 7.10 as a function of wavelength. It is seen that the relative collection efficiency increases with wavelength as was expected. This confirms once again that the improvement in short circuit current is due to the introduction of the vertical junctions.

In the case of an ideal diode, the reverse leakage saturation current I_o is defined as the reverse current under reverse applied bias (lower than the breakdown voltage); it does not vary with the applied voltage. The solar cells used in the present study are not ideal diodes and the dark reverse current varies with applied voltage (Fig. 7.4). The reverse current for an applied bias of -1 V was assumed to approximate the reverse saturation current and was determined from the dark characteristics. It is shown in Fig. 7.11 for both lots of solar cells as a function of distance from the periphery. It is seen that the reverse current is generally larger for heat treated than for non-heat treated solar cells. This is consistent with the observed behavior of the open circuit voltage. In fact, the I-V characteristic of a solar cell considered as an ideal diode is (73):

$$I = I_o \left(e^{qV/kT} - 1\right) - I_L \qquad (7.3)$$

where I_L is the light-generated current, q the electronic charge, k Boltz-

mann constant and T the temperature. Solving for the open circuit voltage:

$$V_{oc} = \frac{kT}{q} \ell n \left(\frac{I_L}{I_o} - 1\right) \qquad (7.4)$$

and, therefore, an increase in I_o causes a decrease in V_{oc}. The increase in reverse leakage current can be attributed to an increase in the junction area due to the introduction of the multijunctions upon heat treatment.

A computer simulation model of the cell structure investigated in the present study was developed by Dr. Jim Y. Chi. In this model, the dark reverse leakage current was calculated extending Shockley's analysis of the I-V characteristics for a simple one-dimensional p-n junction geometry (72) to the present geometry. The light-generated current was calculated by solving the minority carrier generation, recombination and transport equations at low injection level under appropriate boundary conditions (74). The model was used to calculate various quantities of interest. The total collection efficiency, the reverse saturation current and the conversion efficiency calculated as a function of the diffusion length are shown in Figs. 7.12, 7.13 and 7.14 respectively. The junction spacing w is used as a parameter and curves relative to a conventional BSF cell are shown for comparison.

In Fig. 7.12 it is seen that the total collection efficiency for the structure under consideration is generally larger than for the conventional BSF cell; small values of the junction spacing can achieve a large improvement in collection efficiency for short diffusion lengths. These results are in good agreement with the increase in short circuit current of about 8% observed in Fig. 7.6.

In Fig. 7.13 it is seen that the reverse saturation current is generally larger for the vertical multijunction structure than for the conventional BSF cell; the difference becomes very small for long diffusion lengths. This is again in agreement with the observed increase in reverse leakage current (Fig. 7.11) and degradation in open circuit voltage (Fig. 7.7).

In Fig. 7.14 it is seen that the total conversion efficiency is generally higher for the vertical multijunction structure, except for short diffusion lengths and large junction spacings. This is the case in the material used in the present study, since the diffusion length measured is shorter than 100 μm (78), while junction spacings are larger than 100 μm. It is therefore to be expected that vertical multijunction solar cells fabricated on silicon with small oxygen striation widths (10 - 50 μm) and heat treated, minimizing all possible contamination effects, will hold an improved conversion efficiency. Further developments of this solar cell structure involve the investigation of the possibility of eliminating turbulence convection during growth and of obtaining closely spaced regular striations by appropriately adjusting the rotation rate and the pulling rate.

Figure Captions

Fig. 7.1 Schematic representation of new photovoltaic cell structure (see text). Light incident from the top.

Fig. 7.2 EBIC image of new photovoltaic cell structure fabricated demonstrating the collection of carriers generated by electron beam excitation. In the micrograph the horizontal dark stripes are the contacts. The vertical light and dark stripes are the n and p regions of the cell. The energy of the electron beam is 10 keV.

Fig. 7.3 Schematic representation of the two parts of the cell; (a) the p-n junction and the high-low junction are at the top and bottom of the cell; (b) part of structure adjacent to that illustrated in (a).

Fig. 7.4 I-V characteristic in the dark for a solar cell fabricated on a slice cut at 7.8 mm from the periphery of a B-doped silicon crystal and heat treated at 450°C for 18 hours and 50 minutes.

Fig. 7.5 I-V characteristic under AM2 illumination of the same solar cell as in Fig. 7.4. The open circuit voltage V_{OC}, the short circuit current I_{SC} and the maximum output power P_{out} are shown in the figure.

Fig. 7.6 Short circuit current I_{SC} under AM2 illumination as a function of distance from the periphery of the crystal.
Δ Heat treated solar cells
⊙ Non-heat treated solar cells

Fig. 7.7 Open circuit voltage V_{OC} under AM2 illumination as a function of distance from the periphery of the crystal.
Δ Heat treated solar cells
⊙ Non-heat treated solar cells

Fig. 7.8 Fill factor FF under AM2 illumination as a function of distance from the periphery of the crystal.
Δ Heat treated solar cells
⊙ Non-heat treated solar cells

Fig. 7.9 Efficiency η for AM2 illumination as a function of distance from the periphery of the crystal.
Δ Heat treated solar cells
⊙ Non-heat treated solar cells

Fig. 7.10 Relative collection efficiency (the ratio of measured short circuit current for the present structure to the conventional structure) versus wavelength.

Fig. 7.11 Reverse current I_0 for an applied bias of -1 V as a function of distance from the periphery of the crystal.
▲ Heat treated solar cells
⊙ Non-heat treated solar cells

Fig. 7.12 Total collection efficiency as a function of diffusion length for the new solar cell structure and a conventional BSF cell structure for AMO illumination. In the computer simulation the surface recombination velocity was 10^6 cm s^{-1}; various values for the spacing between junctions w were used.

Fig. 7.13 Reverse saturation current as a function of diffusion length for the new solar cell structure and a conventional BSF cell structure. In the computer simulation the surface recombination velocity was 10^6 cm s^{-1}; various values for the spacing between junctions w were used.

Fig. 7.14 Conversion efficiency η as a function of diffusion length for the new solar cell structure and a conventional BSF structure for AMO illumination. In the computer simulation various values of the spacing between junctions w were used.

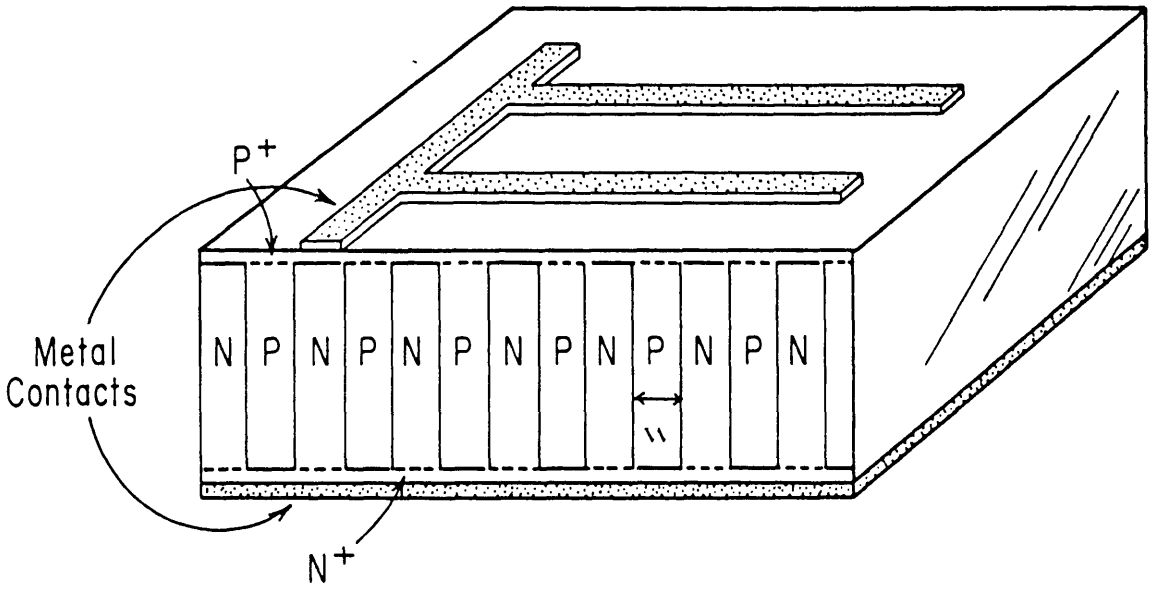

Fig. 7.1

Fig. 7.2

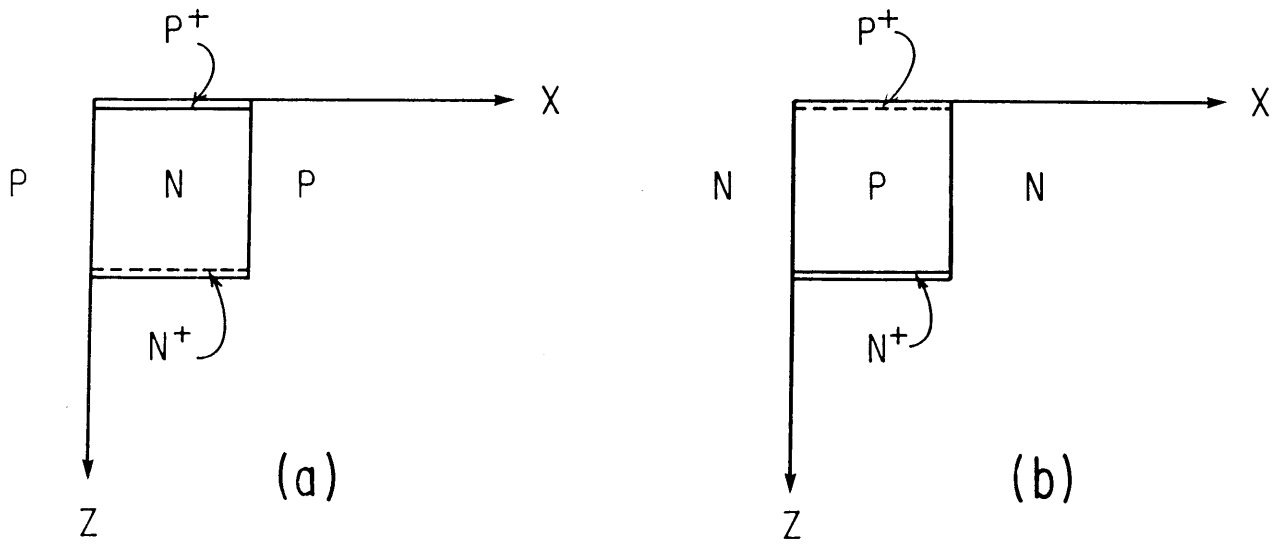

Fig. 7.3

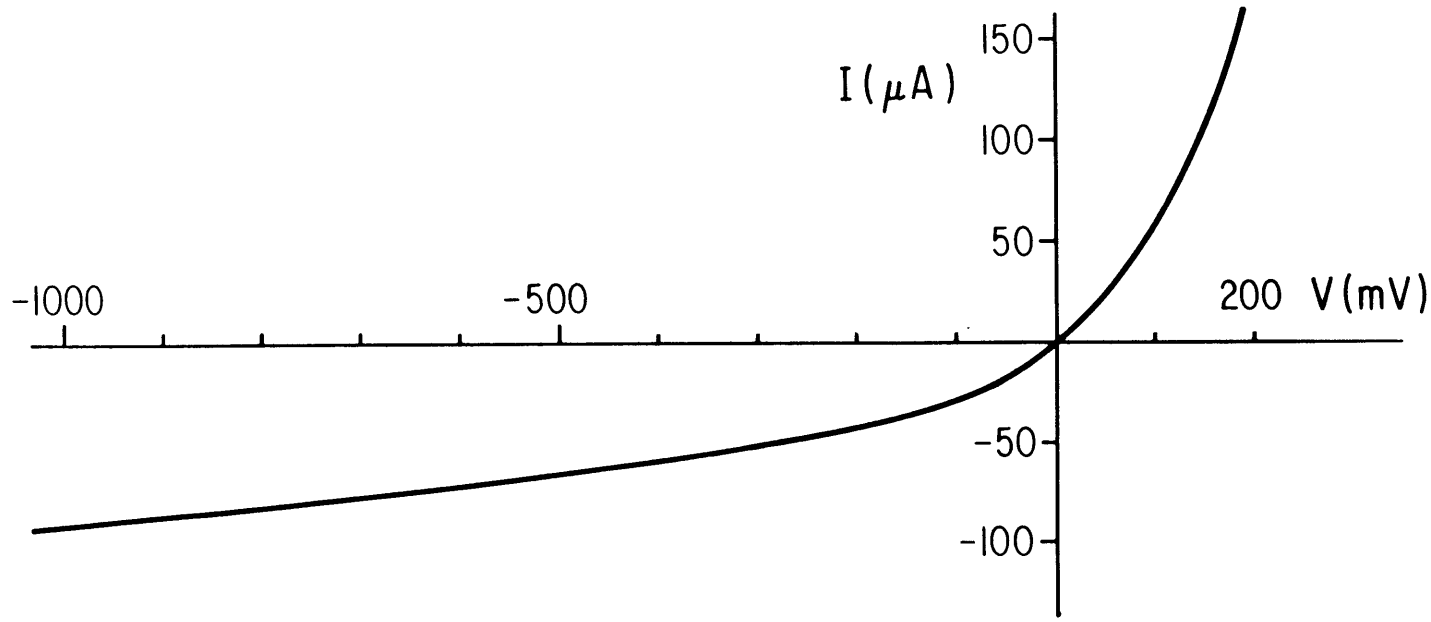

Fig. 7.4

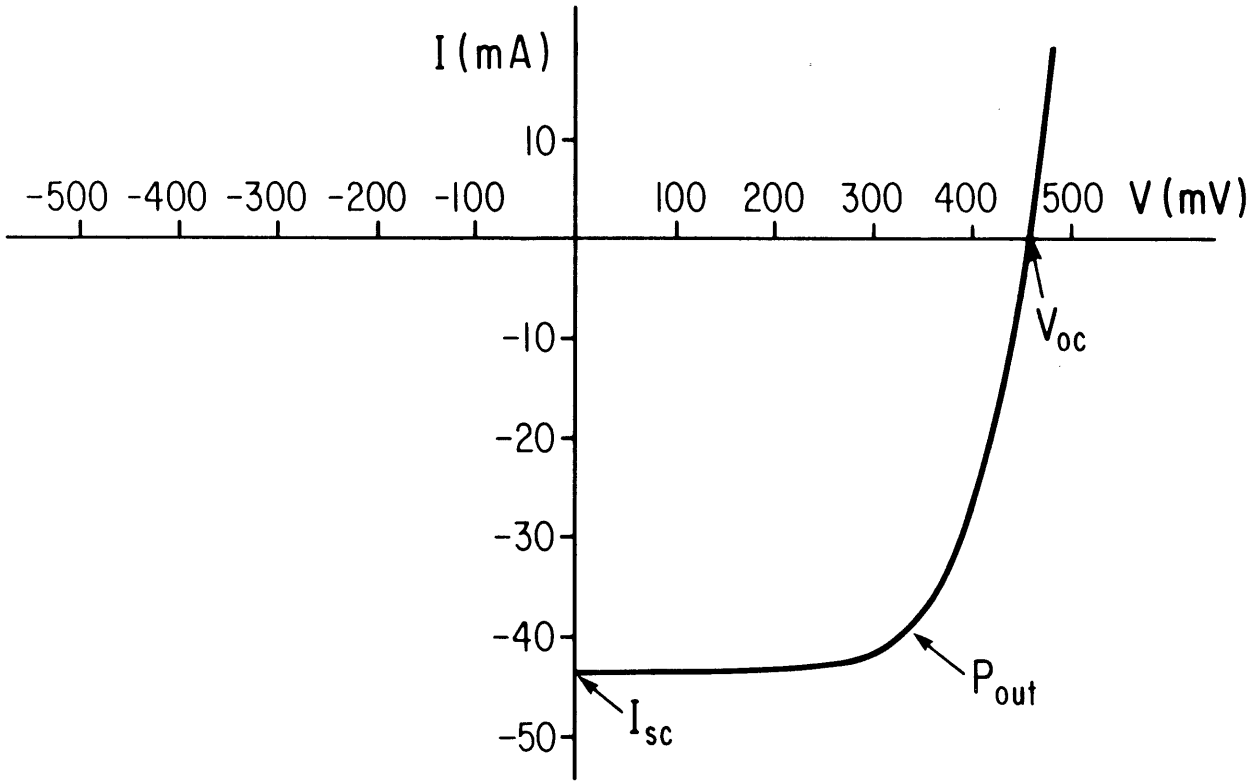
I (mA)
10
-10
-20
-30
-40
-50
-500 -400 -300 -200 -100
100 200 300 400 500 V (mV)
V_{oc}
P_{out}
I_{sc}

Fig. 7.5

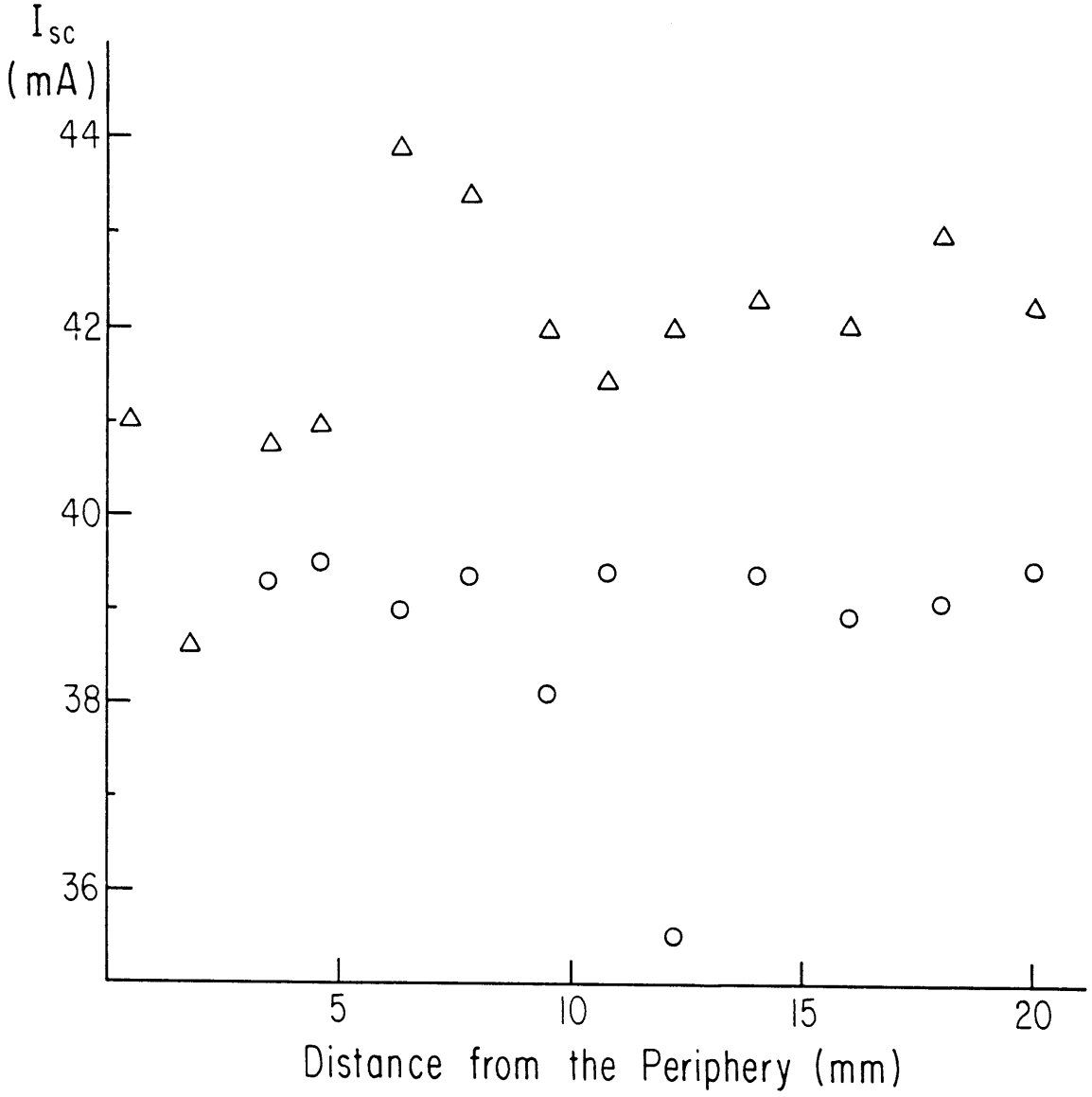

Fig. 7.6

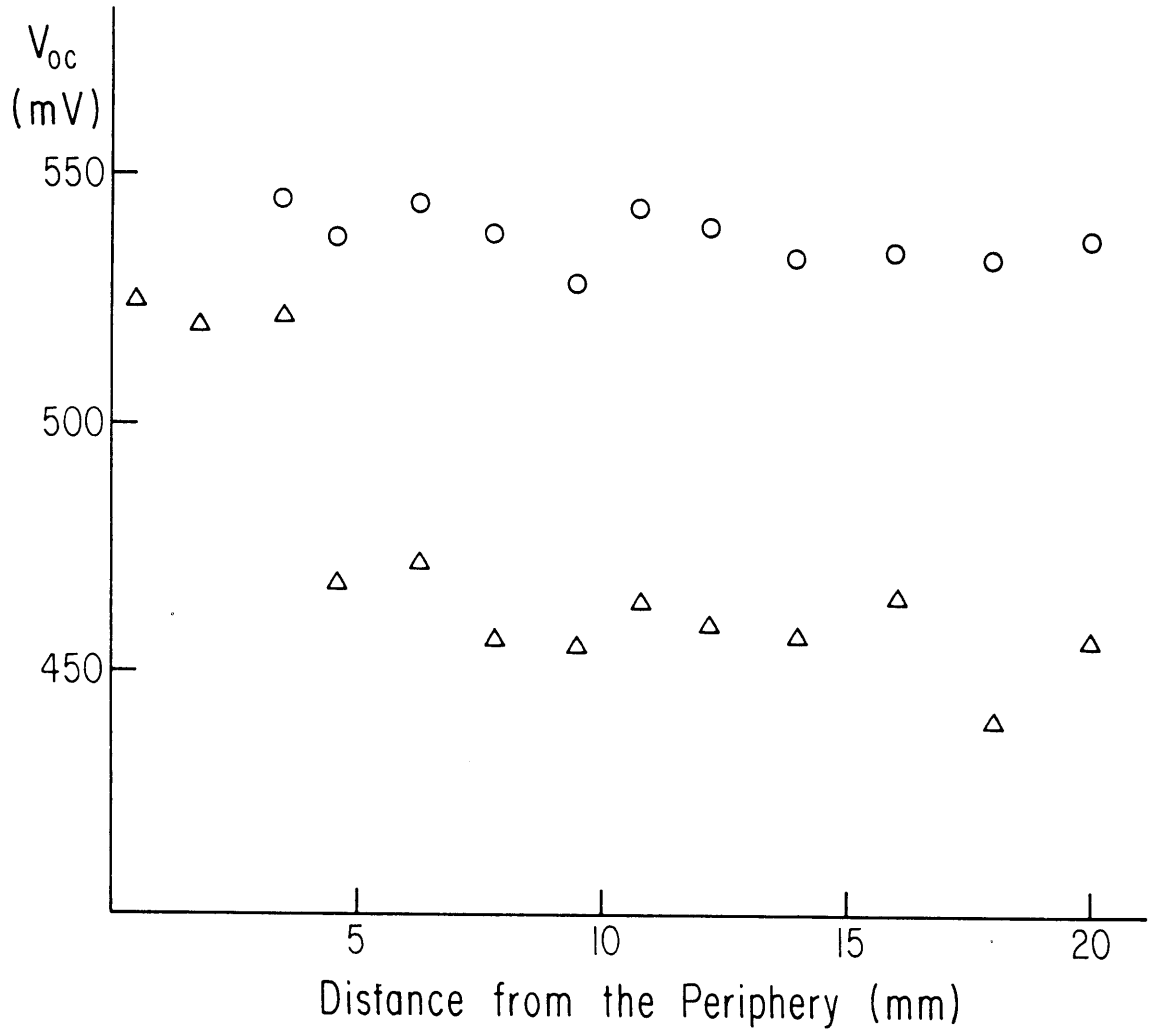

Fig. 7.7

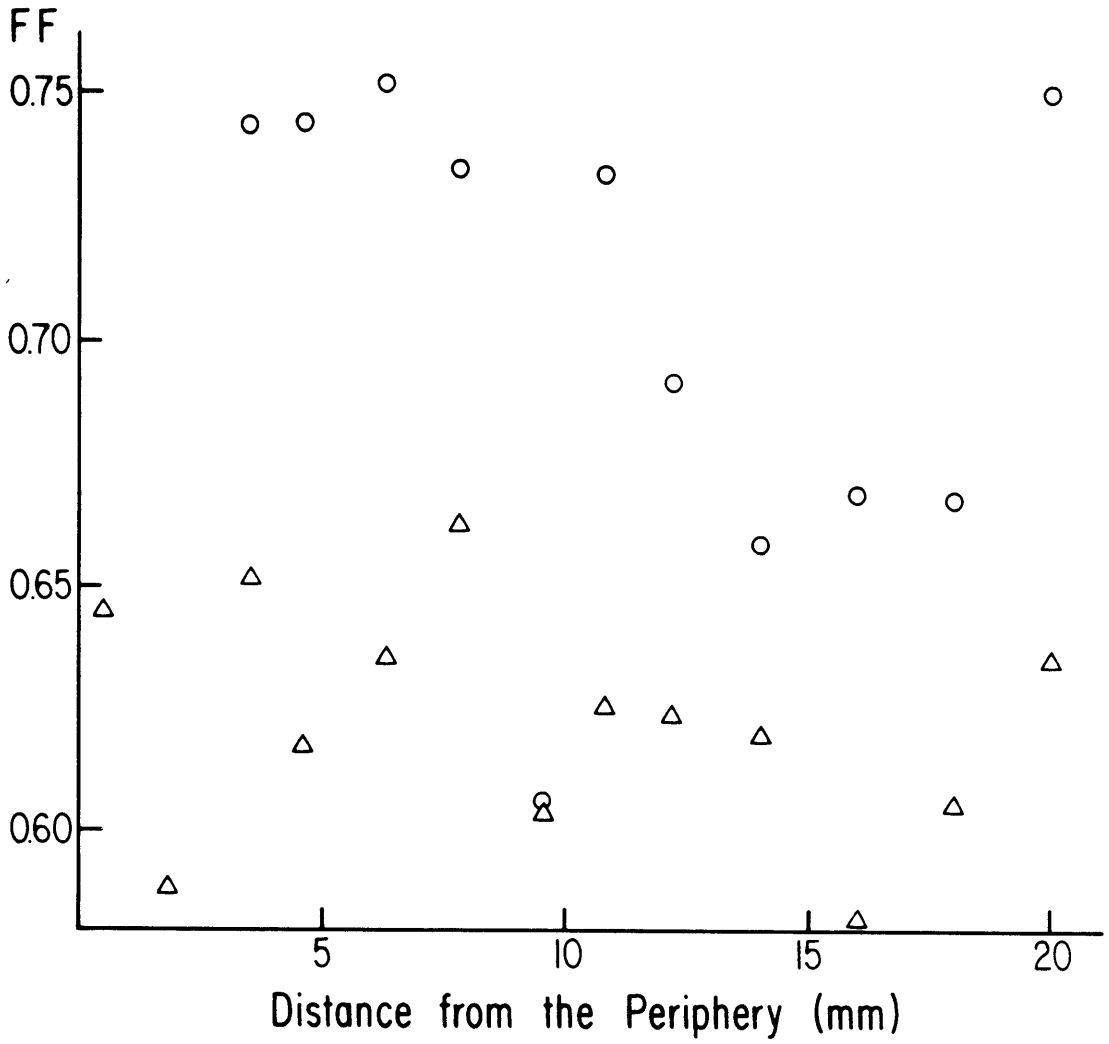

Fig. 7.8

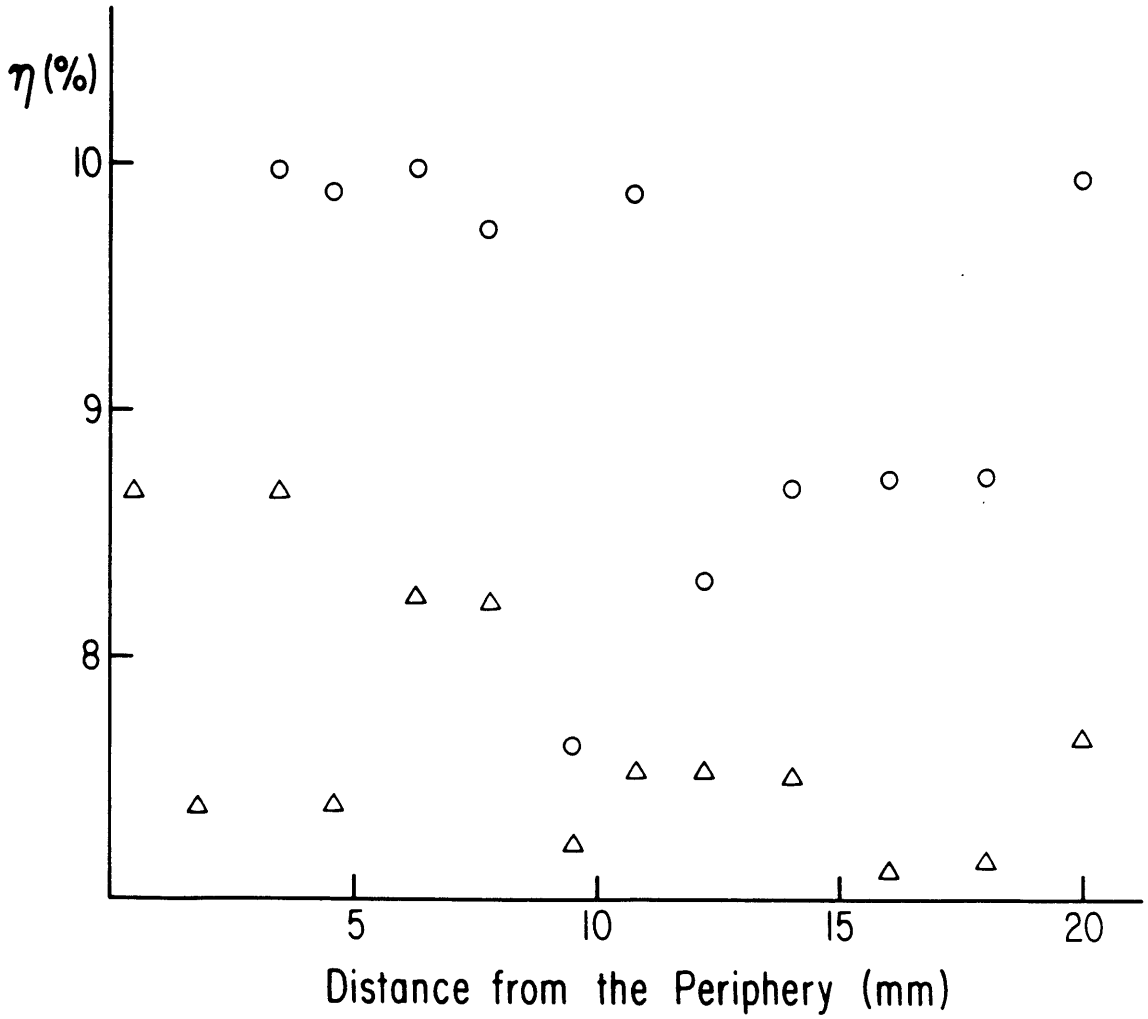

Fig. 7.9

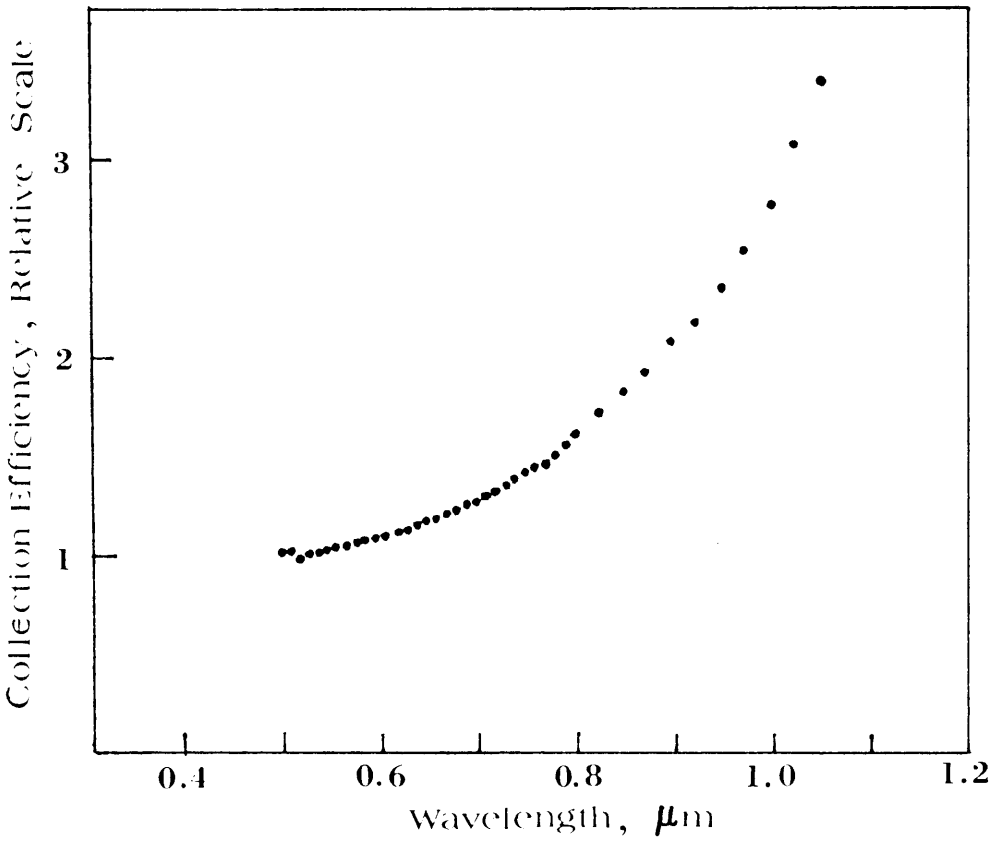
Collection Efficiency, Relative Scale
3
2
1
0.4
0.6
0.8
1.0
1.2
Wavelength, μm

Fig. 7.10

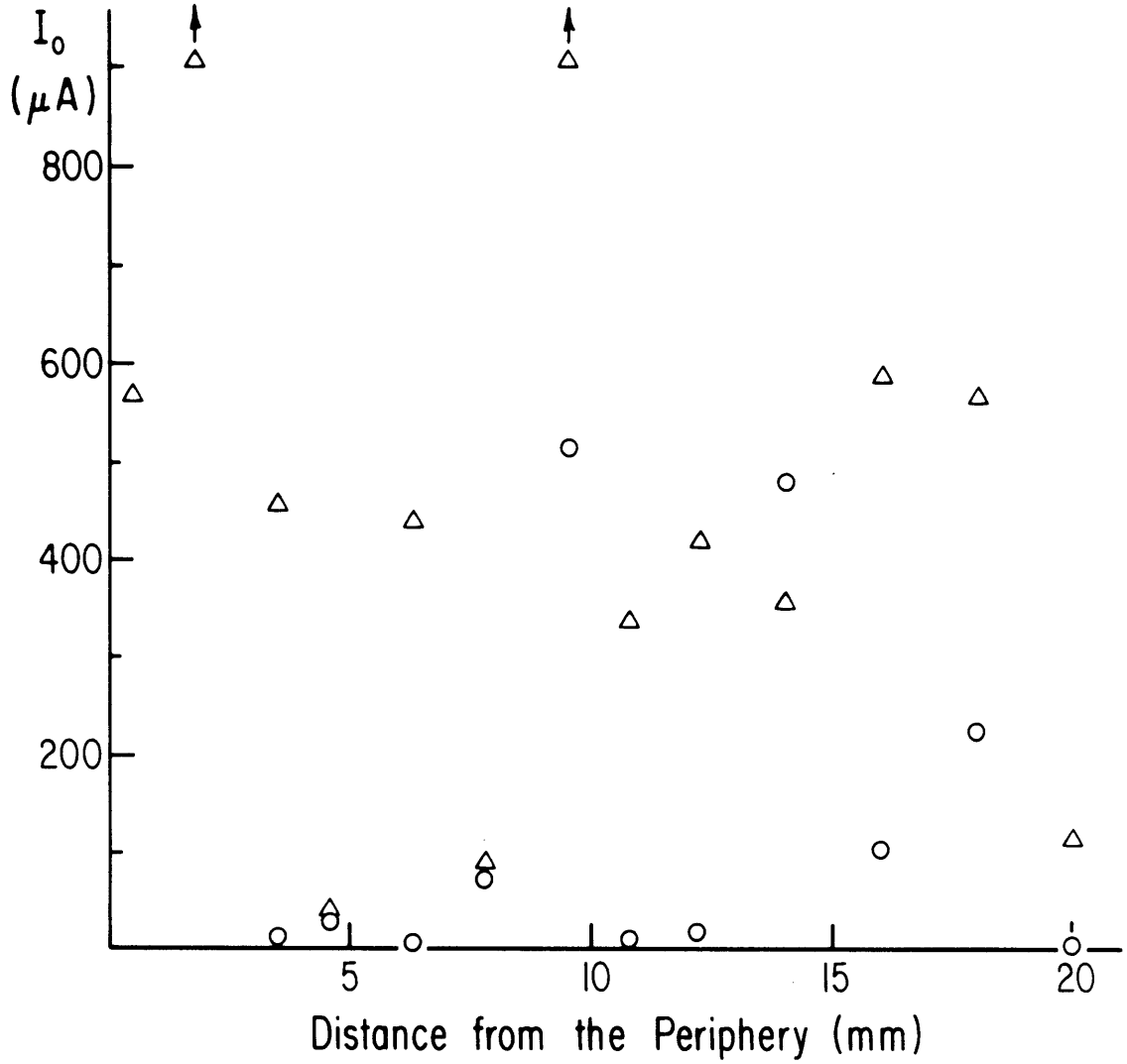
I_0
(μA)
800
600
400
200
5
10
15
20
Distance from the Periphery (mm)

Fig. 7.11

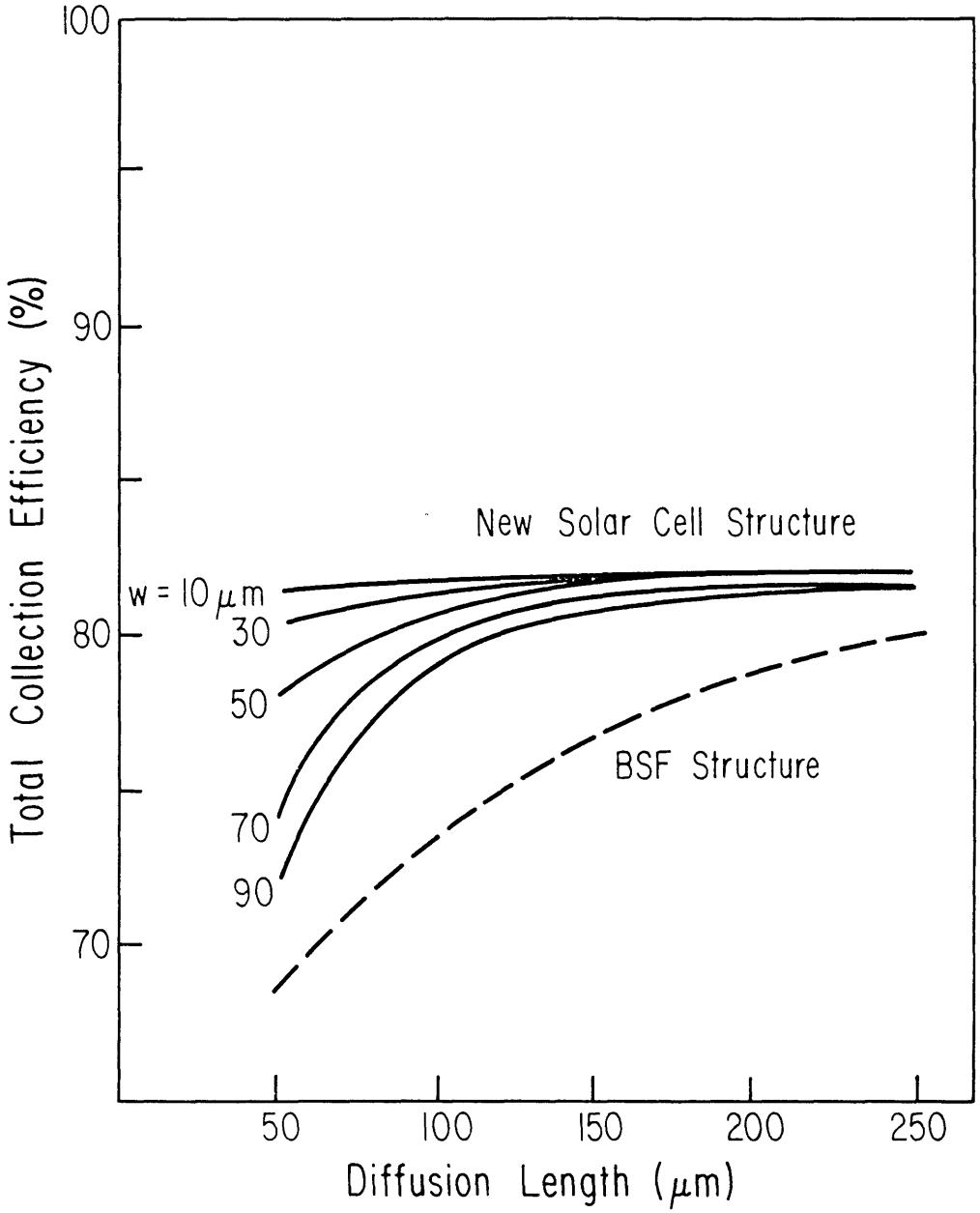
100
90
80
70
Total Collection Efficiency (%)
New Solar Cell Structure
w = 10 μm
30
50
70
90
BSF Structure
50
100
150
200
250
Diffusion Length (μm)

Fig. 7.12

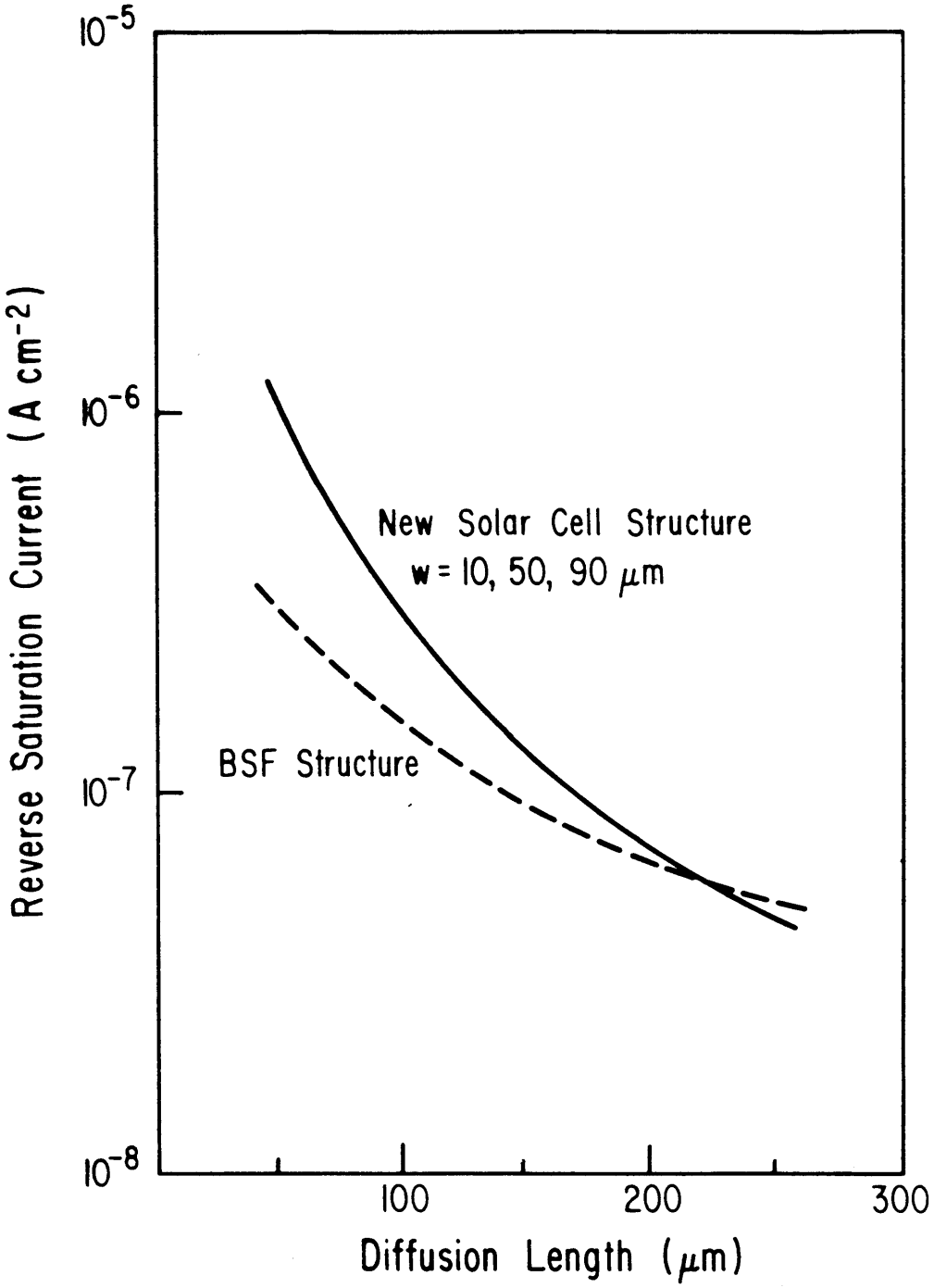
10^{-5}
10^{-6}
10^{-7}
10^{-8}
Reverse Saturation Current ($A\ cm^{-2}$)
New Solar Cell Structure
w = 10, 50, 90 μm
BSF Structure
100
200
300
Diffusion Length (μm)

Fig. 7.13

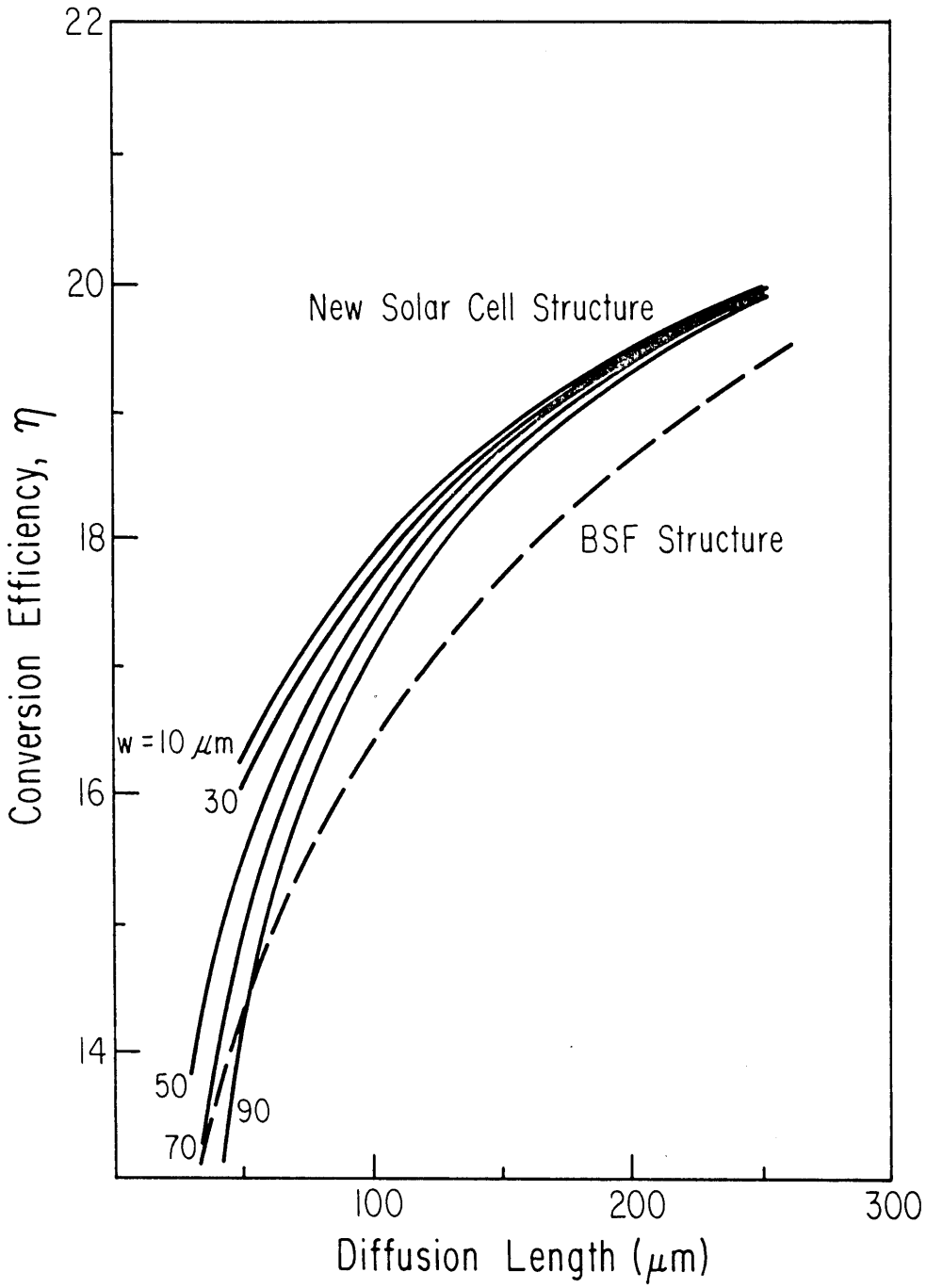
22
20
18
16
14
Conversion Efficiency, η
New Solar Cell Structure
BSF Structure
w = 10 μm
30
50
70
90
100
200
300
Diffusion Length (μm)

Fig. 7.14

VIII. ELECTRON MOBILITY AND FREE CARRIER ABSORPTION IN InP; DETERMINATION OF THE COMPENSATION RATIO

VIII.1 Theoretical considerations

The compensation ratio is a very important parameter in the characterization of semiconducting materials and in particular of III-V compound semiconductors. Walukiewicz et al (53) proposed a method to determine the compensation ratio in GaAs from independent measurements of the electron mobility and of the free carrier absorption, as discussed in Section II.

In the present study the theoretical calculations of the electron mobility and of the free carrier absorption were extended to InP, using an approach similar to ref. 53. The following scattering mechanisms are taken into account: electron-optical phonon, electron-acoustical phonon and electron-ionized impurity scattering. Screening effects due to free carriers are included in the calculations. The piezoelectric acoustical phonon scattering is neglected, since in InP the piezoelectric coupling parameter is ~16 times smaller than that of GaAs, in which the piezoelectric scattering contribution to the room temperature mobility does not exceed 2% (53). The deformation potential optical phonon scattering is also neglected here, since in most compound semiconductors this scattering process is efficiently masked by the much stronger polar interaction. For InP the conduction band parameters and the electron phonon coupling constants are fairly well known. Thus InP is a direct and wide gap semiconductor (E_g ~ 1.35 eV at 300°K) with the conduction band minimum located at the Γ point of the Brillouin zone. The conduction band dispersion relation is well described within the spherical and parabolic approximation with a constant effective mass m*. This approximation allows

direct application of the relationships for the mobility and free carrier absorption given in ref. 53.

VIII.2 Calculation of the electron mobility

Owing to the large optical phonon energy, the electron-optical phonon scattering is an inelastic process and thus the relaxation time approximation cannot be used in the mobility calculations (48,49). Accordingly, a variational procedure is used (53). This procedure does not invoke the Matthiessen rule (according to which average macroscopic mobilities resulting from different scattering mechanisms are summarized, $\frac{1}{\mu} = \sum_i \frac{1}{\mu_i}$), since in III-V compounds it leads to unacceptable errors (53). Thus, in order to find the electron mobility as a function of free carrier concentration and compensation ratio, it is necessary to perform numerical computations.

Figure 8.1 shows the calculated temperature dependence of the total electron mobility in InP with two different free electron concentrations. In addition, the temperature dependence of the two most important component mobilities is plotted. The ionized impurity contribution to the total mobility rapidly decreases with increasing temperature. For the material with the lower dopant concentration the room temperature mobility is practically insensitive to ionized impurity scattering and its value is determined mainly by optical phonon scattering. In such a case, more reliable results for the compensation ratio can be obtained from the mobility value at liquid nitrogen temperature.

The calculated room and liquid nitrogen temperature mobilities as a function of free carrier concentrations and compensation ratio are presented in Tables 8.1 and 8.2.

VIII.3 Calculation of free carrier absorption

In contrast to the mobility, the free carrier absorption may be represented as a sum of absorption coefficients associated with various scattering processes considered in the present work; the total absorption coefficient is:

$$\alpha_t = \alpha_{op} + \alpha_{ac} + \alpha_{imp} \tag{8.1}$$

where α_{op}, α_{ac} and α_{imp} are the absorption coefficients associated with electron-optical phonon, electron-acoustical phonon and electron-ionized impurity interaction, respectively.

Numerical calculations of absorption coefficients were carried out employing appropriate expressions for the component absorption coefficients (53). The results for room and liquid nitrogen temperatures at a wavelength of 10 μm are given in Table 8.3.

As in the case of GaAs (53), it can be shown that the component absorption coefficients at any wavelength λ can be obtained from the following approximate relationships:

$$\alpha_{op,\lambda} = \alpha_{op,\lambda_o} \left(\frac{\lambda}{\lambda_o}\right)^{2.5} \tag{8.2a}$$

$$\alpha_{imp,\lambda} = \alpha_{imp,\lambda_o} \left(\frac{\lambda}{\lambda_o}\right)^{3.5} \tag{8.2b}$$

$$\alpha_{ac,\lambda} = \alpha_{ac,\lambda_o} \left(\frac{\lambda}{\lambda_o}\right)^{1.5} \tag{8.2c}$$

This approximation is valid for n-type InP with free carrier concentrations

up to about 10^{18} cm^{-3} and for wavelengths $\lambda < 10$ μm. The above expressions are valid at larger wavelengths for lower dopant concentrations.

The results of Table 8.3 can be used to determine the absorption coefficient in samples with a given ionized impurity concentration, namely:

$$\alpha_{exp} = (N_{imp}/n)\ \alpha_{imp} + \alpha_{op} + \alpha_{ac} \qquad (8.3)$$

where N_{imp} is the total concentration of ionized impurities and n is the free electron concentration. Using the above relation, one can express the compensation ratio in terms of the experimental and theoretical component absorption coefficients:

$$\theta = \frac{\alpha_{exp} - (\alpha_{op} + \alpha_{ac} + \alpha_{imp})}{\alpha_{exp} + \alpha_{imp} - (\alpha_{op} + \alpha_{ac})} \qquad (8.4)$$

where $\theta = (N_A^-/N_D^+)$, i.e., the ratio of the ionized acceptor to the ionized donor concentrations.

VIII.4 Experimental procedure

Hall effect measurements, conductivity, and infrared absorption have been carried out on n-type InP samples cut from melt grown single crystals with electron concentrations in the range 3×10^{15} - 2.5×10^{18} cm^{-3}. Assessment of the sample homogeneity was found necessary in order to obtain consistent and meaningful results. The measurements carried out for this assessment, namely, the carrier concentration profiling with laser IR scanning and the Hall constant measurements as a function of magnetic field up to 150 kOe, are presented in Section IX. In considerable portions of melt grown crystals the spatial variation of the absorption coefficient at $\lambda = 10.6$ μm was found to exceed 30% of the average value. In such

inhomogeneous samples, the Hall constant exhibited an anomalous magnetic field dependence consistent with the Hall effect analysis of ref. 79. A reliable interpretation of electron mobility and free carrier absorption on the basis of average macroscopic values is not possible for inhomogeneous material. Accordingly, only selected samples with carrier-concentration inhomogeneities not exceeding 10% and exhibiting the standard Hall-constant dependence on magnetic field are considered in this section. For these samples, the electron mobility and electron concentration were obtained from conductivity and Hall-effect measurements. The saturation value of the Hall factor r = 1, was used to determine the electron concentration. In this way common ambiguities associated with the value of the Hall factor r were eliminated. The measured parameters of the samples employed are listed in Table 8.4.

VIII.5 Results and discussion on electron mobility

In the present theoretical treatment, the electron drift mobility was taken as $\mu = \sigma/en$, where σ is the low dc electric field conductivity. Thus, a comparison between theory and experiment requires experimental data of drift mobility rather than of the commonly measured Hall-effect mobility, $\mu_H = r\mu$. Since the present measurements of the Hall constant, R_H, were determined in a high magnetic field, where r = 1, the electron concentration ($n = r/eR_H$) and the drift mobility can be reliably determined. The results on the room-temperature mobility as a function of electron concentration are presented in Fig. 8.2, together with the theoretically calculated values for different compensation ratios θ. It is seen that the presently determined mobility values are below the theoretical limit for uncompensated InP ($\theta = 0$). Utilizing Table 8.1, the values of compensation ratios were

determined for these samples and are given in Table 8.4.

The literature mobility data (80-86) plotted in Fig. 8.2 represent Hall mobilities, and thus it is not surprising that in the region of low electron concentrations, some values slightly exceed the limit of the drift mobility. According to theoretical considerations presented in ref. 87, the Hall factor r in pure InP at room temperature is about 1.25. With increasing electron concentration the value of r decreases, approaching r = 1 for degenerate material. Thus for high electron concentrations, the Hall mobility approaches the drift mobility value, and the literature results fall below the theoretical curve corresponding to uncompensated material.

Mobility data at 77°K are given in Fig. 8.3. At this temperature the difference between the Hall-effect and drift mobility does not exceed 5% (87), i.e., it is within the experimental accuracy of Hall-effect measurements. Thus the present results and the literature data fall below the theoretical curve of $\theta = 0$ over the entire electron concentration range. The compensation ratios determined from Table 8.2 are given in Table 8.4.

The necessity to include the compensation ratio in the theoretical analysis of the mobility is especially evident in the dependence of mobility on temperature. Thus in Fig. 8.4 the experimentally determined mobility is shown as a function of temperature for two InP samples with different free-electron concentrations. The theoretical curves for uncompensated samples lie well above the experimental values and exhibit a distinctly different temperature dependence. On the other hand, as shown in the same figure, there is a very reasonable agreement between theory and experiment if the compensation ratio is taken into account in the theoretical

calculations.

It is of interest to note that, according to the present analysis, melt-grown InP exhibits much lower compensation than that encountered in melt-grown GaAs. This difference is evident in Fig. 8.5, where the normal range of N_{imp}/n is plotted as a function of electron concentration for commercially available high-quality GaAs (53), and for InP. In the low electron-concentration region the melt-grown GaAs is highly compensated, with a total concentration of ionized impurities exceeding by an order of magnitude the free-carrier concentration. InP, on the other hand, even at low concentrations can be obtained by melt growth with a concentration of ionized impurities of the same order of magnitude as the electron concentration. This marked difference is probably related, in part, to the lower melting point of InP (1062°C for InP and 1238°C for GaAs) and thus to the lower concentration of native point defects; point defects in compound semiconductors are known to participate in the formation of compensation centers. Furthermore, the covalent radii of In and P differ by about 40%, whereas those of Ga and As are about the same; thus a dopant impurity is more likely to preferentially occupy In or P sites in InP than Ga or As sites in GaAs (amphoteric or compensating doping).

VIII.6 Results and discussion on free carrier absorption

Room-temperature IR absorption was determined from transmittance measurements employing a Fourier spectrometer. The absorption coefficient α is obtained from eq. 3.1. Values of R as a function of wavelength λ for InP are given in ref. 89.

The present experimental results on the absorption coefficient at λ = 10 μm together with those in ref. 57 are presented in Fig. 8.6 as a function of electron concentration. The theoretical values of the total

absorption coefficient and the absorption components associated with different scattering mechanisms are also shown in this figure. It is seen that the major contribution to free-carrier absorption in InP is provided by optical-phonon scattering. The ionized impurity scattering is of significance only at high concentrations, $n > 10^{17}$ cm^{-3}.

As pointed out in ref. 53, a comparison between the experimental and theoretical dependence of free-carrier absorption on the electron concentration (for samples having different compensation ratios) can be achieved by reducing the experimental absorption coefficient α_{exp} to an absorption coefficient corresponding to zero compensation, $\alpha^*_{exp} \equiv \alpha_{exp} - (N_{imp}/n-1)\alpha_{imp}$ which according to ref. 53 is:

$$\alpha^*_{exp} = \alpha_{exp} - \alpha_{imp}\, 2\theta/(1 - \theta) \qquad (8.5)$$

The values of α^*_{exp} were calculated using the values of compensation ratio determined for each sample from its electron mobility (Table 8.4) and from the computed values of α_{imp} given in Table 8.3. In Fig. 8.7, α^*_{exp} is plotted as a function of carrier concentration together with the theoretical dependence $\alpha_T(n)$. It is seen that good agreement is obtained between theoretical and experimental results.

Using eq. 8.4 and the theoretical values of the absorption coefficient given in Table 8.3 values of the compensation ratios for the samples investigated were obtained. The results are summarized in Table 8.4. It is seen that the values obtained by the optical method are in satisfactory agreement with those determined from electron mobilities.

The theoretically calculated values of the absorption coefficient at 77°K are shown in Fig. 8.8 as a function of carrier concentration. A

comparison with the room-temperature results in Fig. 8.6 shows that the optical-phonon contribution to the total absorption coefficient does not decrease significantly with decreasing temperature. Thus low-temperature IR absorption is not appreciably more sensitive to the ionized impurity scattering than room-temperature absorption. This behavior is significantly different from that of the electron mobility discussed in the previous section. The optical-phonon contribution to the total mobility decreases rapidly with decreasing temperature and thus the low-temperature mobility is very sensitive to the ionized impurity scattering. This different behavior of two closely related processes can be explained as follows. At low temperatures when the optical-phonon occupation number is very small the main contribution to electron optical-phonon scattering consists of transitions in which optical phonons are emitted by electrons. In low dc fields phonon emission requires a transition of an electron from an occupied state at a given energy E to an empty state at an energy lower by the phonon energy $\hbar\omega_0$. Such a process is hardly possible at low temperatures ($kT << \hbar\omega_0$) whereby the density of final unoccupied states is essentially negligible. Free-carrier absorption involves additional interaction with an incident photon. Thus even at low temperatures the phonon emission is energetically possible provided that the energy of the absorbed photon, $h\nu$, is higher than the energy of the emitted phonon $\hbar\omega_0$.

In summary, a practical method for the determination of the compensation ratio in n-type InP has been developed; this method can be applied only for homogeneous samples. In the next section, an investigation of the effect of inhomogeneities is presented.

TABLE 8.1

Electron mobility, carrier concentration, and compensation ratio in n-type InP at 300°K.

Concentration	Compensation ratio 0	0.1	0.2	0.3	0.4	0.5	0.6	0.7	0.75	0.80	0.85	0.90	0.95
	Electron mobility (cm^2/V sec)												
1.0×10^{15}	4710	4690	4660	4620	4570	4510	4410	4270	4160	4020	3820	3490	2900
1.5	4670	4630	4590	4540	4480	4390	4270	4090	3970	3800	3560	3210	2610
2	4640	4600	4550	4490	4410	4300	4160	3960	3810	3630	3380	3010	2420
3	4570	4510	4450	4370	4270	4140	3970	3730	3570	3360	3090	2720	2150
4	4520	4450	4370	4280	4160	4010	3820	3560	3380	3170	2900	2530	1980
5	4460	4390	4300	4190	4060	3900	3690	3410	3230	3020	2750	2380	1840
6	4420	4340	4240	4120	3980	3810	3590	3300	3120	2900	2620	2270	1740
7	4380	4290	4180	4060	3910	3730	3500	3200	3010	2790	2520	2170	1650
8	4330	4230	4120	3990	3830	3640	3410	3110	2920	2700	2440	2090	1570
9	4300	4200	4080	3940	3780	3580	3340	3030	2850	2630	2360	2020	1510
1.0×10^{16}	4250	4140	4010	3870	3700	3500	3250	2950	2760	2550	2290	1950	1450
1.5	4080	3950	3800	3640	3460	3240	2990	2690	2500	2300	2044	1720	1240
2	3960	3820	3660	3480	3290	3070	2810	2510	2330	2120	1880	1560	1100
3	3770	3610	3440	3250	3050	2820	2570	2270	2100	1900	1660	1360	918
4	3630	3460	3280	3090	2880	2660	2400	2110	1940	1750	1510	1220	800
5	3530	3350	3170	2970	2770	2540	2290	2000	1830	1640	1410	1120	718
6	3440	3270	3080	2880	2670	2440	2190	1900	1740	1550	1320	1040	654
7	3370	3190	3000	2800	2590	2360	2120	1830	1660	1480	1250	973	604
8	3310	3130	2940	2730	2530	2300	2050	1770	1600	1410	1190	920	563
9	3260	3070	2880	2680	2470	2250	2000	1710	1550	1360	1140	875	530
1.0×10^{17}	3220	3030	2830	2630	2420	2200	1950	1660	1500	1320	1100	835	501
1.5	3090	2900	2700	2490	2280	2060	1800	1520	1360	1180	970	723	423
2	2960	2760	2560	2350	2140	1910	1660	1370	1210	1040	839	611	345
3	2840	2640	2430	2210	1990	1750	1500	1220	1060	896	712	507	277
4	2770	2560	2340	2120	1890	1650	1400	1120	967	806	633	444	239
5	2720	2500	2270	2050	1820	1570	1320	1040	896	741	577	400	213
6	2680	2450	2220	1990	1760	1510	1260	987	844	694	536	369	194
7	2650	2410	2180	1940	1710	1460	1210	942	802	657	505	346	181
8	2620	2380	2140	1900	1660	1420	1160	900	764	623	477	325	169
9	2590	2350	2110	1860	1630	1380	1130	867	733	596	455	309	160
1.0×10^{18}	2570	2320	2080	1830	1590	1350	1100	839	708	573	436	295	152
1.5	2470	2210	1960	1710	1460	1220	979	737	617	495	373	250	128
2	2390	2130	1870	1620	1380	1140	904	674	561	448	336	224	113
3	2290	2010	1750	1500	1260	1030	811	598	495	393	293	194	98
4	2210	1930	1670	1420	1190	965	755	553	456	361	268	177	89
5	2150	1880	1610	1360	1140	920	717	523	431	340	252	166	83
6	2100	1830	1560	1320	1100	886	687	501	411	325	241	158	79
7	2070	1790	1530	1290	1070	861	667	484	398	314	232	152	76
8	2040	1760	1500	1260	1040	838	647	470	386	304	225	148	74
9	2010	1740	1480	1240	1020	821	635	462	378	296	219	144	72
1.0×10^{19}	1990	1710	1460	1230	1010	809	624	452	370	289	215	141	71

TABLE 8.2

Computed values of electron mobility in n-type InP at 77°K.

Concentration	Compensation ratio 0	0.1	0.2	0.3	0.4	0.5	0.6	0.7	0.75	0.8	0.85	0.9	0.95
	Electron mobility (cm^2/V sec)												
1.0×10^{13}	3.06×10^5	2.98×10^5	2.88×10^5	2.77×10^5	2.63×10^5	2.46×10^5	2.25×10^5	1.99×10^5	1.83×10^5	1.64×10^5	1.42×10^5	1.15×10^5	8.01×10^4
1.5	2.91	2.80	2.68	2.54	2.39	2.20	1.98	1.72	1.56	1.39	1.19	9.58×10^4	6.64
2	2.77	2.65	2.52	2.37	2.20	2.01	1.79	1.53	1.39	1.23	1.05	8.41	5.78
3	2.56	2.42	2.27	2.11	1.94	1.74	1.53	1.30	1.17	1.03	8.76×10^4	6.97	4.72
4	2.38	2.24	2.08	1.92	1.75	1.56	1.36	1.15	1.03	9.05×10^4	7.68	6.09	4.05
5	2.25	2.09	1.94	1.77	1.61	1.43	1.24	1.04	9.33×10^4	8.19	6.92	5.47	3.58
6	2.13	1.98	1.82	1.66	1.49	1.32	1.15	9.60×10^4	8.60	7.54	6.36	5.00	3.22
7	2.03	1.87	1.72	1.56	1.40	1.24	1.07	8.96	8.02	7.02	5.91	4.62	2.94
8	1.92	1.77	1.62	1.47	1.31	1.16	1.00	8.35	7.47	6.52	5.48	4.26	2.68
9	1.87	1.71	1.56	1.41	1.26	1.11	9.60×10^4	8.00	7.15	6.23	5.23	4.04	2.51
1.0×10^{14}	1.80×10^5	1.65×10^5	1.50×10^5	1.35×10^5	1.21×10^5	1.06×10^5	9.16×10^4	7.62×10^4	6.81×10^4	5.93×10^4	4.96×10^4	3.81×10^4	2.35×10^4
1.5	1.55	1.41	1.27	1.14	1.02	8.91×10^4	7.65	6.33	5.63	4.87	4.02	3.03	1.80
2	1.38	1.25	1.13	1.01	8.97×10^4	7.85	6.72	5.53	4.89	4.20	3.44	2.55	1.48
3	1.17	1.06	9.49×10^4	8.46×10^4	7.50	6.33	5.55	4.52	3.97	3.37	2.71	1.96	1.10
4	1.04	9.36×10^4	8.39	7.47	6.60	5.72	4.84	3.90	3.40	2.86	2.27	1.62	8.95×10^3
5	9.46×10^4	8.50	7.60	6.75	5.95	5.14	4.32	3.45	2.99	2.50	1.97	1.39	7.58
6	8.76	7.86	7.02	6.22	5.47	4.71	3.93	3.12	2.69	2.34	1.75	1.23	6.62
7	8.21	7.36	6.56	5.80	5.09	4.36	3.63	2.86	2.46	2.03	1.58	1.10	5.91
8	7.74	6.93	6.17	5.44	4.76	4.07	3.37	2.64	2.26	1.86	1.44	1.00	5.33
9	7.36	6.58	5.85	5.15	4.49	3.83	3.16	2.46	2.10	1.72	1.33	9.20×10^3	4.88
1.0×10^{15}	7.04	6.29	5.58	4.91	4.27	3.63	2.98	2.31	1.97	1.61	1.24	8.53	4.51
1.5	5.87	5.22	4.60	4.01	3.46	2.90	2.35	1.80	1.52	1.23	9.37×10^3	6.37	3.33
2	5.16	4.56	4.00	3.47	2.97	2.47	1.98	1.50	1.26	1.01	7.67	5.18	2.70
3	4.27	3.74	3.25	2.79	2.36	1.95	1.54	1.15	9.58×10^3	7.67×10^3	5.77	3.87	2.00
4	3.72	3.25	3.80	2.39	2.01	1.64	1.29	9.56×10^2	7.93	6.32	4.74	3.17	1.63
5	3.33	2.89	2.48	2.11	1.76	1.43	1.12	8.24	6.82	5.42	4.05	2.71	1.39
6	3.05	2.64	2.26	1.90	1.59	1.28	1.00	7.34	6.06	4.81	3.59	2.39	1.23
7	2.82	2.43	2.07	1.74	1.45	1.67	9.07×10^2	6.63	5.47	4.34	3.23	2.15	1.10
8	2.63	2.26	1.92	1.61	1.34	1.07	8.34	6.08	5.01	3.97	2.95	1.96	1.01
9	2.48	2.13	1.80	1.51	1.25	1.00	7.76	5.65	4.65	3.68	2.74	1.82	9.30×10^2
1.0×10^{16}	2.35×10^4	2.01×10^4	1.70×10^4	1.42×10^4	1.17	9.39×10^3	7.26×10^3	5.28×10^3	4.34×10^3	3.43×10^3	2.53×10^3	1.70×10^3	8.66×10^2
1.5	1.92	1.63	1.37	1.14	9.32×10^3	7.42	5.70	4.12	3.38	2.67	1.98	1.31	6.67
2	1.67	1.41	1.18	9.73×10^3	7.95	6.31	4.83	3.48	2.86	2.25	1.67	1.10	5.58
3	1.38	1.15	9.55×10^3	7.95	6.39	5.05	3.86	2.77	2.27	1.78	1.32	8.69×10^2	4.38
4	1.20	1.00	8.30	6.81	5.52	4.36	3.32	2.38	1.95	1.53	1.13	7.42	3.73
5	1.08	9.04×10^3	7.48	6.12	4.96	3.91	2.97	2.13	1.74	1.36	1.00	6.60	3.31
6	1.00	8.34	6.89	5.64	4.56	3.59	2.73	1.95	1.59	1.25	9.20×10^2	6.03	3.02
7	9.36×10^3	7.79	6.43	5.25	4.24	3.34	2.53	1.81	1.48	1.16	8.53	5.58	2.79
8	8.68	7.22	5.96	4.87	3.94	3.10	2.36	1.69	1.38	1.08	7.99	5.24	2.62
9	8.44	7.02	5.78	4.72	3.81	2.99	2.27	1.62	1.32	1.03	7.59	4.97	2.48
1.0×10^{17}	8.08	6.71	5.53	4.51	3.64	2.85	2.16	1.54	1.26	9.84×10^2	7.23	4.72	2.35
1.5	6.92	5.73	4.71	3.84	3.09	2.42	1.83	1.30	1.06	8.29	6.08	3.97	1.97
2	6.22	5.15	4.22	3.44	2.76	2.16	1.63	1.16	9.45×10^2	7.38	5.40	3.52	1.75
3	5.38	4.45	3.65	2.96	2.38	1.86	1.40	9.96×10^2	8.09	6.31	4.62	3.01	1.49
4	4.90	4.04	3.31	2.69	2.16	1.68	1.27	8.99	7.30	5.69	4.16	2.71	1.34
5	4.63	3.82	3.12	2.53	2.03	1.58	1.19	8.43	6.84	5.33	3.90	2.53	1.25
6	4.31	3.55	2.91	2.36	1.89	1.47	1.11	7.86	6.38	4.97	3.63	2.36	1.17
7	4.09	3.38	2.76	2.24	1.79	1.40	1.05	7.46	6.05	4.72	3.45	2.24	1.11
8	3.96	3.27	2.67	2.16	1.73	1.35	1.02	7.20	5.84	4.55	3.33	2.16	1.07
9	3.88	3.19	2.61	2.11	1.69	1.32	9.91×10^2	7.01	5.68	4.42	3.23	2.10	1.04
1.0×10^{18}	3.74	3.07	2.51	2.04	1.63	1.27	9.57	6.78	5.48	4.28	3.12	2.03	1.01
1.5	3.37	2.79	2.26	1.83	1.47	1.14	8.61	6.12	4.98	3.85	2.81	1.82	9.00×10^1
2	3.71	2.61	2.12	1.72	1.38	1.09	8.02	5.79	4.64	3.63	2.64	1.67	8.50
3	2.70	2.37	2.00	1.48	1.34	9.16×10^2	7.51	5.33	4.34	3.34	2.36	1.59	7.60

TABLE 8.3

Free carrier absorption.

Concentration cm^{-3}	300 °K $m^* = 0.078$			77 °K $m^* = 0.082$		
	α_{imp}	α_{ac}	α_{op}	α_{imp}	α_{ac}	α_{op}
1.0×10^{16}	0.004	0.034	0.623	0.003	0.005	0.320
1.5	0.008	0.052	0.932	0.007	0.008	0.476
2	0.014	0.069	1.239	0.012	0.011	0.629
3	0.031	0.104	1.850	0.028	0.016	0.928
4	0.056	0.139	2.456	0.048	0.022	1.217
5	0.086	0.173	3.051	0.075	0.028	1.503
6	0.123	0.208	3.646	0.106	0.033	1.780
7	0.167	0.243	4.240	0.143	0.039	2.053
8	0.217	0.278	4.815	0.185	0.045	2.321
9	0.273	0.313	5.397	0.232	0.050	2.588
1.0×10^{17}	0.314	0.325	5.578	0.284	0.056	2.849
1.5	0.690	0.491	8.227	0.617	0.086	4.127
2	1.201	0.660	10.79	1.066	0.117	5.366
3	2.602	1.005	15.75	2.296	0.181	7.793
4	4.474	1.360	20.52	3.949	0.250	10.19
5	6.790	1.726	25.16	6.009	0.322	12.60
6	9.510	2.100	29.65	8.460	0.398	15.02
7	12.64	2.488	34.11	11.27	0.476	17.41
8	16.13	2.879	38.44	14.49	0.560	19.90
9	20.00	3.285	42.75	18.05	0.646	22.38
1.0×10^{18}	24.22	3.699	47.01	21.96	0.736	24.89
1.5	50.28	5.912	67.80	46.69	1.229	37.69
2	83.91	8.354	88.02	78.85	1.798	50.91
3	170.3	13.87	127.0	165.13	3.147	78.60
4	276.7	20.12	164.1	276.8	4.751	98.46
5	396.1	26.98	199.6	405.0	6.57	118.6
6	522.8	34.34	233.4	533.3	8.527	137.7

TABLE 8.4

Compensation ratios determined from mobility and ir absorption measurements.

Sample	Electron concentration (cm^{-3})		Electron mobility $cm^2/V\,s$		Compensation ratio, θ		
	300 °K	77 °K	300 °K	77 °K	mobility 300 °K	77 °K	absorption 300 °K
1	1.9×10^{15}	1.9×10^{15}	3950	20000		0.5[a]	
2	3.5×10^{15}	3.0×10^{15}	4340	30500	0.23	0.22	—
3	4.2×10^{15}	3.6×10^{15}	3850	18500	0.57	0.48	—
4	1.1×10^{16}	7.0×10^{15}	2220	5150	0.86	0.76	—
5	5.7×10^{16}	3.9×10^{16}	2800	3850	0.35	0.56	—
6	6.3×10^{16}	4.6×10^{16}	2710	3740	0.37	0.54	—
7	3.3×10^{17}	3.3×10^{17}	2130	2210	0.33	0.40	0.38
8	4.1×10^{17}	3.2×10^{17}	2390	2970	0.17	0.29	0.29
9	7.0×10^{17}	6.6×10^{17}	2050	2100	0.27	0.34	0.4
10	8.0×10^{17}	8.0×10^{17}	1800	1650		0.36[a]	
11	2.45×10^{18}	2.4×10^{18}	1620	1650	0.28	0.3	0.31

a) Compensation determined from mobility vs temperature.

Figure Captions

Fig. 8.1 Theoretical temperature dependence of electron mobility in uncompensated InP (see text).

Fig. 8.2 Theoretical (solid lines) and experimental values of mobility at 300°K as a function of electron concentration in n-type InP for various compensation ratios: +, present results (drift mobility); other experimental results correspond to measured Hall mobility; I, ref. 80; o, ref. 81; ▲, ref. 82; X, ref. 83; ▽, ref. 84; ●, ref. 85; △, ref. 86.

Fig. 8.3 Theoretical (solid lines) and experimental values of mobility at 77°K as a function of electron concentration in n-type InP for various compensation ratios: +, present results (drift mobility); other experimental points correspond to reported Hall mobility values; I, ref. 80; ▲, ref. 82; ▽, ref. 84; ●, ref. 85; △, ref. 86; ■, ref. 88.

Fig. 8.4 Experimental (+) and theoretical (lines) values of electron mobility in n-type InP as a function of temperature. Dashed lines correspond to uncompensated material. Solid lines represent electron mobilities calculated using a compensation ratio θ independent of temperature.

Fig. 8.5 Normal range of N_{imp}/n as a function of electron concentration in available melt-grown InP and GaAs (see text).

Fig. 8.6 Theoretical and experimental values of the room-temperature (300°K) absorption coefficient as a function of electron concentration in InP (for λ = 10 μm). ● , present results; ✗, ref. 57.

Fig. 8.7 Theoretical (solid line) and experimental values (obtained in present study) of the absorption coefficient reduced to zero compensation (see text).

Fig. 8.8 Theoretical and experimental (ref. 57) values of low-temperature (77°K) free-carrier absorption coefficient in n-type InP.

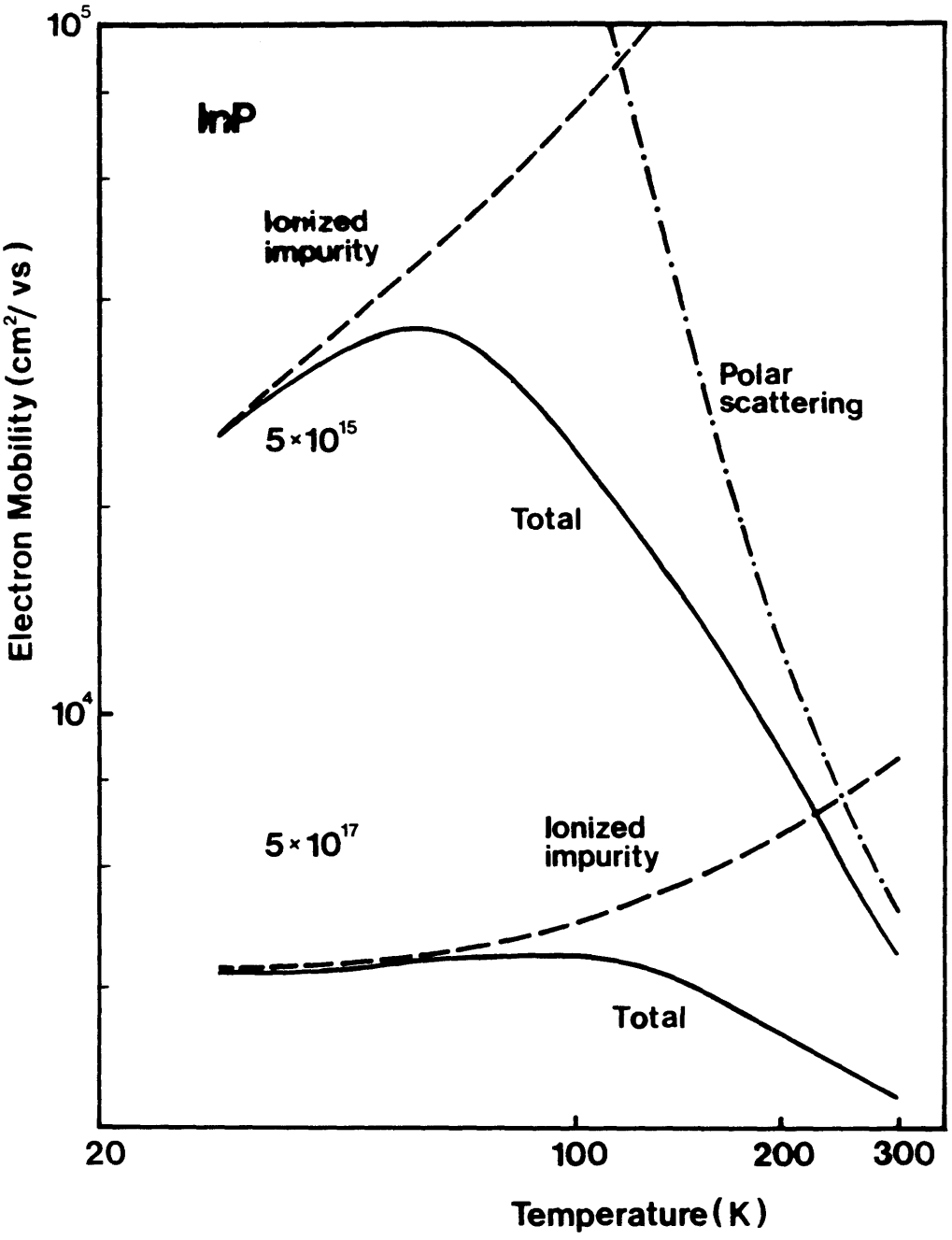
InP
Ionized impurity
Polar scattering
5×10^15
Total
5×10^17
Ionized impurity
Total
Electron Mobility (cm²/ vs)
10^5
10^4
20
100
200
300
Temperature (K)

Fig. 8.1

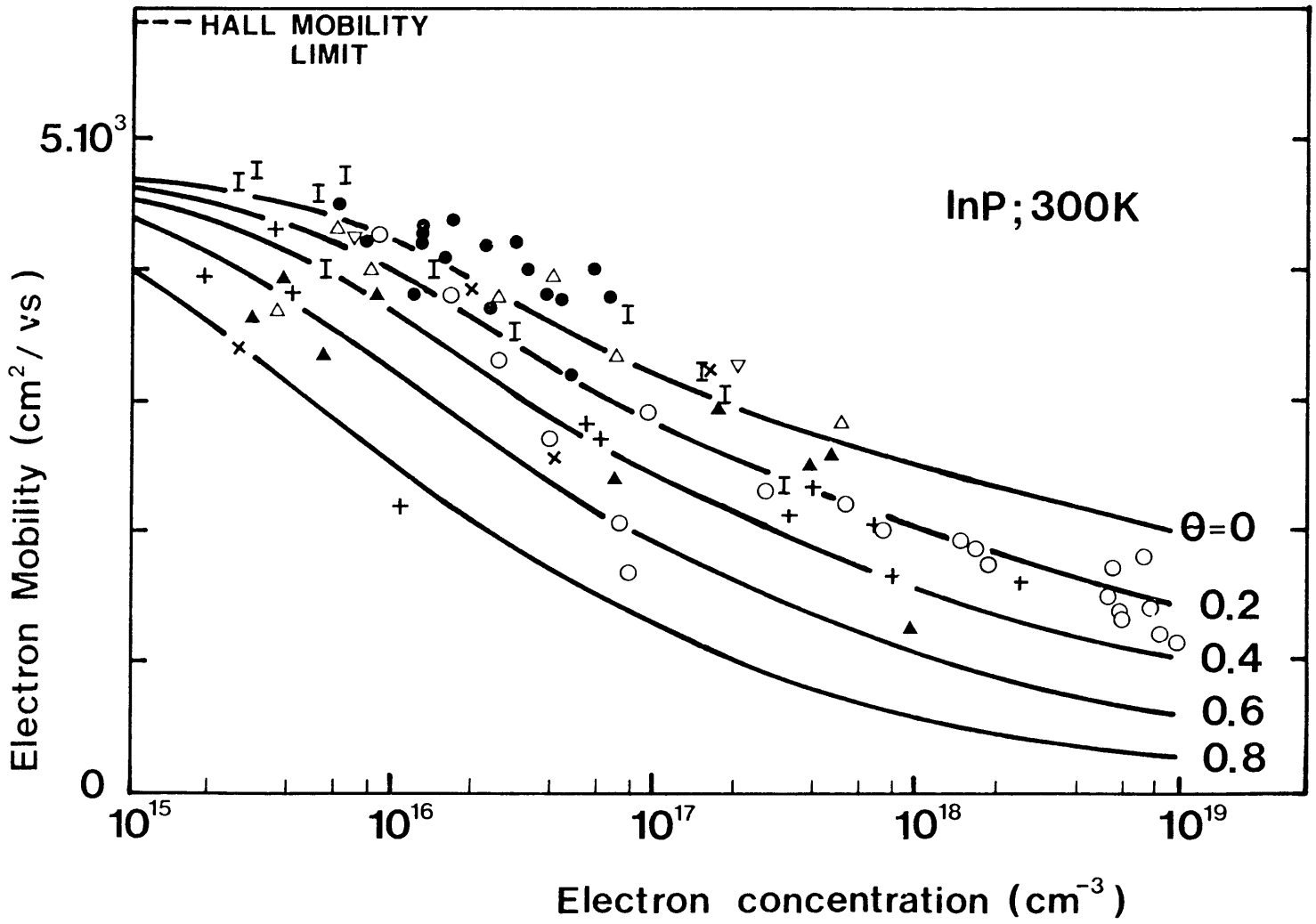
HALL MOBILITY LIMIT
InP; 300K
5.10^3
0
Electron Mobility (cm^2 / vs)
θ=0
0.2
0.4
0.6
0.8
10^15
10^16
10^17
10^18
10^19
Electron concentration (cm^-3)

Fig. 8.2

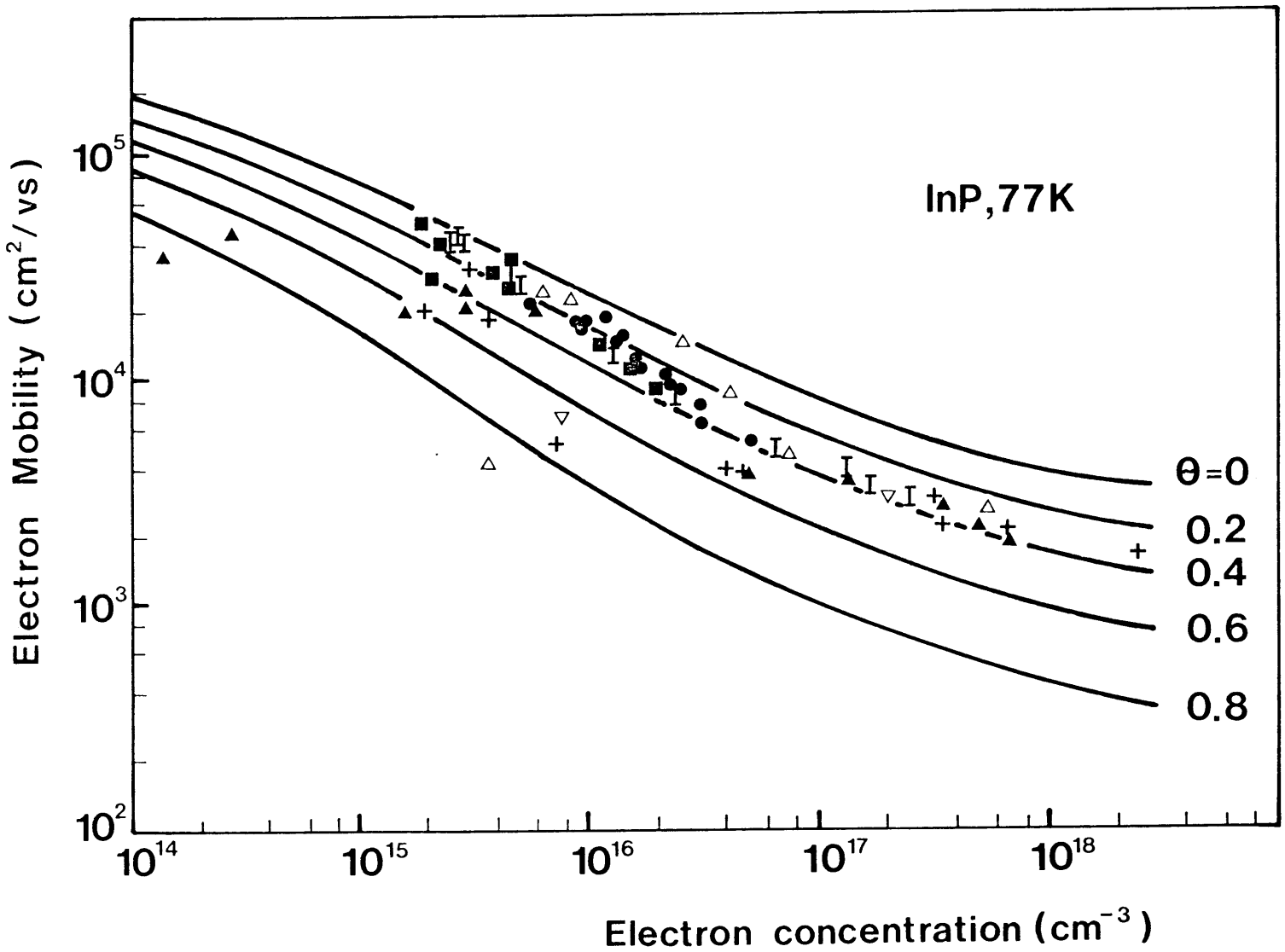
InP,77K
Electron Mobility (cm²/vs)
Electron concentration (cm⁻³)
10⁵
10⁴
10³
10²
10¹⁴
10¹⁵
10¹⁶
10¹⁷
10¹⁸
θ=0
0.2
0.4
0.6
0.8

Fig. 8.3

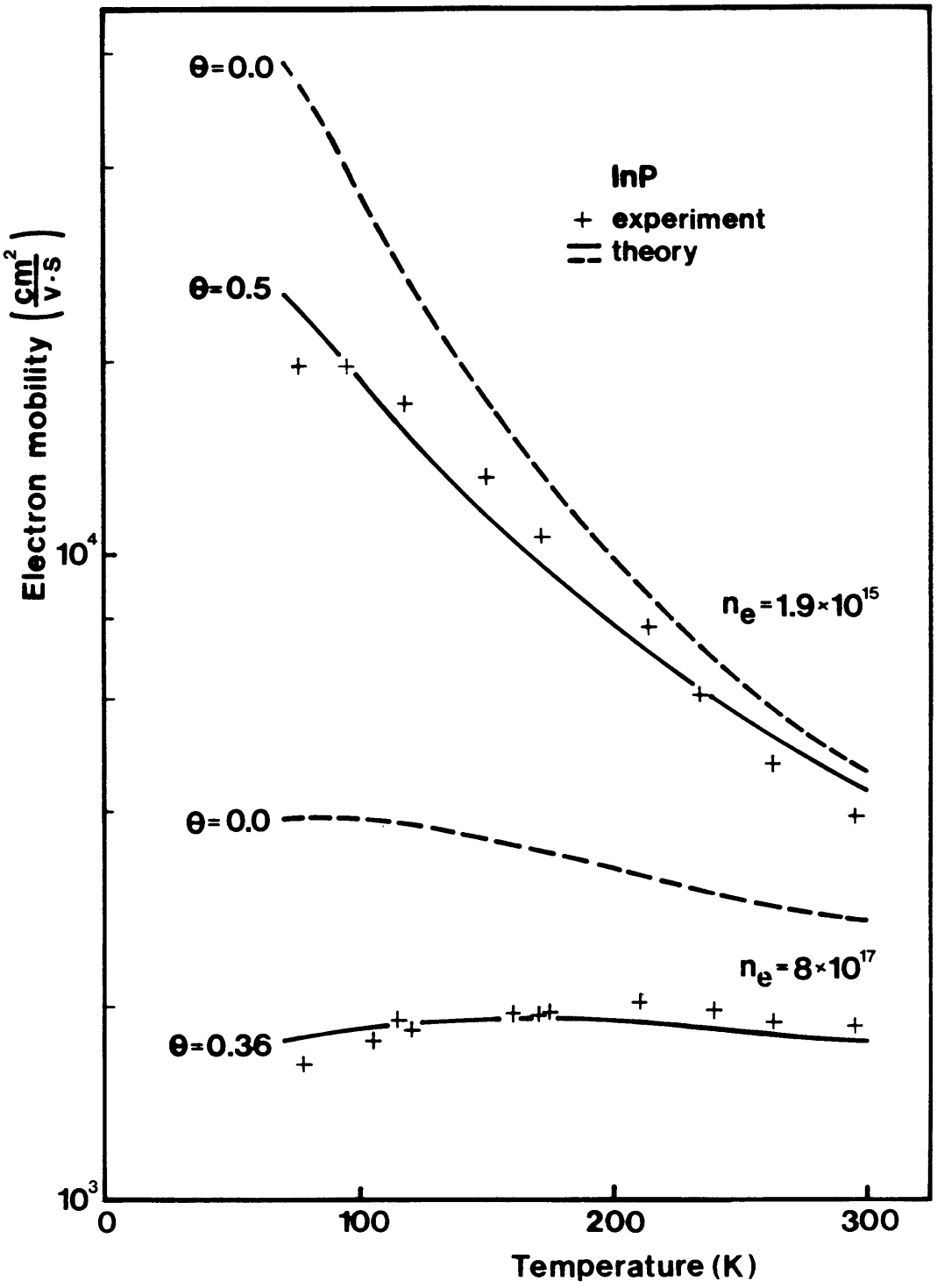
θ=0.0
InP
+ experiment
= theory
θ=0.5
Electron mobility (cm²/V·s)
10⁴
n_e=1.9×10¹⁵
θ=0.0
n_e=8×10¹⁷
θ=0.36
10³
0
100
200
300
Temperature (K)

Fig. 8.4

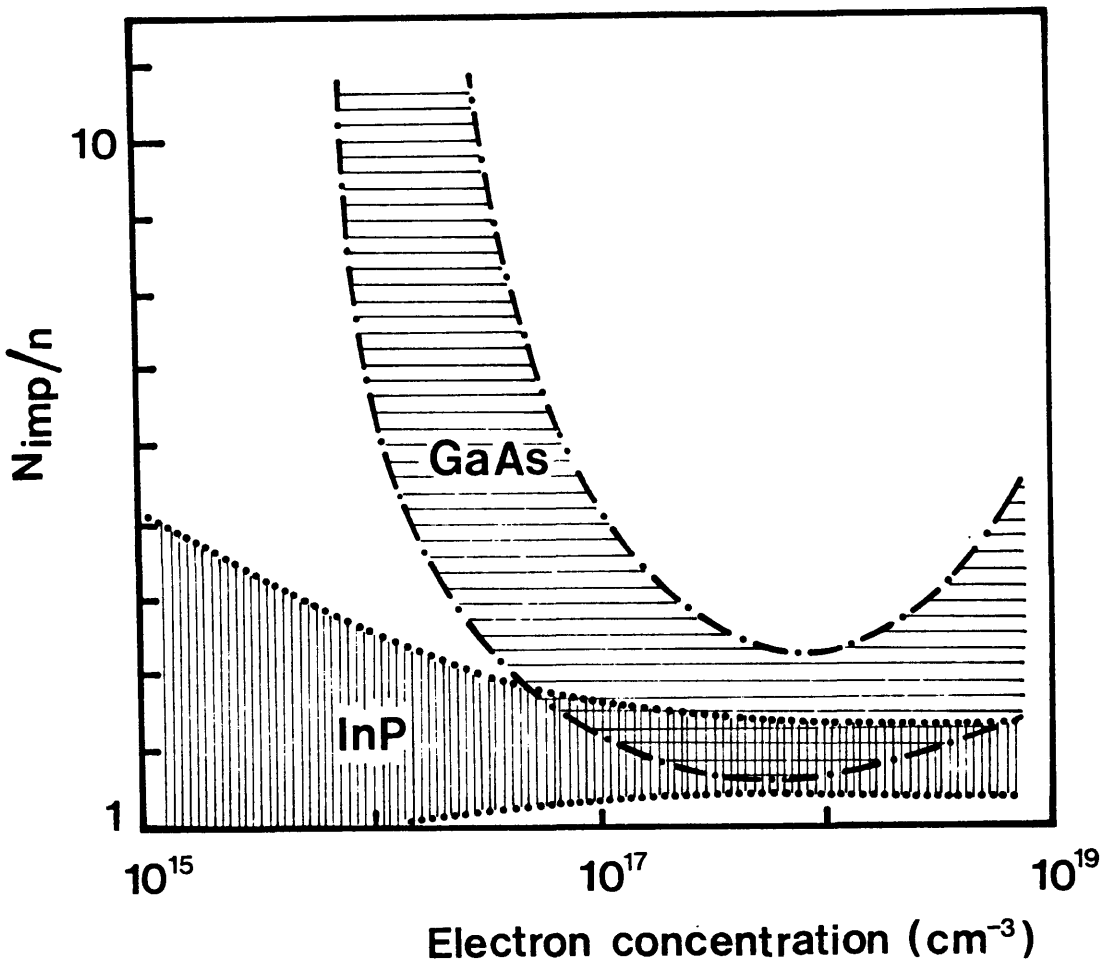
10
1
N_{imp}/n
GaAs
InP
10^{15}
10^{17}
10^{19}
Electron concentration (cm^{-3})

Fig. 8.5

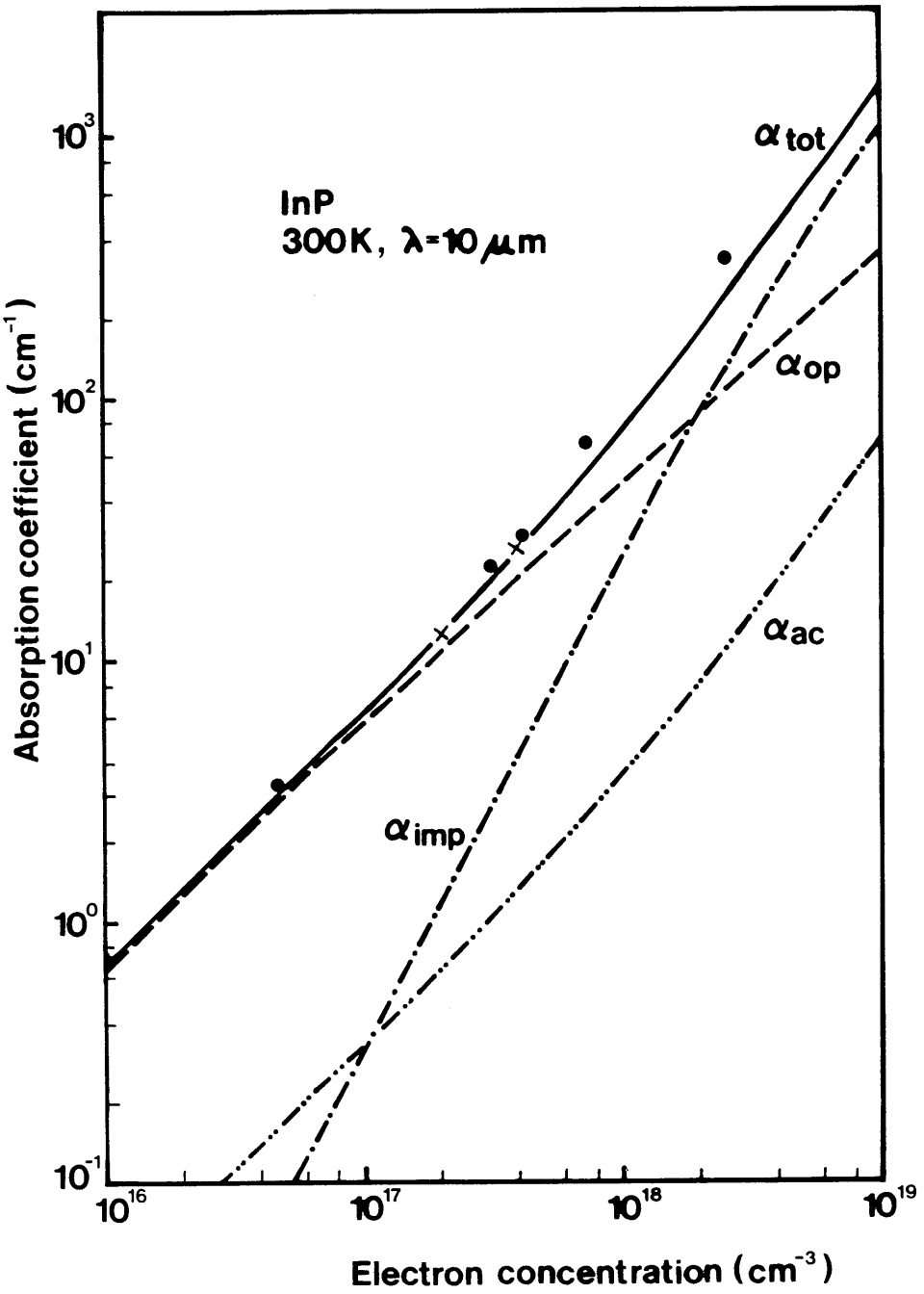
InP
300K, λ=10μm
α_{tot}
α_{op}
α_{ac}
α_{imp}
Absorption coefficient (cm^{-1})
10^{3}
10^{2}
10^{1}
10^{0}
10^{-1}
10^{16}
10^{17}
10^{18}
10^{19}
Electron concentration (cm^{-3})

Fig. 8.6

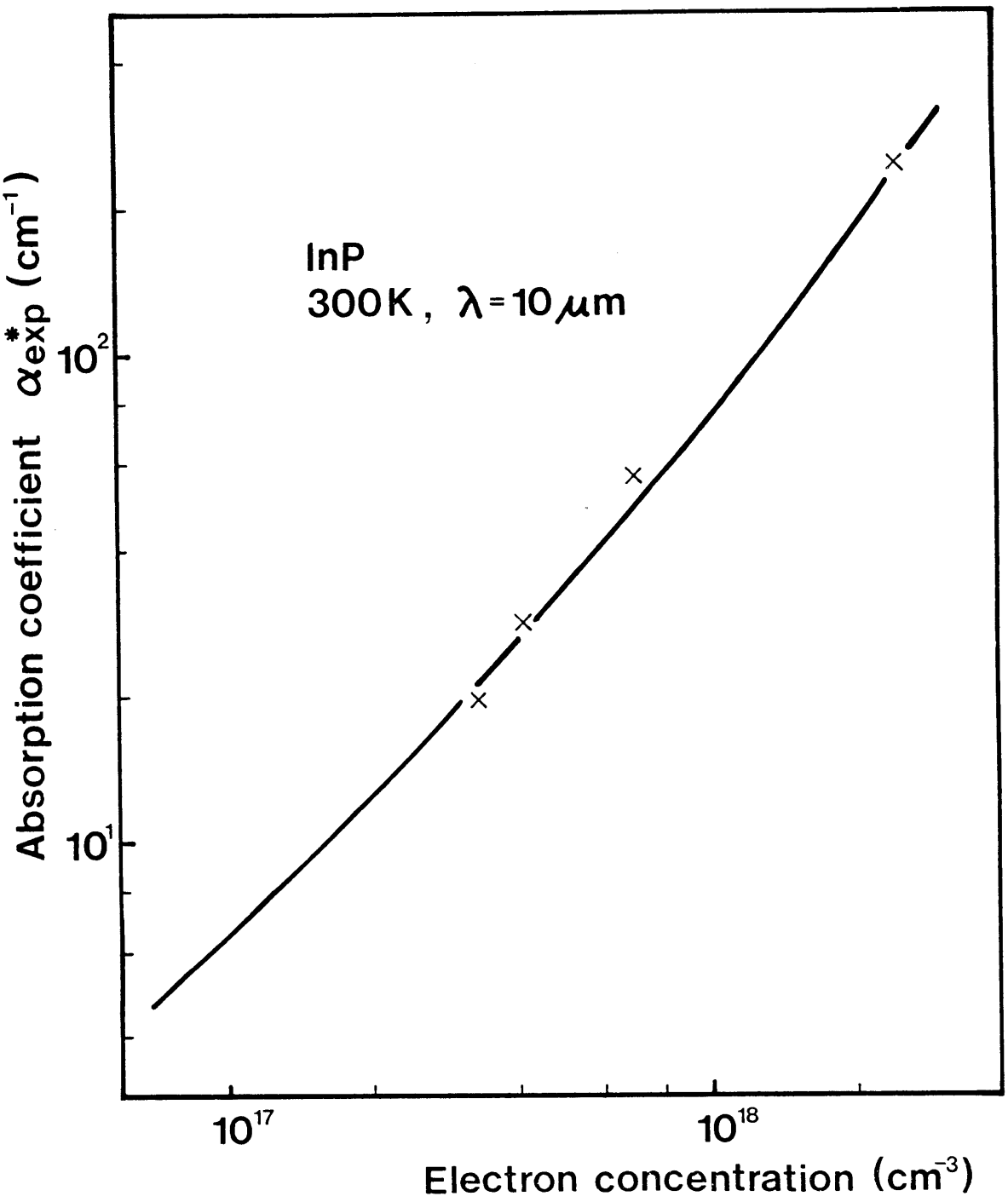
InP
300K, λ=10μm
Absorption coefficient α^*_{exp} (cm^{-1})
10^2
10^1
10^{17}
10^{18}
Electron concentration (cm^{-3})

Fig. 8.7

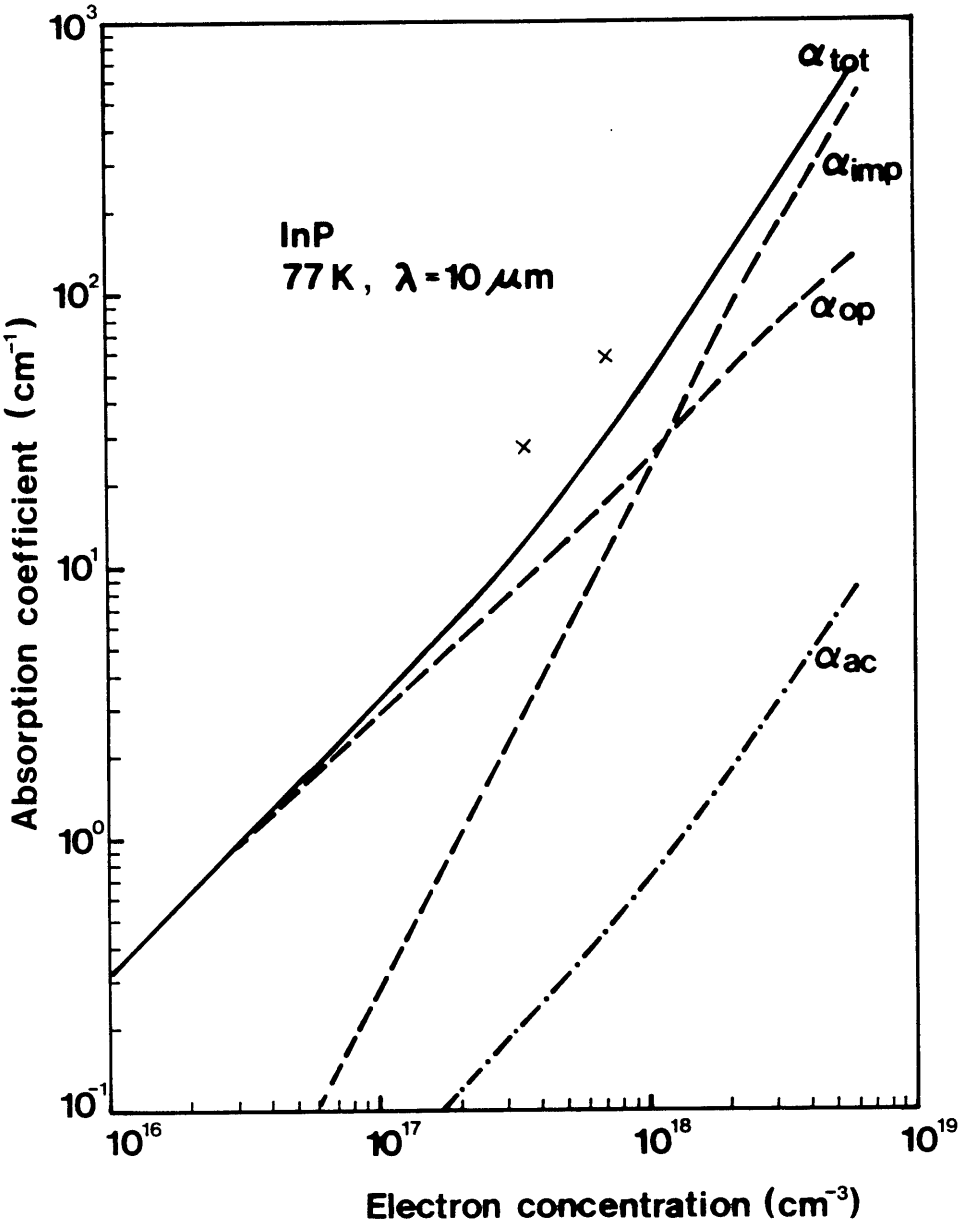
InP
77 K, λ = 10 μm
α_{tot}
α_{imp}
α_{op}
α_{ac}
Absorption coefficient (cm^{-1})
Electron concentration (cm^{-3})
10^{3}
10^{2}
10^{1}
10^{0}
10^{-1}
10^{16}
10^{17}
10^{18}
10^{19}

Fig. 8.8

IX. EFFECT OF INHOMOGENEITIES ON ELECTRICAL AND OPTICAL PROPERTIES OF InP AND GaAs

IX.1 Carrier concentration microprofiles

The effect of carrier density inhomogeneities in GaAs and InP samples on electrical and optical macroscopic measurements was studied. It was established that presence of inhomogeneities in the samples can lead to a significant ambiguity in the determination of mobility and carrier concentration from Hall measurements as well as the value of absorption coefficient and its spectral dependence from infrared transmission measurements. It was reported previously that inhomogeneities in samples can lead to anomalous values of electron mobility (79,90,91) or absorption coefficient (53).

Carrier density microprofiles in InP and GaAs samples were determined with the IR laser scanning technique discussed in Section III and used to determine oxygen concentration microprofiles in silicon. In fact, as discussed in Section VIII, free carrier absorption is present in InP and GaAs in the wavelength range covered by the CO_2 laser (9.174 μm - 10.94 μm). The same experimental apparatus shown in Fig. 3.9 was used. For free carrier concentrations $n \gtrsim 2 \times 10^{17}$ cm^{-3} interference due to multireflections is negligible and this technique can be applied to samples without antireflection coating. In fact, for such carrier concentrations $\alpha_t > 10$ cm^{-1} (Fig. 8.6) so that the condition $\alpha z >> 1$ can be attained with sample thicknesses of a few millimeters. The absence of interference effects was checked by repeating the measurements for a few different wavelengths.

The electron concentration microprofiles were determined from absorption coefficient microprofiles using the theoretical values of the free

carrier absorption coefficient in Table 8.3 for InP and in a corresponding table in ref. 53 for GaAs. A series of parallel free carrier microprofiles taken on the same melt grown InP crystal with a spatial resolution of about 30 μm at various distances from the edge of the sample are shown in Fig. 9.1. It is seen that a striation pattern can be clearly identified and that local changes in electron concentration are as high as ± 30% from the average value. Similar large fluctuations of carrier concentration were found in about 20% of the melt grown InP crystals obtained from various sources. A similar map of carrier concentration microprofiles for GaAs is shown in Fig. 9.2. It is seen that the pattern of inhomogeneity is quite similar to the one observed for InP and it is typical for most samples considered in this section.

For very large carrier concentrations the absorption coefficient is very large and the intensity of the transmitted signal becomes too low to be detected. In this case carrier concentration profiles can be obtained with reduced resolution using a larger pinhole in front of the detector. A map of free carrier concentration profiles obtained with a resolution of 500 μm on a GaAs sample ($n \cong 3 \times 10^{18}$ cm^{-3}) is shown in Fig. 9.3. The position of the striations with respect to the crystal topology is identified in the upper part of Fig. 9.3.

Free carrier concentration microprofiles obtained with the IR laser scanning technique were compared with microprofiles obtained with a completely independent technique, cathodoluminescence. The luminescence intensity emitted by a GaAs sample excited by an electron beam is inversely proportional to the electron concentration for concentrations

$\geq 2 \times 10^{18}$ cm^{-3}. A high resolution cathodoluminesce profile was obtained by Dr. John Vaughan using the Scanning Electron Microscope of the Electronic Materials Group at MIT and is shown in Fig. 9.4. A free carrier concentration profile obtained by the laser IR scanning technique with a resolution of 500 μm is also shown in Fig. 9.4. It is seen that a good correspondence exists between the two techniques, confirming their validity.

IX.2 Effect of inhomogeneities on transport properties

To study the effect of inhomogeneities on transport properties, Hall measurements in magnetic field up to 140 kG were performed. Dependence of the Hall factor r (defined as $r = R_H en$ where R_H is the Hall constant, n is the carrier concentration and e is the electronic charge) on magnetic field for three InP and one GaAs inhomogeneous samples is presented in Fig. 9.5. For comparison the dependence of r on magnetic field in a typical homogeneous sample ($n = 5.9 \times 10^{14}$ cm^{-3}) is presented in Fig. 9.5 by the upper solid line (79). In the inhomogeneous samples considered, r(H) exhibits anomolous behavior with the values of r lower than the high magnetic field limit ($r \to 1$), which cannot happen for homogeneous samples with this concentration and in this temperature range.

The presented measurements of the Hall factor in the inhomogeneous samples are in very good agreement with the theoretically predicted dependence of r on magnetic field for inhomogeneous samples (79,90,91). It has therefore been verified that samples of proven inhomogeneity have an anomalous dependence of r on magnetic field.

IX.3 Effect of inhomogeneities on optical properties

To establish the effect of inhomogeneities on the optical properties the value of the absorption coefficient and its spectral dependence was

measured for the samples investigated. The absorption coefficient was obtained from transmission measurements performed with a Fourier spectrometer in the spectral range 2.5 - 25 μm. The value of the absorption coefficient at a wavelength of 10 μm as a function of average carrier concentration is presented in Figs. 9.6a and 9.6b for GaAs and InP samples respectively. The four samples previously discussed are shown, as well as other GaAs samples of proven inhomogeneity. The solid lines in Figs. 9.6a and 9.6b are the lowest limit of the absorption coefficient for non-compensated homogeneous samples as a function of carrier concentration respectively for GaAs (53) and InP (Fig. 8.6). It can be seen that in most instances the values of absorption coefficient for compensated inhomogeneous samples are below the theoretical absorption limit, which was already previously suggested (53).

The presence of inhomogeneities in the sample results not only in an anomalous value of absorption coefficient but also in its anomalous spectral dependence, as shown in Fig. 9.7 for the GaAs sample (a) previously discussed and another sample (a') with a similar average carrier concentration. In fact, the slope for the sample (a') with lower values of absorption coefficient is higher than the slope for sample (a) with higher values of absorption coefficient. It is evident that this type of behavior cannot be expected for two homogeneous samples with the same carrier concentration; in fact, for two such samples absolute values of absorption coefficient can be higher only when the compensation ratio in the sample is higher, but the higher compensation ratio will also give a higher slope in the spectral dependence. Anomalous values of absorption coefficient and its anomalous spectral dependence can be explained by the presence of inhomogeneities in the samples.

In the theoretical model of absorption measured in an inhomogeneous sample of thickness z, transmission measured through the sample with different areas ΔS_i and absorption coefficients $\alpha + \Delta\alpha_i$ will be considered. In the case when multireflections could be neglected, transmission T, using eq. 3.2, will be given by:

$$T = (1 - R)^2 \frac{e^{-\alpha z}}{S} \sum_i \Delta S_i \, e^{-\Delta\alpha_i z} \tag{9.1}$$

where $S = \sum_i \Delta S_i$ is the total area of the sample and R is the reflection coefficient. The absorption coefficient α_{exp} determined from transmission will be:

$$\alpha_{exp} \cong \alpha - \frac{1}{z} \ell n \left(\sum_i \frac{\Delta S_i}{S} e^{-\Delta\alpha_i z} \right) \tag{9.2}$$

Equation 9.2 shows that in an inhomogeneous sample the measured absorption coefficient could be below the average value of the absorption coefficient and the discrepancy from the average value will depend on the areas and magnitudes of the inhomogeneities ΔS_i, $\Delta\alpha_i$ and z. According to eq. 9.2 the regions of minimum absorption are weighted more heavily in the measurement of the absorption coefficient, which therefore in most cases is below the average value.

For the simplified case of an inhomogeneous sample composed of two different areas ΔS_1 and $\Delta S_2 = S - \Delta S_1$ with absorption coefficients respectively $\alpha + \Delta\alpha$ and $\alpha - \Delta\alpha$, eq. 9.2 reduces to:

$$\alpha_{exp} = \alpha - \frac{1}{z} \ell n \left[\frac{\Delta S_1}{S} e^{-\Delta\alpha z} + \left(1 - \frac{\Delta S_1}{S}\right) e^{\Delta\alpha z} \right] \tag{9.3}$$

The spectral dependence of α is determined by the scattering mechanism and is given by (from eq. 8.2):

$$(\alpha + \Delta\alpha) = (C + \Delta C)\left(\frac{\lambda}{\lambda_o}\right)^n \qquad (9.4)$$

where n can go from 2.5 for optical phonon scattering to 3.5 for impurity scattering. The spectral dependence of α_{exp} can be calculated substituting eq. 9.4 into eq. 9.3 for the two limit cases of n = 2.5 and n = 3.5. Results of the calculations for two different sets of values of the parameters are shown in Fig. 9.8. The presence of an inhomogeneity in the sample changes the value of the slope from n = 2.5 and n = 3.5 for a homogeneous sample to n = 1.8 and n = 3.1 for an inhomogeneous sample ($\Delta S_1/S = 0.25$) for optical phonon scattering and impurity scattering respectively. Therefore according to Fig. 9.8 the results presented in Fig. 9.7 can be explained by the presence of different areas and magnitudes of inhomogeneity in the two measured samples.

IX.4 Conclusions

It can be concluded that carrier concentration inhomogeneities in the measured samples will influence Hall as well as infrared absorption measurements producing serious ambiguity in the determination of the Hall constant, carrier concentration, mobility, value of absorption coefficient and its spectral dependence. These parameters are essential for any analysis of physical phenomena taking place in semiconductors, therefore selection of homogeneous samples prior to measurements is essential for their accurate determination. The presence of inhomogeneities in the samples can be disclosed by comparison with theoretical predictions of measurements of the magnetic field dependence of the Hall

constant and of the value and spectral dependence of the absorption coefficient, as well as by direct measurement of the free carrier micro-profiles by IR laser scanning absorption.

Figure Captions

Fig. 9.1 Typical electron concentration microprofiles of InP obtained with scanning IR absorption.

Fig. 9.2 Typical electron concentration microprofiles of GaAs obtained with scanning IR absorption.

Fig. 9.3 Typical electron concentration profiles of a GaAs sample with large carrier concentration obtained with scanning IR absorption with a resolution of 500 μm.

Fig. 9.4 Electron concentration profile of GaAs obtained with scanning IR absorption with a resolution of 500 μm; catholuminescence intensity along the same location.

Fig. 9.5 Hall constant dependence on magnetic field for inhomogeneous samples.

S-1 o : InP $n_{av} = 1.8 \times 10^{16}$ cm^{-3}

S-2 Δ : InP $n_{av} = 8.5 \times 10^{16}$ cm^{-3}

S-3 ▲ : InP $n_{av} = 8 \times 10^{17}$ cm^{-3}

(a) ● : GaAs $n_{av} = 1.9 \times 10^{18}$ cm^{-3}

The solid line in the upper part of the figure gives the dependence of the Hall constant on magnetic field for a homogeneous sample (82).

Fig. 9.6 (a) Free carrier absorption coefficient $\alpha_{10\ \mu m}$ as a function of electron concentration n for GaAs. The dot corresponds to the sample (a) of Fig. 9.5; the squares correspond to other samples of proven inhomogeneity. The solid line gives the theoretical dependence of the absorption coefficient on the electron concentration (53).

(b) Free carrier absorption coefficient $\alpha_{10\ \mu m}$ as a function of electron concentration n for InP. The samples S-1, S-2 and S-3 of Fig. 9.5 are shown. The solid line gives the theoretical dependence of the absorption coefficient on the electron concentration (Fig. 8.6).

Fig. 9.7 Absorption coefficient α as a function of wavelength λ for the GaAs sample (a) of Fig. 9.5 and for another GaAs sample (a') of similar average carrier concentration. The slope for sample (a) is 3.1, for sample (a') 3.5.

Fig. 9.8 Theoretical spectral dependence of the absorption coefficient for samples of different inhomogeneity. The two lower curves have parameters $z = 5 \times 10^{-2}$ cm, $\lambda_o = 10$ μm, $C = 30$ cm^{-1}, $\Delta C = 25$ cm^{-1}, $n = 2.5$ and respectively $(\Delta S_1/S) = 0$ for the lower one and $(\Delta S_1/S) = 0.25$ for the higher one. The two

upper curves have parameters $z = 5 \times 10^{-2}$ cm, $\lambda_o = 10$ μm, $C = 70$ cm^{-1}, $\Delta C = 40$ cm^{-1}, $n = 3.5$ and respectively $(\Delta S_1/S) = 0$ for the lower one and $(\Delta S_1/S) = 0.25$ for the higher one.

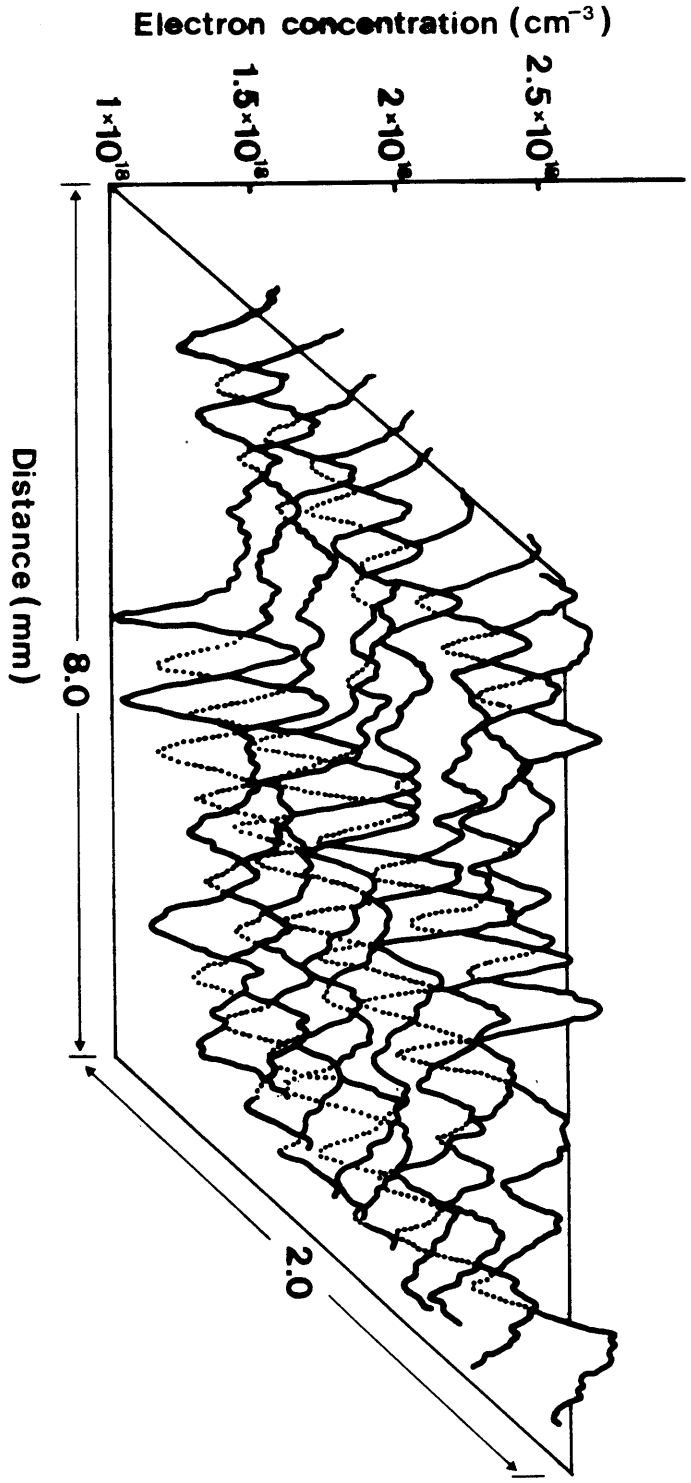
Electron concentration (cm^{-3})
1×10^{18}
1.5×10^{18}
2×10^{18}
2.5×10^{18}
Distance (mm)
8.0
2.0

Fig. 9.1

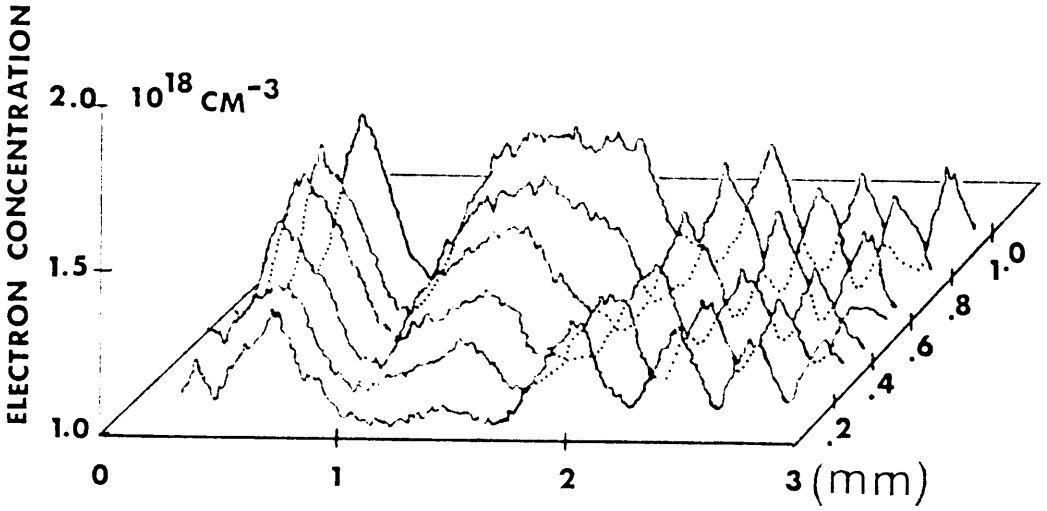

Fig. 9.2

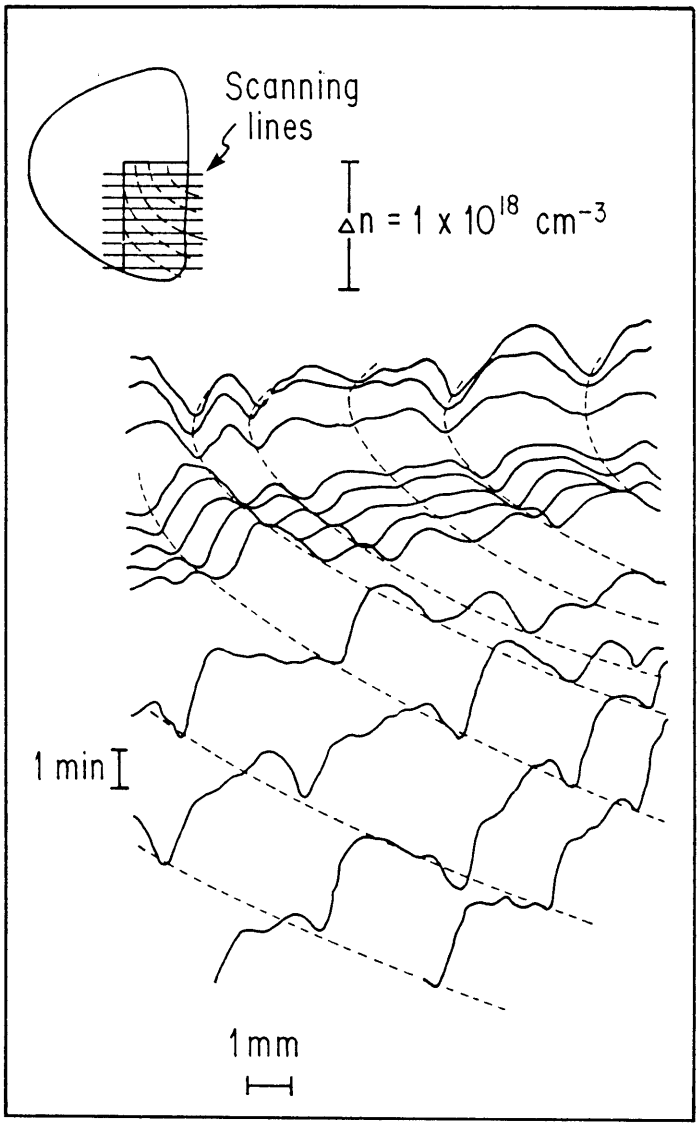

Fig. 9.3

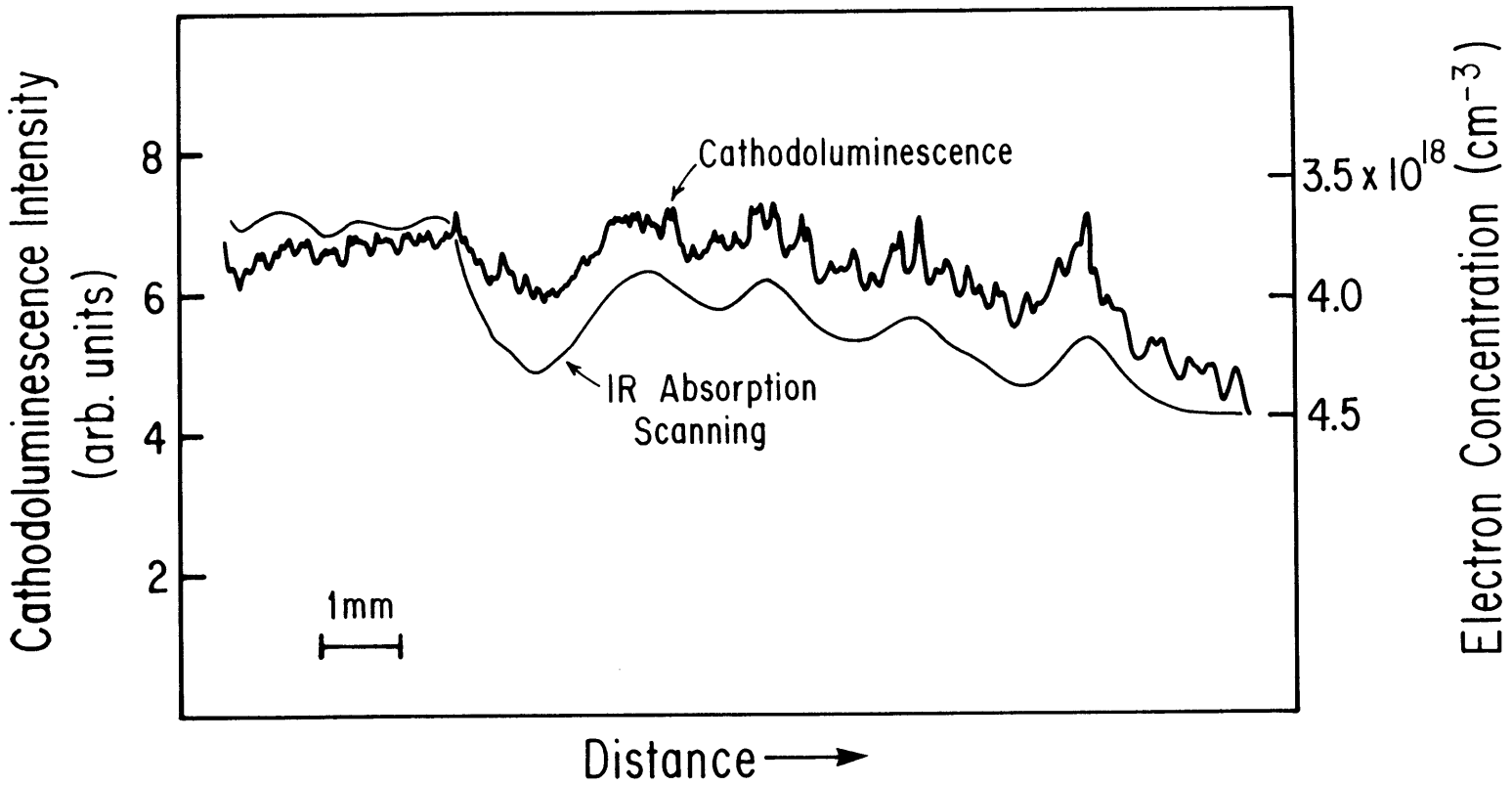
Cathodoluminescence Intensity
(arb. units)
8
6
4
2
Cathodoluminescence
IR Absorption
Scanning
1mm
Distance
3.5 x 10^18
4.0
4.5
Electron Concentration (cm^-3)

Fig. 9.4

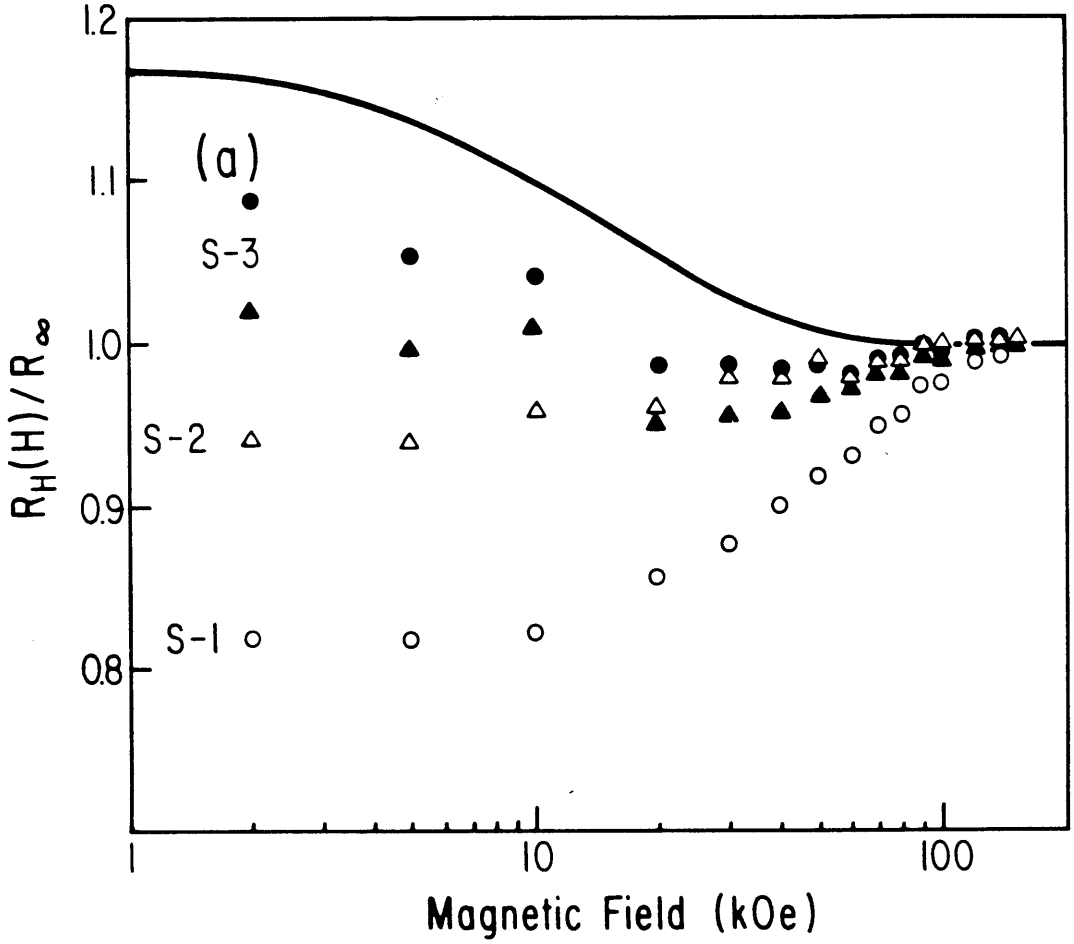

Fig. 9.5

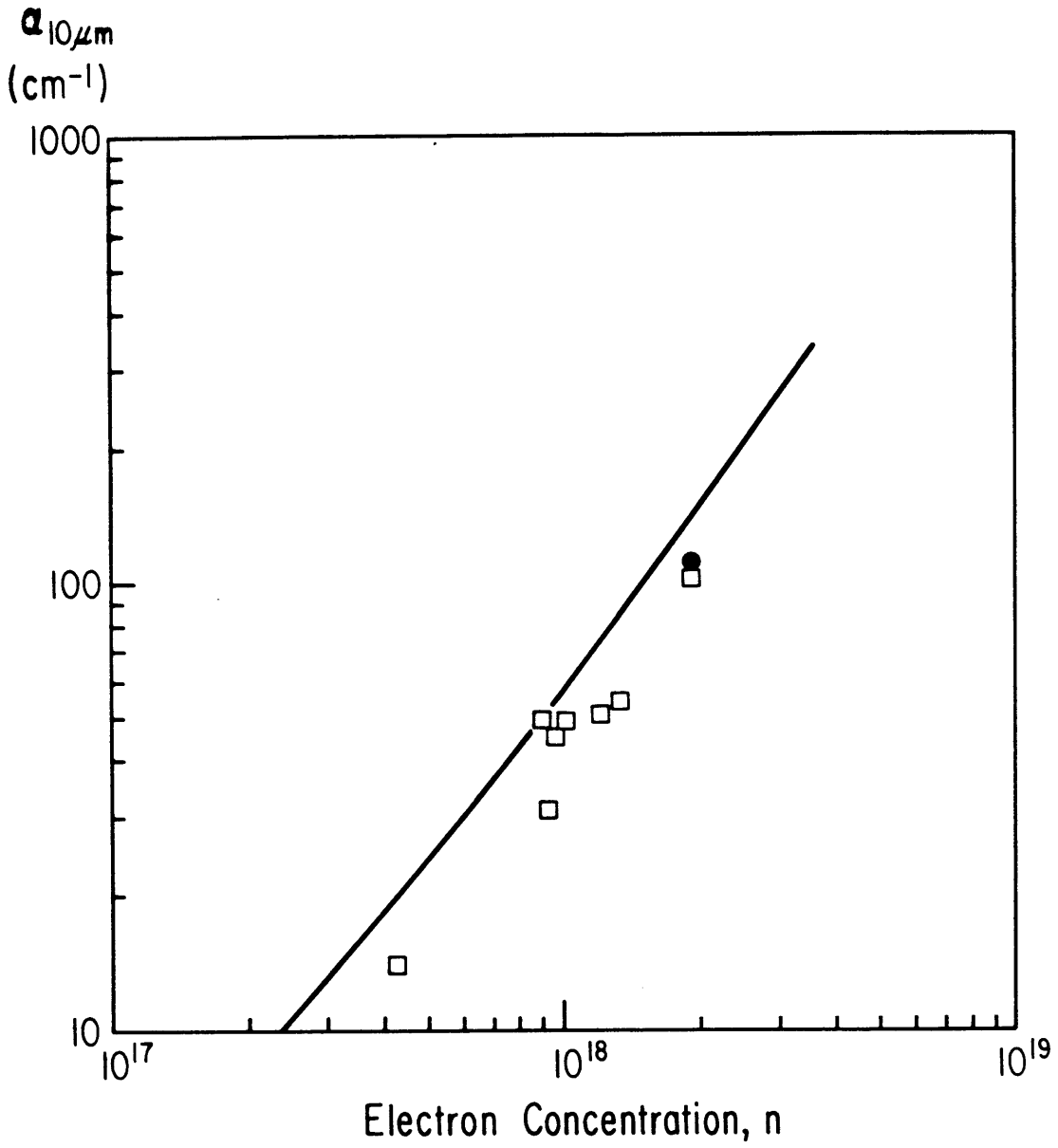
$\alpha_{10\mu m}$
(cm^{-1})
1000
100
10
10^{17}
10^{18}
10^{19}
Electron Concentration, n

Fig. 9.6a

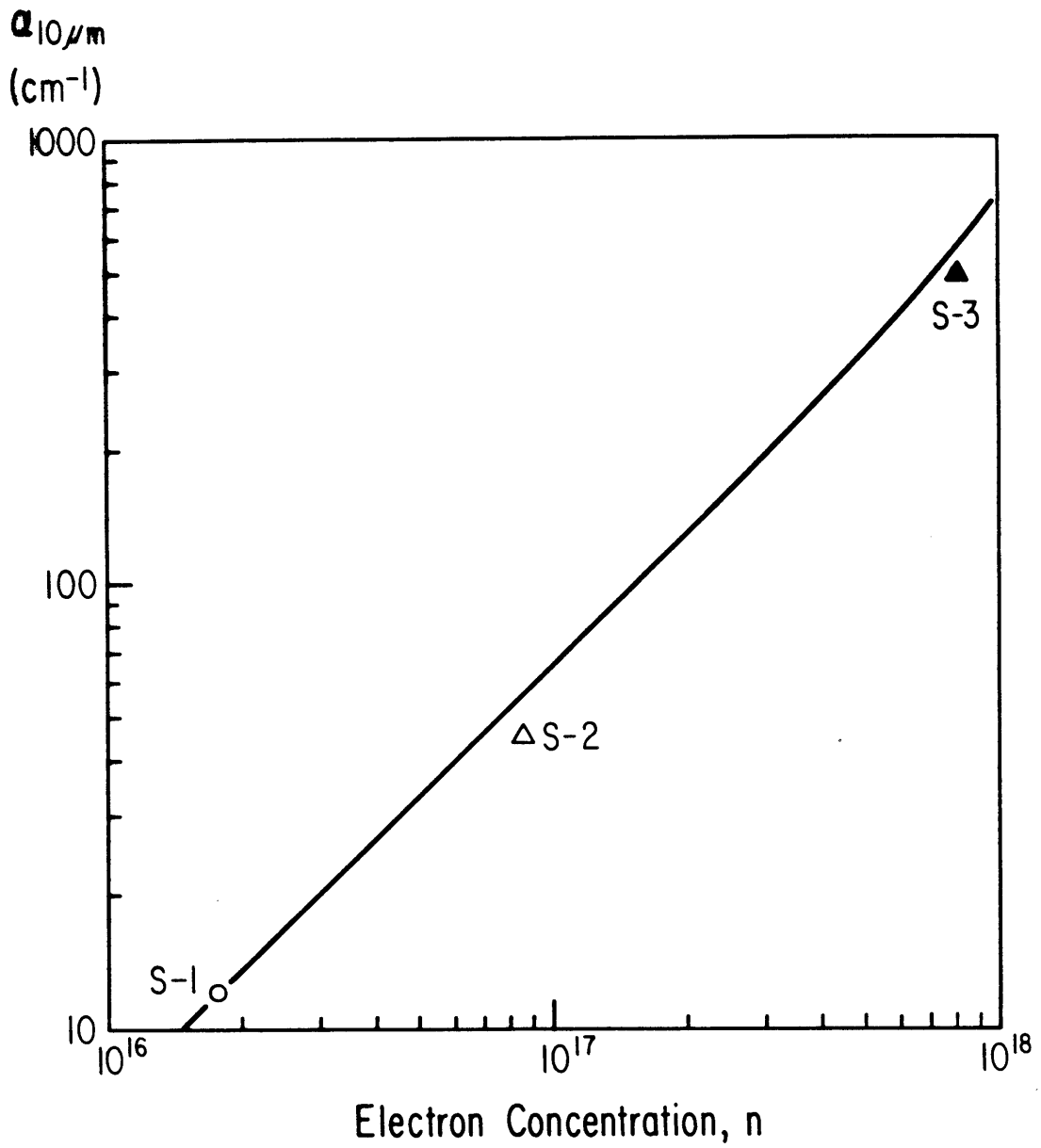
$\alpha_{10\mu m}$
(cm^{-1})
1000
100
10
S-1
S-2
S-3
10^{16}
10^{17}
10^{18}
Electron Concentration, n

Fig. 9.6b

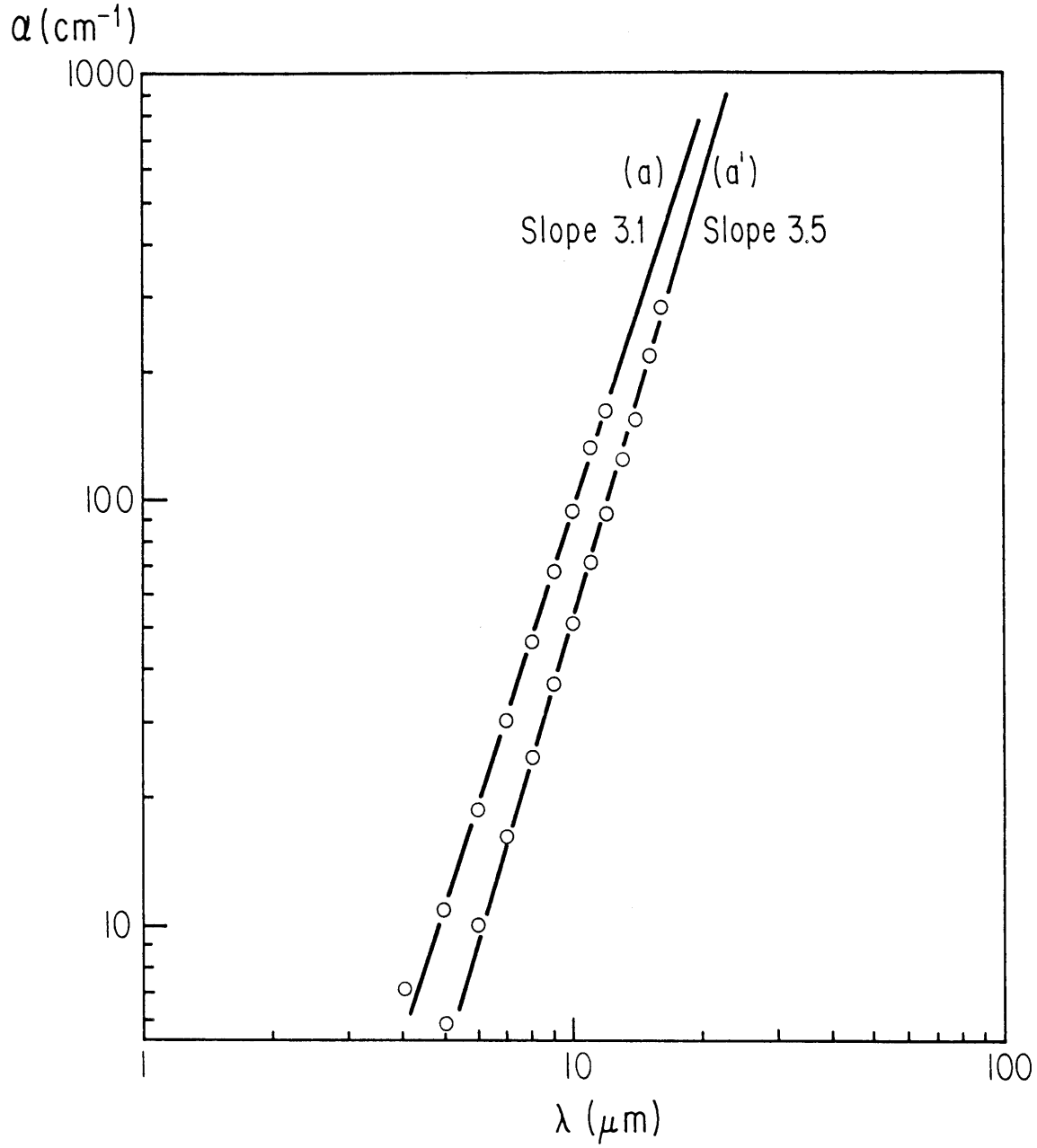

Fig. 9.7

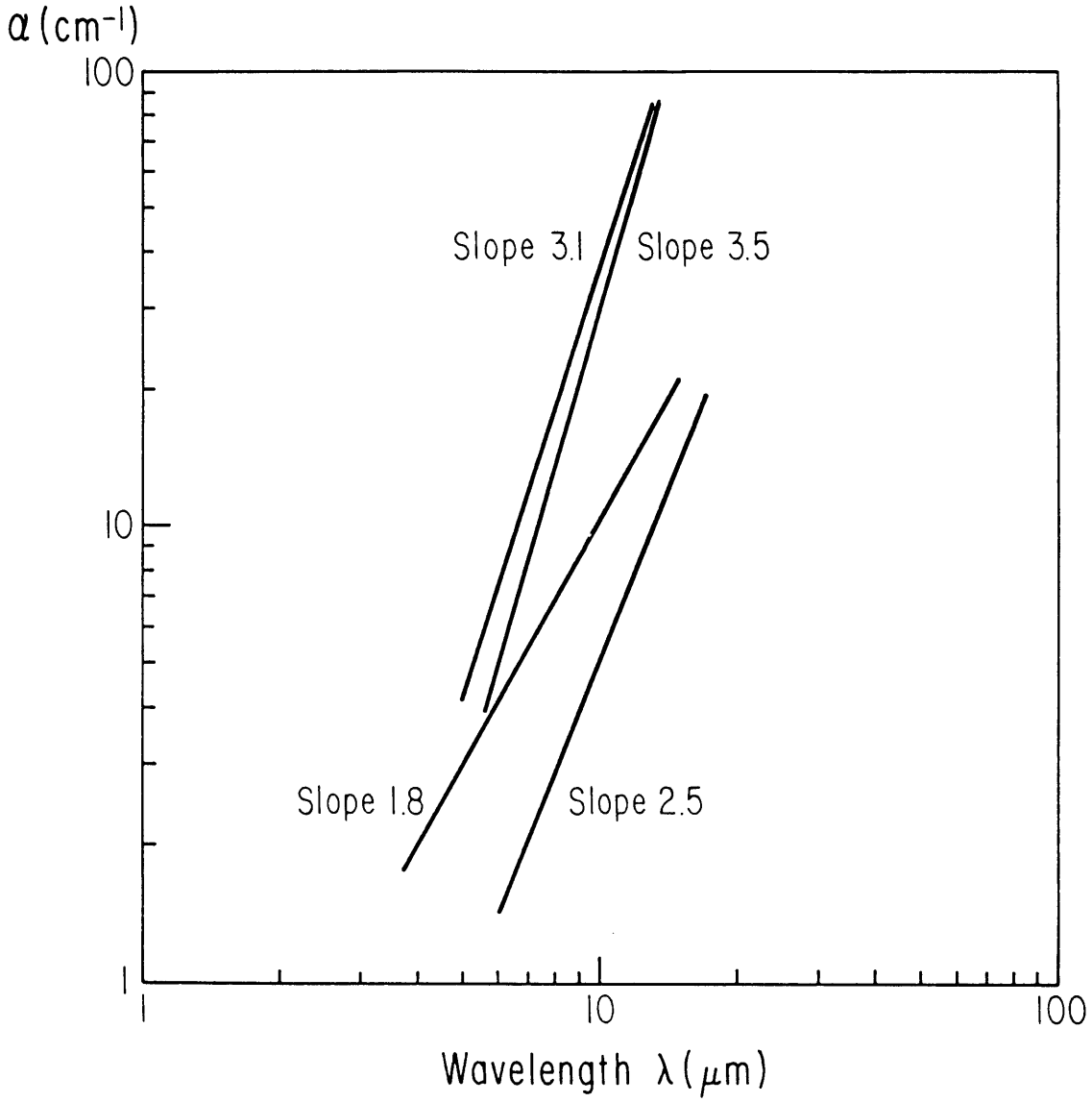
α (cm⁻¹)
100
10
1
Slope 3.1
Slope 3.5
Slope 1.8
Slope 2.5
1
10
100
Wavelength λ (μm)

Fig. 9.8

X. SUMMARY

In the present work for the first time the axial microdistribution of oxygen in silicon was measured with a resolution of 30 μm using an IR laser scanning absorption technique. To avoid interference arising from multireflections, an antireflection coating was applied to the samples. Typically, variations in the oxygen concentration were about 30% of the average value.

The samples (B-doped) were then heat treated at 450°C for 4 hours to activate thermal donors. Thermal donor concentration microprofiles were measured with the spreading resistance technique along the same locations of the oxygen microprofiles. As an average, the donor concentration was about three orders of magnitude smaller than the oxygen concentration. A comparison of the thermal donor and of the oxygen microprofiles showed that, although there is a correspondence in the overall features of the two profiles, in some locations there is no direct correspondence between oxygen and activated donor concentrations. In particular, in large regions near the periphery of the crystal, no thermal donors were formed.

The samples were then heat treated at 650°C for 4 hours and all the donors were annihilated. Upon further heat treatment at 450°C thermal donors were activated in previously unactivated regions, whereas activation occurred at a reduced level in previously activated regions. Further heat treatments at 450°C increased the activated donor concentration in all regions and further heat treatments at 650°C caused annihilation of donors. After long heat treatment cycles the activated donor concentration was greatly reduced.

The microdefect distribution was studied for B-doped Si as a function of heat treatment time using a defect revealing etchant. Large densities of B-defects were found in regions which presented no activation upon the first heat treatment at 450°C; A-defects, of larger size than B-defects, were present in activated regions. Upon heat treatment at 650°C for 4 hours the B-defects increased in size, tending to become A-defects and allowing activation to take place upon further heat treatment at 450°C.

The influence of the acceptor dopants on the activation rate was investigated. The activation rate was larger for Ga-doped Si than for B-doped Si; for both dopants, it was proportional to the fourth power of the oxygen concentration on the average; points close to the periphery presented a reduced activation. The activation rate for In-doped silicon was proportional roughly to the square of the oxygen concentration; no deviation from this proportionality was observed near the periphery.

The microdefect distribution in Ga-doped silicon had a behavior similar to B-doped silicon. On the other hand, a very low density of B-defects was present in all regions of In-doped silicon for all heat treatment times.

These results were interpreted in the light of the oxygen-vacancy complex model. An interstitial oxygen becomes substitutional when it slips into a silicon vacancy. The substitutional oxygen is stabilized by complexing with another vacancy or an acceptor atom; its extra electron can then be ionized, creating a donor. Further complexing with a third vacancy or an acceptor annihilates the donor. At 450°C, vacancies have diffusivities large enough to allow donor generation; at 650°C the neutral three vacancies-oxygen complexes are predominant. In regions where

B-defects are present, vacancies are not available for donor formation; in fact, B-defects act as vacancy getters. Upon heat treatment at 650°C vacancies are released from B-defects and can take part in donor activation upon further heat treatment at 450°C.

Concentrations of vacancies of the right order of magnitude to account for donor activation are present in silicon crystals. Large concentrations of impurities can increase the vacancy concentration; In-doped crystals have large concentrations of available vacancies in all regions of the crystal due to a large concentration of In

The vacancy-oxygen complex model was shown to be compatible with a model which explains donor activation with SiO_4 complexes. The formation of a substitutional oxygen by vacancy-oxygen complexing is considered the first step in the formation of SiO_2, SiO_3, SiO_4 complexes; all these donor complexes can be present simultaneously. The essential role of vacancies in donor activation could be disclosed only by a microscale analysis such as the one presented here. Previous macroscale measurements had failed to individuate unambiguously the presence of another species active in donor activation.

An application of thermal donor activation to a multijunction structure was then investigated. Axially cut p-type silicon was heat treated at 450°C to generate overcompensation to n-type in correspondence of the thermal donor maxima; an alternate p-n junction structure resulted. Solar cells were built using this structure and were tested. An increase in short circuit current with respect to a conventional structure was achieved; but at the same time, a degradation in open circuit voltage occurred, so that no net improvement in conversion efficiency resulted.

These results were interpreted with the aid of a computer simulation. It was shown that a net increase in efficiency could be achieved using a structure with spacing between junctions smaller than the diffusion length.

A microscale analysis was then used to investigate the influence of carrier density inhomogeneities on the electrical and optical properties of InP and GaAs. First, macroscale measurements were made of the electron mobility, electron concentration and free carrier absorption coefficient in InP. A procedure, which had already been proposed for GaAs, was then used to obtain the compensation ratio comparing the experimentally obtained values of electron mobility and free carrier absorption coefficient with theoretical values. Both these quantities are partly dependent on ionized impurity scattering, so that the concentration of impurities can be determined from their measurement. Good agreement between the two independently determined values of electron mobility was found for most samples. For a few samples, the procedure was not applicable because the values of the absorption coefficient was anomalously low.

The homogeneity of all the samples was assessed by measurements of the free carrier concentration microprofiles. The same IR laser scanning absorption technique used in the first part of this study was used to determine carrier concentration microprofiles in InP and GaAs. In about 20% of the samples used, local changes in electron concentration were as high as $\pm 30\%$ from the average value. Measurements of the Hall constant as a function of magnetic field showed an anomalous dependence for inhomogeneous samples. These results were found in agreement with the predictions of a model of an inhomogeneous sample. The free carrier absorption coefficient was then measured on a macroscale as a function of wavelength.

Inhomogeneous samples had anomalously low values of absorption coefficient and an anomalous spectral dependence. These results were interpreted in the light of a model for absorption in an inhomogeneous sample.

The ambiguities arising from inhomogeneities do not allow application of the procedure to determine the compensation ratio discussed above to inhomogeneous samples. A microscale analysis was proven necessary to resolve ambiguities in macroscale measurements both in the case of the activation of thermal donors in silicon and in the case of the determination of the compensation ratio in InP and GaAs.

Some of the results presented in this work appear in the following publications:

W. Walukiewicz, J. Lagowski, L. Jastrzebski, P. Rava, M. Lichtensteiger, C. H. Gatos and H. C. Gatos, J. Appl. Phys. 51, 2659 (1980).

P. Rava, H. C. Gatos and J. Lagowski, Appl. Phys. Lett. 38, 274 (1981).

P. Rava, H. C. Gatos and J. Lagowski, Semiconductor Silicon 1981, Electrochem. Soc., Minneapolis, 1981.

XI. SUGGESTIONS FOR FURTHER WORK

In the present work the mechanism of thermal donor activation in oxygen containing silicon has been clarified, the potential for improved efficiency of a new solar cell structure has been demonstrated and the influence of inhomogeneities on macroscopic electrical and optical properties of III-V compounds has been shown. Work remains to be done in each of the following areas.

Regarding the properties of oxygen in silicon, a lot of attention has been focused lately on spectroscopic investigations of the thermal donor levels (37-39). Results reported in the literature can be interpreted to support the model presented in this work. But a complete investigation of the behavior of the thermal donor levels as a function of heat treatment times and for different dopants is still lacking. Such an investigation should include both deep levels and shallow levels. Infrared transmissivity measurements at low temperatures in the range 5-50 μm would allow determination of both shallow and deep levels. In addition, Deep Level Transient Spectroscopy measurements would allow determination of deep levels. These two techniques are commonly employed on a macroscale and their use in a comprehensive investigation would shed more light on the nature of the thermal donor. Extremely important for this purpose would also be their extension to microscale and the correlation of the thermal donor level microprofiles so obtained with oxygen concentration microprofiles obtained with the technique described in the present investigation.

Work remains to be done on the correlation between oxygen concentration and some properties relevant to photovoltaic energy conversion, like lifetime and diffusion length. Lifetime profiles can be determined using

the free carrier absorption scanning technique to measure the excess carriers excited by a light source. A laser with a wavelength appropriate to excite carriers can be used in conjunction with the experimental apparatus used in the present work (Fig. 3.9). The lifetime profiles can then be correlated with oxygen profiles obtained along the same line.

Further developments of the new solar cell structure described in Section VII require obtaining closely spaced and regular junctions, hence oxygen striations. Therefore crystal growth techniques aimed at obtaining regular oxygen striations of controllable width must be developed. This involves eliminating the effects of uncontrolled turbulent convection, which is predominant in most cases for oxygen in silicon. Turbulent convection could be eliminated by Czochralski growth under forced convection conditions or in transverse magnetic fields. Under such conditions, the oxygen impurity would be microscopic growth rate controlled. Regular oxygen striations could then be introduced by thermal cycling, rotating and pulling the crystal regularly. The striation spacing would be determined by the rotation and pulling rate. The development of such crystal growth techniques requires the use of the oxygen microcharacterization techniques developed in the present investigation.

APPENDIX: Raman scattering

Raman scattering has been used as a technique to analyze impurities in silicon (92). The one phonon and the two phonon Raman lines in silicon have been identified respectively in the vicinity of 500 cm^{-1} and 1000 cm^{-1} (93, 94). There is no report in the literature of any line due to oxygen or of any influence of oxygen on the lattice lines. In order to investigate the influence of oxygen on the Raman lines, Raman scattering experiments were performed using the experimental set-up of Professor Dresselhaus' group at MIT with the cooperation of Boris Elman. Raman spectra were measured for two samples, one cut from a Czochralski-grown ingot with an oxygen content of about 10^{18} cm^{-3} and one cut from a float zone ingot with low oxygen content. The wavelength of the incident laser beam was 4881 Å. The Raman spectra for the Czochralski-grown sample and for the float zone sample are shown in Fig. A.1 and Fig. A.2 respectively. The one phonon and the two phonon lines are clearly visible and their frequencies are in good agreement with values reported in the literature; no difference can be observed between the two spectra. It can be concluded that oxygen has little or no influence on Raman spectra and that Raman scattering is not a viable technique to measure interstitial oxygen in silicon.

Figure Captions

Fig. A.1 Intensity of Raman scattered radiation as a function of wave-number. The wavelength of the incident laser beam is 4881 Å. The two phonon peak is amplified X10 in the insert. The oxygen concentration of the sample is ~10^{18} cm^{-3}.

Fig. A.2 Intensity of Raman scattered radiation as a function of wave-number. The wavelength of the incident laser beam is 4881 Å. The two phonon peak is amplified X10 in the insert. The oxygen concentration of the sample is ~10^{15} cm^{-3}.

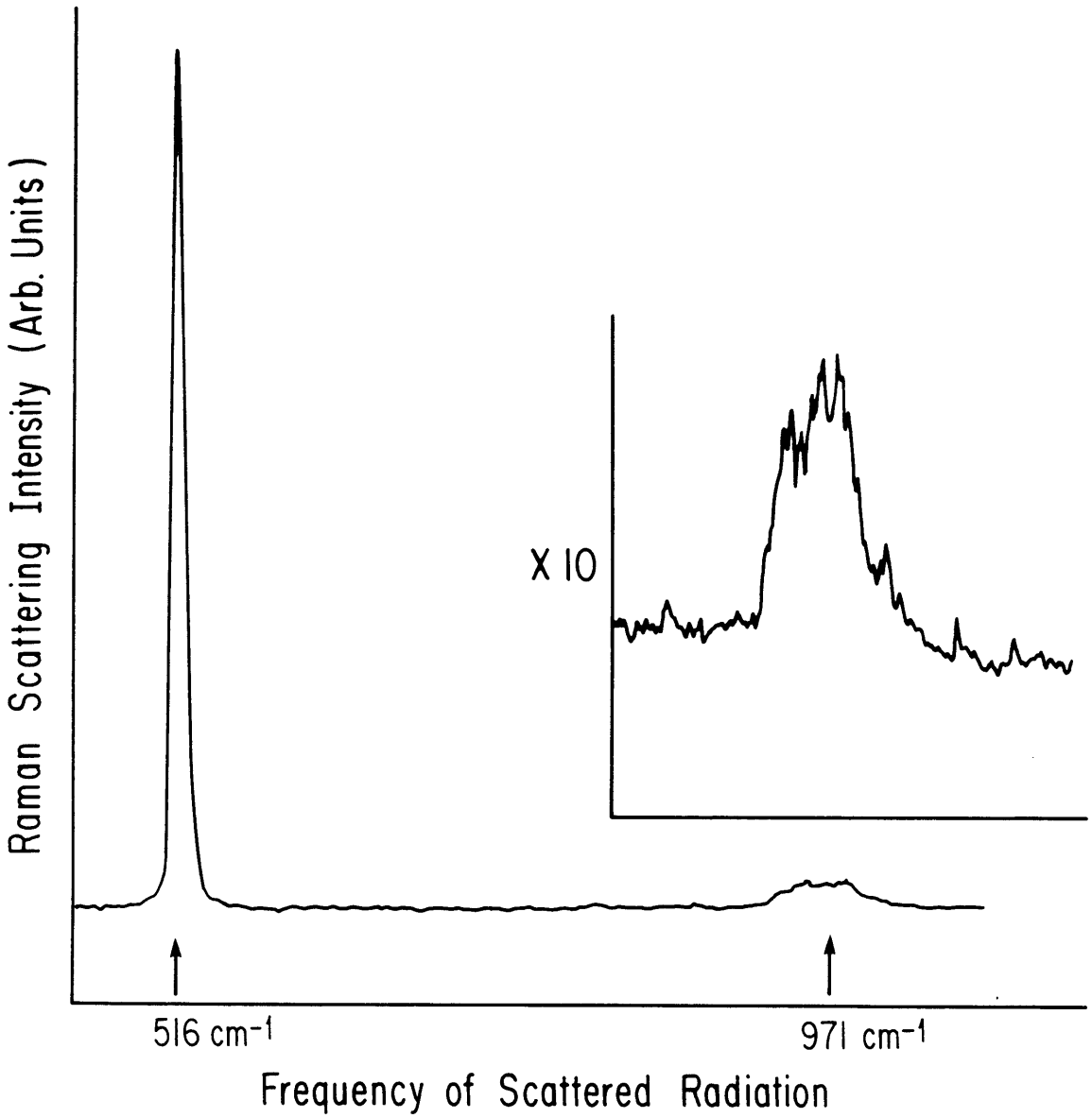
Raman Scattering Intensity (Arb. Units)
X 10
516 cm-1
971 cm-1
Frequency of Scattered Radiation

Fig. A.1

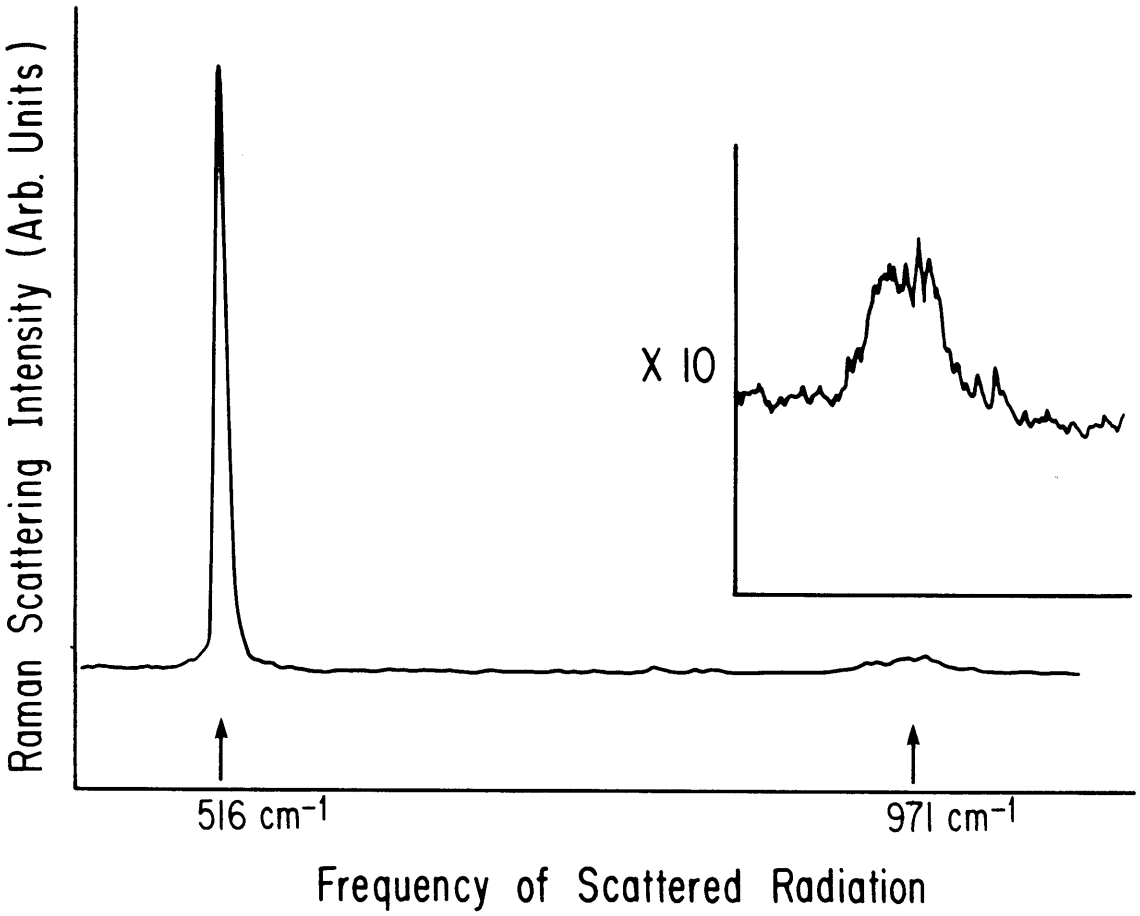
Raman Scattering Intensity (Arb. Units)
X 10
516 cm⁻¹
971 cm⁻¹
Frequency of Scattered Radiation

Fig. A.2

References

1. R. J. Collins and H. Y. Fan, Phys. Rev. 93, 674 (1954).
2. W. Kaiser, P. H. Keck and C. F. Lange, Phys. Rev. 101, 1264 (1956).
3. H. J. Hrostowski and R. H. Kaiser, Phys. Rev. 107, 966 (1957).
4. H. J. Hrostowski and B. J. Adler, J. Chem. Phys. 33, 980 (1960).
5. W. Kaiser and P. H. Keck, J. Appl. Phys. 28, 882 (1957).
6. B. Pajot, Solid State El. 12, 923 (1969).
7. J. A. Baker, Solid State El. 13, 1431 (1970).
8. K. Graff, E. Grallath, S. Ades, G. Goldbach and G. Toelg, Solid State El. 16, 887 (1973) (in German).
9. Standard test method for interstitial atomic oxygen content of silicon by infrared absorption, ASTM Standard F 121-79.
10. C. S. Fuller, J. A. Ditzenberger, N. B. Hannay and E. Buehler, Phys. Rev. 96, 833 (1954).
11. C. S. Fuller, J. A. Ditzenberger, N. B. Hannay and E. Buehler, Acta Met. 3, 97 (1956).
12. C. S. Fuller and R. A. Logan, J. Appl. Phys. 28, 1427 (1957).
13. W. Kaiser, Phys. Rev. 105, 1751 (1957).
14. W. Kaiser, H. L. Frisch and H. Reiss, Phys. Rev. 112, 1546 (1958).
15. C. Haas, J. Phys. Chem. Solids 15, 108 (1960).
16. R. A. Logan and A. J. Peters, J. Appl. Phys. 30, 1627 (1959).
17. Y. Takano and M. Maki, Semiconductor Silicon 1973, edited by H. R. Huff and R. R. Burgess, Electrochem. Soc., p. 469.
18. J. Gass, H. H. Mueller and H. Stuessi, J. Appl. Phys. 51, 2030 (1980).
19. H. J. Hrostowski and R. H. Kaiser, J. Phys. Chem. Solids 9, 214 (1959).
20. A. R. Bean and R. C. Newman, J. Phys. Chem. Solids 32, 1211 (1971).
21. A. R. Bean and R. C. Newman, J. Phys. Chem. Solids 33, 255 (1972).

22. D. Helmreich and E. Sirtl, Semiconductor Silicon 1977, edited by H. R. Huff and E. Sirtl, Electrochem. Soc., p. 626.

23. C. S. Fuller and F. H. Doleiden, J. Appl. Phys. 29, 1264 (1958).

24. C. S. Fuller, F. H. Doleiden and K. Wolfstirn, J. Phys. Chem. Solids 13, 187 (1960).

25. H. J. Hrostowski and R. H. Kaiser, J. Phys. Chem. Solids 4, 148 (1958).

26. R. C. Newman and J. B. Willis, J. Phys. Chem. Solids 26, 373 (1965).

27. R. C. Newman and R. S. Smith, J. Phys. Chem. Solids 30, 1493 (1969).

28. Standard test method for substitutional atomic carbon content of silicon by infrared absorption, ASTM Standard F 123-74.

29. J. A. Baker and T. N. Tucker, J. Appl. Phys. 39, 4365 (1968).

30. Y. Matukura, J. Phys. Soc. Jap. 14, 918 (1959).

31. K. Graff and H. Pieper, J. El. Mat. 4, 281 (1975).

32. K. Graff, K. Hilgarth and H. Neubrand, Semiconductor Silicon 1977, edited by H. R. Huff and E. Sirtl, Electrochem. Soc., p. 575.

33. J. P. Suchet, J. Chim. Phys. 58, 455 (1961) (in French).

34. F. J. Morin, J. P. Maita, R. G. Shulman and N. B. Hannay, Phys. Rev. 96, 833 (1954).

35. H. J. Hrostowski and R. H. Kaiser, Phys. Rev. Lett. 1, 199 (1958).

36. V. N. Mordkovich, Sov. Phys. Solid State 6, 654 (1964).

37. P. Gaworzewski and K. Schmalz, phys. stat. sol. (a) 55, 699 (1979).

38. D. Wruck and P. Gaworzewski, phys. stat. sol. (a) 56, 557 (1979).

39. H. Nakayama, J. Katsura, T. Nishino and Y. Hamakawa, Jap. J. Appl. Phys. 19, 547 (1980).

40. P. Capper, A. W. Jones, E. J. Wallhouse and J. G. Wilkes, J. Appl. Phys. 48, 1646 (1977).

41. A. Kanamori, Appl. Phys. Lett. 34, 287 (1979).

42. A. Kanamori and M. Kanamori, J. Appl. Phys. 50, 8095 (1979).

43. V. Cazcarra and P. Zunino, J. Appl. Phys. 51, 4206 (1980).

44. A. Murgai and H. C. Gatos, J. Electrochem. Soc. 126, 2240 (1979); A. Murgai, J. Y. Chi and H. C. Gatos, J. Electrochem. Soc. 127, 1182 (1980).

45. F. G. Vieweg-Gutberlet, NBS special publication 400-10, 185 (1974).

46. P. Gaworzewski and H. Riemann, Krist. Tech. 12, 189 (1977) (in German).

47. A. Raymond, J. L. Robert and B. Pistoulet, Proc. VI Int. Symp. on GaAs and Related Compounds, Edinburgh, Sept. 1976, edited by C. Helsum (The Institute of Phys., London, 1976), p. 105.

48. D. L. Rode and S. Knight, Phys. Rev. B 3, 2534 (1971).

49. H. Ehrenreich, J. Appl. Phys. 32, 2155 (1961).

50. E. Haga and H. Kimura, J. Phys. Soc. Jap. 19, 658 (1964).

51. K. Osamura and Y. Marakami, Jap. J. Appl. Phys. 11, 365 (1972).

52. J. K. Kung and W. G. Spitzer, J. Electrochem. Soc. 121, 1482 (1974).

53. W. Walukiewicz, J. Lagowski, L. Jastrzebski, M. Lichtensteiger and H. C. Gatos, J. Appl. Phys. 50, 899 (1979).

54. H. Ehrenreich, J. Phys. Chem. Solids 8, 130 (1959).

55. R. B. Dingle, Philos. Mag. 46, 831 (1955).

56. D. L. Rode, Phys. Rev. B 2, 1012 (1970).

57. R. Newman, Phys. Rev. 111, 1518 (1958).

58. W. P. Dumke, M. R. Lorenz and G. H. Pettit, Phys. Rev. B 1, 4668 (1970).

59. L. Jastrzebski, J. Lagowski, H. C. Gatos and W. Walukiewicz, Inst. Phys. Conf. Ser. 45, 437 (1979).

60. L. Jastrzebski, J. Lagowski and H. C. Gatos, J. Electrochem. Soc. 126, 260 (1979).

61. S. M. Sze and J. C. Irvin, Solid State El. 11, 599 (1968).

62. F. Lukes, Czech. J. Phys. 10, 317 (1960) (in German).

63. A. Ohsawa, K. Honda, S. Ohkawa and R. Ueda, Appl. Phys. Lett. 36, 147 (1980); A. Ohsawa, K. Honda, S. Ohkawa and K. Shinoara, Appl. Phys. Lett. 37, 157 (1980).

64. O. S. Heavens, Optical properties of thin solid films, Dover Pub., New York (1965) p. 208.

65. S. J. Czyzak et al, U.S. Government Report No. AD-143919 (1957).

66. A. J. R. DeKock, Philips Res. Repts. Suppl. 1973, No. 1.

67. F. Shimura, H. Tsuya and T. Kawamura, Appl. Phys. Lett. 37, 483 (1980).

68. F. A. Trumbore, Bell Syst. Tech. J. 39, 205 (1960).

69. H. Föll, W. Gösele and B. O. Kolbesen, J. Cryst. Growth 40, 90 (1977).

70. L. Pauling, The nature of the chemical bond, Cornell University Press, New York (1960).

71. L. S. Smirnov and E. G. Tishkovskii, Sov. Phys. Semicond. 12, 313 (1978).

72. S. M. Sze, Physics of semiconductor devices, Wiley, New York (1969) p. 31.

73. H. J. Hovel, Solar cells, Academic Press, New York (1975).

74. T. B. S. Chadda and M. Wolf, Proc. 10th IEEE photovoltaic specialists conf. (1974) p. 52.

75. J. G. Fossum, IEEE Trans. Electron Devices ED-24, 322 (1977).

76. J. Y. Chi, H. C. Gatos and B. Y. Mao, IEEE Trans. Electron Devices ED-27, 1306 (1980).

77. M. D. Godlewski, C. R. Baraona and H. W. Brandhorst, Jr., Proc. 9th IEEE photovoltaic specialists conf. (1973) p. 40.

78. B. Y. Mao, private communication.

79. C. M. Wolfe and G. E. Stillman, Semiconductors and semimetals, edited by R. K. Willardson and A. C. Beer, Academic Press, New York (1975), vol. 10, chap. 3.

80. V. V. Galavanov and N. V. Siukaev, phys. stat. sol. B 38, 523 (1970).

81. O. Roeder, V. Heim and M. H. Pilkuhn, J. Phys. Chem. Solids 31, 2625 (1970).

82. R. C. Clarke, B. D. Joyce and W. H. E. Wilgoss, Solid State Commun. 8, 1125 (1970).

83. G. G. Kovalevskaya and S. V. Slobodchikov, phys. stat. sol. 30, 441 (1968).

84. J. Kudman and E. F. Steigmeier, Phys. Rev. 133, A 1665 (1964).

85. D. Richman, in Compound semiconductors, edited by R. K. Willardson and H. L. Goering, vol. I, p. 214.

86. M. Glicksman and K. Weiser, J. Electrochem. Soc. 105, 729 (1958).

87. D. L. Rode, phys. stat. sol. B 55, 687 (1973).

88. R. L. Henry and E. M. Swiggard, J. Electron. Mater. 7, 647 (1978).

89. B. O. Seraphin and H. E. Bennett in ref. 79, vol. 3, chap. 12.

90. C. M. Wolfe, G. E. Stillman, D. L. Spears, D. E. Hill and F. V. Williams, J. Appl. Phys. 44, 732 (1973).

91. C. M. Wolfe, G. E. Stillman and J. A. Rossi, J. Electrochem. Soc.: solid state science and technology 119, 250 (1972).

92. R. Beserman and T. Bernstein, J. Appl. Phys. 48, 1548 (1977).

93. J. H. Parker, Jr., D. W. Feldman and M. Ashkin, Phys. Rev. 155, 712 (1967).

94. P. A. Temple and C. E. Hathaway, Phys. Rev. B 7, 3685 (1973).

BIOGRAPHICAL NOTE

The author was born and raised in Torino, Italy. During high school, due also to his father's guidance, he started developing a strong interest in science. In 1969 he began attending courses at the Politecnico in Torino where he also worked on a thesis on liquid crystals. In May 1975 he graduated with a B.S. degree in Electrical Engineering with an emphasis on solid state electronics. During these years he developed a strong interest in solid state physics. He continued his studies at the University of London in England where, in September 1976, he graduated with a M.Sc. degree with a mark of distinction in Solid State Physics; his thesis there was an experimental work on ultrasonic attenuation in metals. In October 1976 he came to the Physics Department at MIT, where he had been admitted through the Fulbright Program. In September 1977 he started working as a research assistant in the Electronic Materials Group where this thesis was completed.

During his career the author contributed to the following publications:

R. Malvano and P. Rava, "Optical Studies of a Second Dynamic Scattering Mode in MBBA", Atti della Accademia delle Scienze di Torino 110, 225 (1976).

D. P. Almond, J. A. Rayne and P. Rava, "An Electronic Study of Electron Mean Free Paths in Molybdenum and Tungsten", Proceedings of the Institute of Acoustics, London (1977).

W. Walukiewicz, J. Lagowski, L. Jastrzebski, P. Rava, M. Lichtensteiger, C. H. Gatos and H. C. Gatos, "Electron Mobility and Free Carrier Absorption in InP; Determination of the Compensation Ratio", J. Appl. Phys. 51, (5), 2659 (1980).

P. Rava, H. C. Gatos and J. Lagowski, "Correlation of Oxygen Concentration and Activated Oxygen Donors in Silicon Crystals on a Microscale", Appl. Phys. Letts. 38, (4), 274 (1981).

P. Rava, H. C. Gatos and J. Lagowski, "Activation of the Oxygen Donor in Silicon on a Microscale", Semiconductor Silicon 1981, Electrochemical Society, Minneapolis, May 1981.